STUDIES ON POLYACRYLONITRILE/CELLULOSE NANOCRYSTALS COMPOSITE PRECURSOR AND CARBON FIBERS

A Dissertation
Presented to
The Academic Faculty

by

Huibin Chang

In Partial Fulfillment
of the Requirements for the Degree
Doctor of Philosophy in the
School of Materials Science and Engineering

Georgia Institute of Technology
December 2017

STUDIES ON POLYACRYLONITRILE/CELLULOSE NANOCRYSTALS COMPOSITE PRECURSOR AND CARBON FIBERS

Approved by:

Dr. Satish Kumar, *Advisor*
School of Materials Science and Engineering
Georgia Institute of Technology

Dr. Yulin Deng
School of Chemical & Biomolecular Engineering
Georgia Institute of Technology

Dr. Kyriaki Kalaitzidou
The G.W. Woodruff School of Mechanical Engineering
Georgia Institute of Technology

Dr. Robert J. Moon
School of Materials Science and Engineering
Georgia Institute of Technology

Dr. Paul S. Russo
School of Materials Science and Engineering
Georgia Institute of Technology

Date Approved: November 3, 2017

ACKNOWLEDGEMENTS

First of all, I would like to express appreciation to my advisor, Dr. Satish Kumar, for his insightful advice and strict attitude during my study. Without his encouragement, suggestions, guidance, and kind help, the completion of my thesis would not have been possible. I also thank my committee members: Dr. Yulin Deng, Dr. Kyriaki Kalaitzidou, Dr. Robert J. Moon, and Dr. Paul S. Russo who have generously provided their valuable time and critical suggestions to my thesis.

Special thanks to Dr. An-Ting Chien for his help in fiber spinning and wide-angle X-ray diffraction. I am thankful to Dr. H. Clive Liu for providing assistance in fiber spinning and training for carbon fiber processing. In addition, I am thankful to Jeffrey Luo, Po-Hsiang Wang, Dr. Amir Bakhtiary Davijani, Dr. Bradley Newcomb, Dr. Prabhakar Gulgunje, and Dr. Kishor Gupta for their help and valuable discussions on my research. I would like to thank past and current colleagues in our research group for their insightful discussions and help in my research and coursework.

Financial support from Renewable Bioproducts Institute at the Georgia Institute of Technology and Air Force office of Scientific Research is gratefully acknowledged.

At last, I am deeply grateful to my parents for their endless love and their encouragement. Thanks to my brother and sister for their support, and understanding. I am greatly appreciative to my wife for her understanding, endless support and abundant love.

TABLE OF CONTENTS

LIST OF TABLES

LIST OF FIGURES

SUMMARY

Carbon fibers exhibit lower density and higher specific strength and modulus as compared to other structural materials such as steel and metal alloys. Thus, carbon fibers are gaining more attention as a light-weight material for high performance applications. For example, about 50 wt% of a Boeing 787 airplane is carbon fiber composites. Currently polyacrylonitrile (PAN), a petroleum derivative, is the predominant precursor for carbon fibers. However, the amount of petroleum reserves is limited on earth. Therefore, cellulose nanocrystals (CNCs), as renewable materials, have been proposed as precursors for carbon fibers due to its biorenewability, sustainability, high aspect ratio, and high mechanical properties. This research adopts PAN as the matrix polymer and CNCs as nanofiller. PAN fibers containing up to 40 wt% CNC were spun by gel-spinning technology. The structure, morphology, and mechanical properties of PAN/CNC precursor fibers and their carbon fibers have been studied in this dissertation.

Chapter 1 gives an overview of literature on PAN fiber, carbon fiber, CNCs and CNC-reinforced polymer composites. Challenges and objectives of this thesis are also outlined in this chapter. Chapter 2 focuses on how to prepare individually dispersed CNC suspensions. The results show that H_2O/dimethyl formamide (DMF) co-solvent disperses individual CNCs more effectively than pure H_2O or pure DMF, especially at high CNC concentrations. Chapter 3 discusses the properties of PAN fibers containing 1, 5 and 10 wt% CNCs. The structure, mechanical and dynamic mechanical properties of the fibers at a draw ratio of 10 were studied. The addition of CNCs improves the tensile modulus and results in higher glass transition temperature of PAN fibers. In Chapter 4, the effect of

post drawing process on the structure and properties of PAN and PAN containing 1, 5, 10, 20, and 40 wt% CNC fibers was investigated. The strain to failure of nanocomposites typically goes down with an increase in filler content. However, remarkably, the fully drawn PAN/CNC fibers containing even the 40 wt% CNCs exhibit the same strain to failure as the fully drawn PAN fibers. This is attributed to the well-dispersed CNCs in PAN fibers. In Chapter 5, the orientation and stress transfer in PAN/CNC fibers containing 20 and 40 wt% CNCs were investigated by Raman spectroscopy. The high orientation of CNCs in PAN fibers was observed by Raman spectroscopy, in which the 1095 cm^{-1} Raman band of CNCs shows a two-fold symmetry under vertical/vertical (VV) mode and a four-fold symmetry under vertical/horizontal (VH) mode. In Chapter 6, the effect of CNC on the stabilization kinetics of PAN fibers was studied. The addition of CNCs improves the orientation of the ladder polymer when PAN/CNC fibers are stabilized either in air or in N_2 followed by air. Furthermore, with the addition of 40 wt% CNC, the activation energy of cyclization and crosslinking reactions of PAN is reduced by 17.5 and 19%, respectively. Chapter 7 discusses the properties of PAN and PAN/CNC based carbon fibers. The carbon fibers made from PAN containing 20 wt% CNCs show the tensile strength of 2.3 GPa and the tensile modulus of 252 GPa, which are comparable to the PAN based carbon fiber properties (tensile strength of 1.9 GPa and tensile modulus of 251 GPa) processed under the same conditions. Conclusions and recommendations for the future work are presented in Chapter 8.

CHAPTER 1. INTRODUCTION

1.1 Overview

Polyacrylonitrile (PAN) fibers are used in our daily life such as blankets, outdoor awnings and sweaters. In addition, PAN is the precursor material for carbon fiber. Due the low density and high strength-to-weight ratio, carbon fibers are used in light-weight and high performance composites for airplanes and cars. Nowadays, sustainable materials are desired due to the environmental concerns and limited amount of non-renewable resources. Cellulose nanocrystals (CNCs), the most abundant biorenewable polymer on earth, are being investigated for different applications. Incorporation of CNCs into PAN fibers not only expands the applications of sustainable materials in polymer fiber industry but also has the potential of positive effect on the carbon fiber green foot print.

1.2 PAN fiber

PAN fiber was developed by DuPont in 1948 [1]. PAN fiber is manufactured from homopolymer PAN or copolymer PAN. For carbon fiber production, the copolymer PAN containing co-monomers such as itaconic acid and methacrylic acid are usually used, as these co-monomers promote the initiation of the stabilization reactions [2].

1.2.1 PAN fiber spinning

PAN fiber has been spun using a variety of techniques including melt spinning, dry spinning, wet spinning, dry-jet wet spinning, and gel spinning. Schematic diagrams of theses spinning systems are shown in Figure 1.1. Traditionally, PAN is dissolved in a solvent and extruded into fibers by solution spinning. PAN is soluble in polar solvents like N,N-dimethyl formamide (DMF), N,N-dimethyl acetamide (DMAc), and dimethyl

sulfoxide (DMSO), and aqueous solutions of ethylene carbonate, as well as some mineral salts [3]. The solution spinning can be classified by the arrangement of the spinneret and the coagulation bath. In wet spinning, spinneret is immersed in the coagulation bath and as-spun fibers pass directly into the coagulation bath [4]. Dry-jet wet spinning is similar to wet spinning. The difference is that there is an air gap between the spinneret and the coagulation bath. Gel spinning was invented to make high-strength polyethylene fiber at DSM in the Netherlands [5]. Since then, gel spinning has also been applied to PAN [6-9]. The gel spinning process may be conveniently divided into two parts: firstly the preparation of a substantially unoriented gel filament, and secondly the processing of this filament to form a highly oriented, strong, and stiff fiber[10]. By the use of the gel spinning technique, PAN solution is spun into a quenching bath to form fibers in a gel-like-state. This gel can be stretched to high extensions and gives rise to strong and stiff fibers. Compared with other spinning methods, gel spinning polymer solution is made with relatively high molecular weight polymers, and at a relatively low solid concentration. A low polymer concentration helps achieve a low degree of polymer entanglement, which allows for higher drawability, resulting in higher molecular alignment and higher modulus than what can be achieved by most other spinning methods (3, 4). In dry spinning, there is no coagulation bath during solution spinning. The solvent in the as-spun fibers is evaporated by passing them through the hot chamber[11]. Melt spinning of PAN is advantageous, as fibers are produced more economically and in an environmentally friendly way. However, PAN tends to degrade rather than melt. Melt-processable high-acrylonitrile copolymers were investigated that can be melt processed[12]. In electrospinning, high voltage (typically 10 to 20 kV) is

applied between the spinneret and the fiber collector, and the polymer solutions are spun into fibers[13]. Using electrospinning, fibers with diameters from about 50 nm to few micrometers can be manufactured

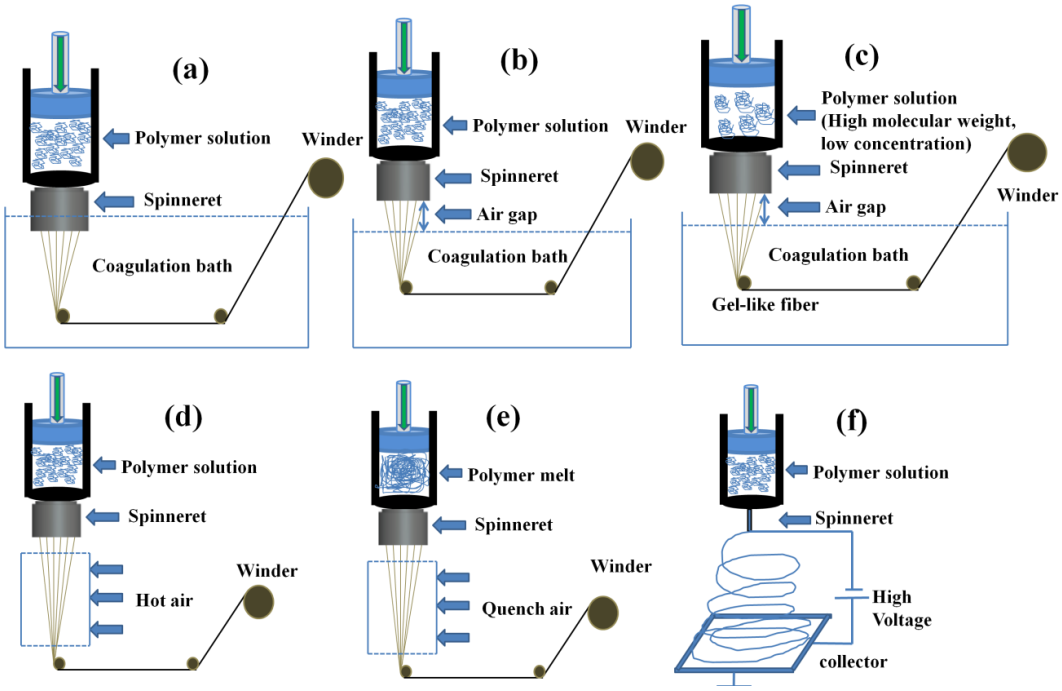

Figure 1.1. Schematic diagrams of various spinning systems. (a) wet spinning, (b) dry-jet wet spinning, (c) gel spinning, (d) dry spinning, (e) melt spinning, and (f) electrospinning [14].

1.2.2 Structure of PAN fiber

The chemical structure of PAN molecules is shown in Figure 1.2 [15]. The PAN molecule has nitrile side groups that have strong dipole interactions. Because of the dipole repulsion between intra-nitrile groups, the molecules tend to form a rod-like helical structure. Wide angle X-ray diffraction (WAXD) pattern of PAN fibers consists of two relatively sharp equatorial diffraction peaks and a third weak peak. These spacings indicate that PAN chains pack in hexagonal or orthorhombic geometry as shown in

Figure 1.3 [16]. The post-drawing process has the effect of the crystal size and crystal structure. PAN chains pack in as-spun PAN fibers has orthorhombic structure. While stretching the PAN fibers would lead to hexagonal structure and increase the PAN crystal size [9].

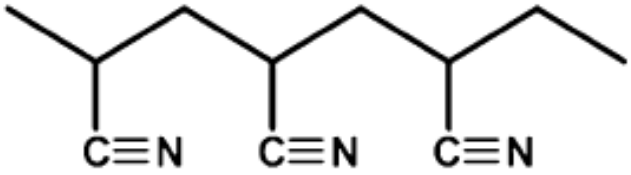

Figure 1.2. Chemical structure of PAN molecule.

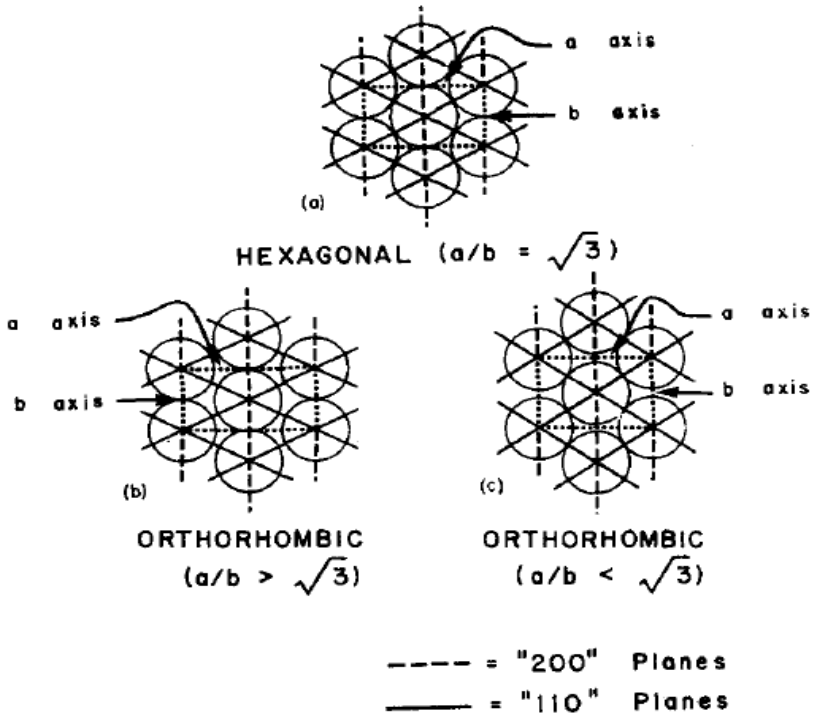

Figure 1.3. Illustrations of hexagonal and orthorhombic packing of PAN molecules[16].

1.3 Cellulose nanocrystals (CNCs)

Cellulose is the most abundant biorenewable polymer in the biosphere, having an annual production that is estimated to be over ~10^{11} tons[17]. It has been used in our daily life for thousands of years. However, only a limited amount of cellulose is consumed because of its uncompetitive mechanical properties or cost. CNC is not known to us until recently when cellulose fibers yield defect-free, rod-like nanocrystalline residues when subjected to acid hydrolysis. CNCs, which have a near perfect crystal structure, possesses high tensile strength and high tensile modulus, as established by experimental and theoretical calculations [18-20]. So CNCs have the potential to be excellent reinforcing materials in polymer based composite.

1.3.1 Structure of cellulose

Cellulose is the major constitutes of plants, bacteria and some marine animals[21]. The hierarchical structure of the tree is shown in Figure 1.4 [22]. In nature, cellulose exists of metastable cellulose I which consist of two suballomorphs I_α and 1_β[23]. Cellulose I is easy to convert to thermostable cellulose II [21, 24, 25]. Cellulose is semicrystalline in nature and it is a polysaccharide of a linear chain of linked β –D glucopyranose units with 1→4 glycosidic bonds (Figure 1.5).

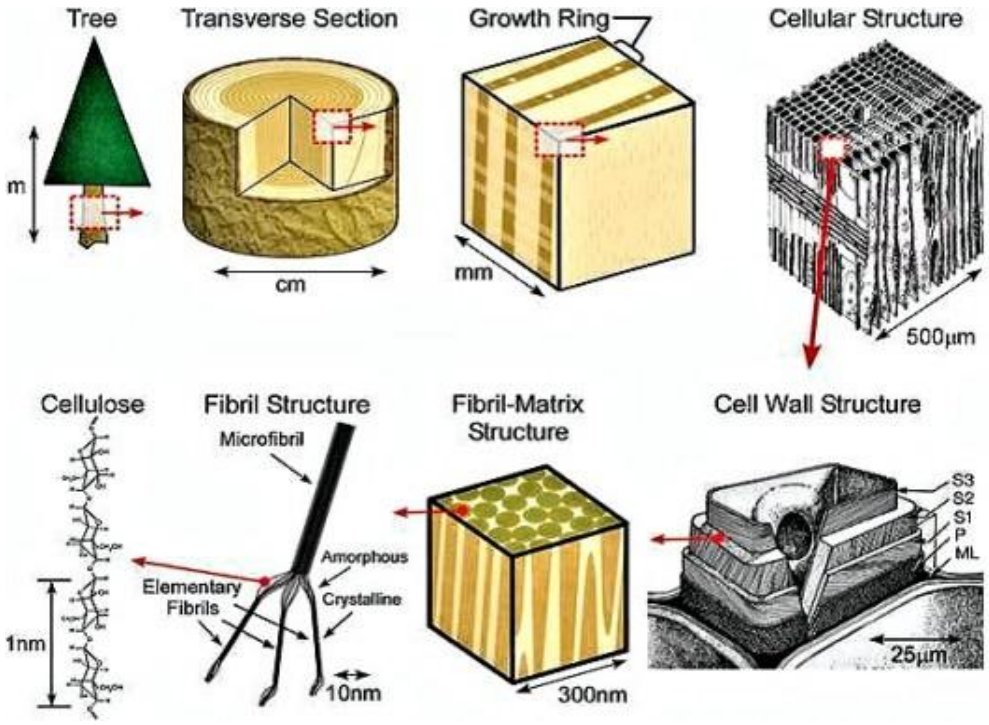

Figure 1.4. Schematic of the tree hierarchical structure [22].

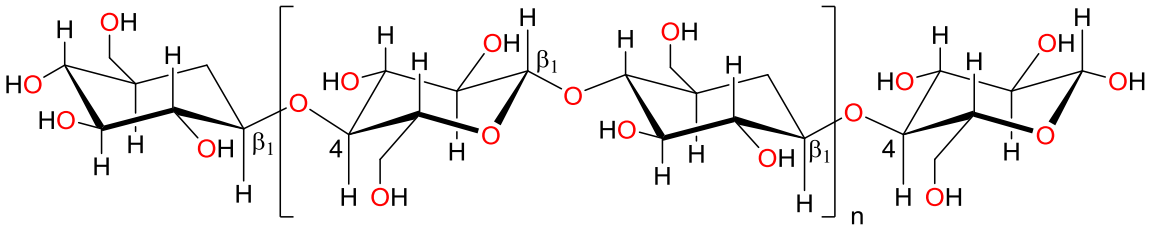

Figure 1.5. Chemical structure of cellulose [26].

1.3.2 Preparation of CNCs

Typical cellulose-based nanomaterials include cellulose nanocrystals (CNC) and cellulose nanofibrils (CNF) based on their preparation and its dimension. CNC or CNF can be prepared by methods including cryocrushing[27, 28], grinding[29, 30], high pressure homogenizing[31], acid hydrolysis[32-34], enzyme-assisted hydrolysis[35, 36]. CNF usually prepared by TEMPO (2,2,6,6-tetramethypiperidine-1-oxyl)-mediated

oxidation on the surface of microfibrils and a subsequent mild mechanical treatment[37], or ultrasonic methods [38].

Acid hydrolysis is the most common way to isolate CNCs from the cellulose fibers [39]. When native cellulose is treated with strong acids, such as sulfuric acid[40, 41], hydrochloric acid[42], and phosphoric acid[43], the amorphous regions of cellulose microfibrils are preferentially attacked and the resulting material is a colloidal suspension of cellulose crystallites. During the process of acid hydrolysis, amorphous regions of cellulose are preferentially hydrolyzed, whereas crystalline regions that have a higher resistance to acid attack remain intact [44]. Table 1.1 summarizes the characteristics and properties of CNCs and CNFs.

Table 1.1 Comparison of cellulose nanocrystals (CNCs) and cellulose nanofibrils (CNFs)[14].

	CNC	CNF
Preparation method	Strong acid hydrolysis	Mechanical treatment
Morphology	Needle-like crystals	Long flexible fibers
Composition	Highly crystalline cellulose	Amorphous and crystalline cellulose
Length (nm)	50 – 500	> 1000
Width (nm)	3 - 10	5 - 30
Aspect ratio (Length/Width, L/W)	5 < L/W < 50	L/W > 50
Tensile strength (GPa)	7.5	< 3
Tensile modulus (GPa)	110 - 220	< 100

1.3.3 Dispersion of CNCs

Despite the high mechanical properties of individual CNCs [18-20], it is a challenge to obtain significant property enhancement in nanocomposites. This is especially true in a hydrophobic polymer matrix system, due to the poor dispersibility of CNCs in organic solvents [45]. Different stabilizing methods such as surfactants [46, 47], silylating agents [48], grafting of polyethylene glycol (PEG) [49], grafting of maleated polypropylene [50], and acylation [51] have been explored to improve CNC dispersibility in organic solvents. However, for some polymers, the surface modification may have negative impact on mechanical properties of the composites [52].

1.3.4 Polymer/CNC composites

Due to its rod-like morphology and high mechanical properties, CNC can be used as a rheology modifier or for reinforcement of polymer materials [26]. CNC reinforced composites such as poly (oxyethylene) [53], epoxy resin [54], polyvinyl acetate (PVAc) [55], and PAN [56] have been processed. Some composites show improved mechanical properties as compared to pure polymer. For example, the fracture toughness of PVAc increased from 2 to 6 MJ/cm^3 at a low CNCs concentration of 2 wt% [55]. In one study, with incorporation of 8 wt% CNCs into epoxy film, tensile strength increased from 7 to 15 MPa and tensile modulus increased from 296 to 800 MPa [54]. Tensile strength and tensile modulus of PAN film increased from 75 to 132 MPa and from 2.2 to 3.7 GPa, respectively, as CNC concentration increased from 0 to 40 wt% [56].

Because the elastic modulus of CNCs in axial direction is much higher than in the transverse direction, high orientation of CNCs in polymer nanocomposites is

desirable[26]. For polymer/CNC composite fibers, CNCs have been used for reinforcing poly(acrylic acid) (PAA) [57], poly(lactic acid) [58, 59], poly(ε-caprolactone) [60], polyethylene oxide [61], poly (vinyl alcohol) [62], and poly (methyl methacrylate) [63] using electrospinning method. CNCs are also used for reinforcing alginate [64], cellulose acetate [65] and silk fibers [66] using wet-spinning method. The addition of CNC in polymer fiber has been observed to improve the mechanical properties for many systems. It is reported that the tensile strength and tensile modulus of PAA nanofibers mat increased from 0.29 to 4.51 MPa, and from 0.06 to 1.98 GPa, respectively, with the addition of 20 wt% CNCs [57]. Similarly, with the addition of 5% CNCs, tensile strength of silk fiber increased from 0.48 to 0.73 GPa [66].

1.3.5 Orientation and stress transfer of CNC composites

Raman spectroscopy has been used to investigate the deformation behavior of the cellulosic materials [67-69]. Cellulosic materials exhibit well-defined 1095 cm^{-1} Raman band, which is attributed to C-O ring stretch. Under polarized Raman spectroscopy, the 1095 cm^{-1} band can be used to quantify the orientation of cellulose in fibers [70], and the band shift can be observed upon deformation. This band shift can be used to determine the stress transfer properties [69, 71]. It was observed that strain dependent Raman band shift of 1095 cm^{-1} peak is different for various regenerated cellulose fibers and natural cellulose [67].

1.4 Carbon fiber

Carbon fibers are widely used as reinforcement in high-strength, low-density composite materials such as carbon fiber reinforced plastics and carbon fiber reinforced

cement[72]. Compared with other reinforcing fibers such as glass and organic polymer fibers, carbon fibers offer superior strength and modulus. Since late 1950s, high strength carbon fibers made from polyacrylonitrile (PAN) have been studied due to the significant demand for higher performance composite materials. Meanwhile, the quality of carbon fibers has been greatly improved. For example, the tensile strength of carbon fibers is improved from ~ 1 GPa to ~ 7 GPa [73].

1.4.1 PAN-based carbon fiber

PAN fibers are converted to carbon fibers via oxidative stabilization followed by carbonization. Both steps are carried out under tension. Oxidative stabilization occurs in air, typically in the temperature range of 180–320°C. Stabilization chemistry is complicated and consists of cyclization of the nitrile groups and oxidation [74]. The possible structures that may arise in stabilized PAN are shown in Figure 1.6 [75]. Carbonization is carried out in an inert atmosphere such as nitrogen or argon (up to 1,700°C). In carbonization process, the non-carbon elements are eliminated in the form of volatile gases such as HCN, NH_3, H_2O, CO_2, N_2, and hydrocarbons [76]. High-strength carbon fibers are typically carbonized at a maximum temperature of approximately 1,400°C. Graphitization, if needed, is carried out in an inert atmosphere as well at temperatures as high as 2,800°C to further increase fiber stiffness. The suggested reaction schemes of PAN during stabilization and carbonization are shown in Figures 1.7 and 1.8, respectively.

Since the beginning of the modern carbon fiber research in late 1950s, their mechanical properties have been greatly improved. The most common precursor for

carbon fiber is PAN, since PAN based carbon fibers provide a good balance of tensile and compressive properties. Even though the pitch based carbon fibers are also available and meso phase pitch based continuous carbon fibers can be manufactured commercially with greater than 90 % of the theoretical modulus [72, 77], these pitch based carbon fibers have relatively low tensile strength (~3 GPa) and very low axial compressive strength (200 to 400 MPa) [14, 78, 79]. For comparison, PAN based carbon fibers have low to intermediate tensile modulus, but these fibers are amongst the strongest structural materials available today. The commercially available PAN based carbon fibers are manufactured using wet or dry-jet wet spinning technology. Using the gel spinning technology, PAN based carbon fibers with up to 30% higher modulus than the state of the art carbon fiber (IM7) have been manufactured at Georgia Tech without compromising the tensile strength [73]. The tensile strength and tensile modulus of PAN based carbon fibers are plotted in Figure 1.9.

1.5 Composite precursors for carbon fiber

In order to improve the performance of PAN based carbon fiber, nano-fillers such as carbon nanotubes reinforced PAN based carbon fibers have been investigated [7, 8, 80]. Renewable materials such as lignin have also been blended with PAN to make carbon fibers.

*1.5.1 **PAN/carbon nanotube composite precursor for carbon fiber***

When only 1 wt % carbon nanotubes (CNTs) were added into PAN matrix, the tensile modulus and tensile strength of the resulted carbon fiber increases from 302 to 450 GPa, and from 1.98 to 3.24 GPa, respectively [80]. It has been shown that the

addition of CNTs improves the orientation of the ladder polymer and increases the maximum tension that can be applied during stabilization [7]. By optimizing stabilization conditions, PAN containing 1 wt % CNT based carbon fibers show a tensile strength of 4 GPa and a tensile modulus of 286 GPa using batch carbonization processing at 1100°C [81]. Furthermore, based on TEM images, carbonized PAN is shown to be templated around CNT in PAN/CNT based carbon fibers (Figure 1.10) [82]. However, in the PAN/CNT based carbon fiber, CNTs are easy to agglomerate as bundles and each end of a CNT bundle can be a micro-void in the carbon fibers [14].

	Structure
Heteroaromatic cyclic structure	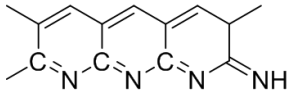
Polyimine cyclic structure (ladder polymer)	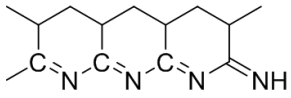
Poluenamine cyclic structure	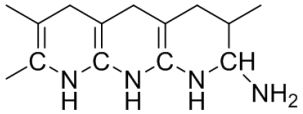
Propagation crosslink	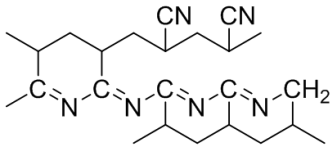
Inermolecular nitrile crosslink	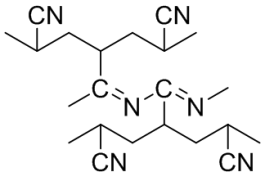
Azomethine crosslink	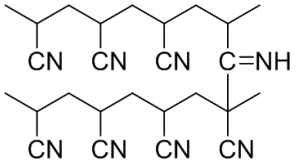
Conjugated polyene	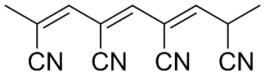

Figure 1.6. Possible structures which may arise in stabilised PAN [75].

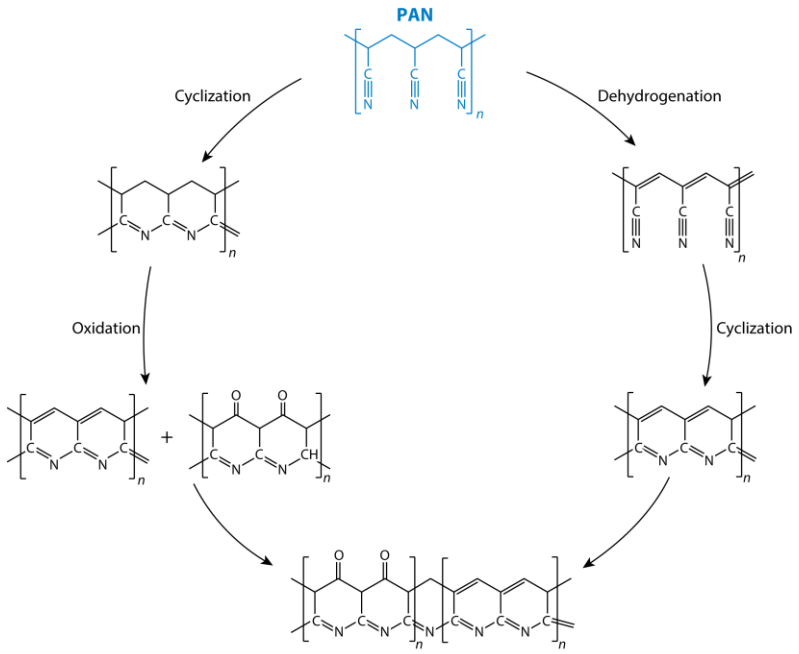

Figure 1.7. Proposed chemical reaction schemes of PAN during stabilization [14].

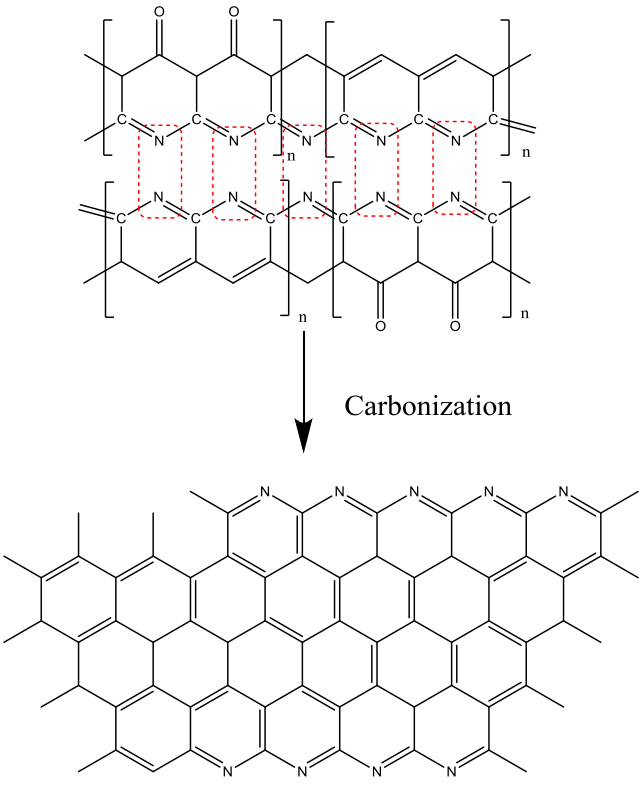

Figure 1.8. Proposed chemical reaction scheme of PAN during carbonization [14].

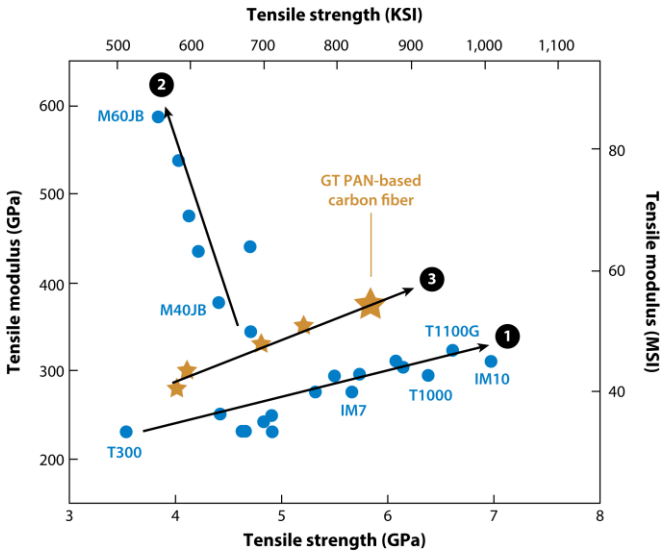

Figure 1.9. Tensile strength versus tensile modulus of various PAN based carbon fibers. Trend lines 1 and 2 represent the trajectory of the developments in the high strength and high modulus solution spun PAN based carbon fibers, respectively. Line 3 represents the development of high-strength and high-modulus gel-spun PAN-based carbon fibers-at Georgia Tech [14, 73].

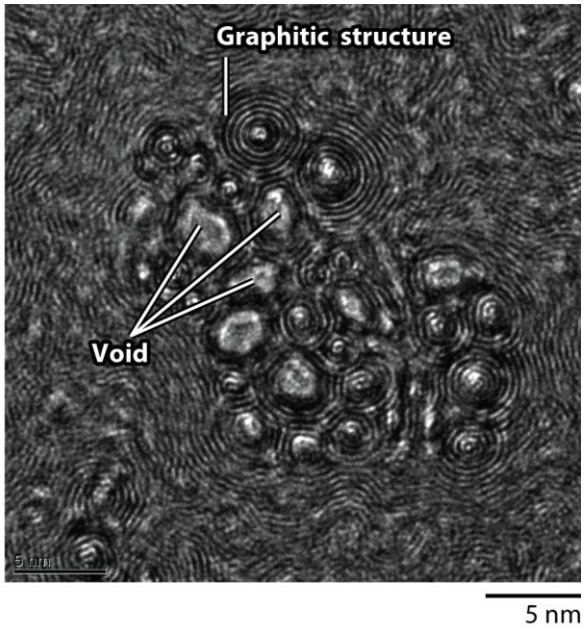

Figure 1.10. PAN/carbon nanotube (CNT)-based carbon fiber. The PAN/CNT-based carbon fiber shows carbonized PAN templating on the CNT's surface [14, 82].

1.5.2 Renewable materials for carbon fiber

Rayon (or regenerated cellulose) was first used to make carbon fibers in late 1950s. The mechanism of cellulose pyrolysis is complicated and has been investigated. One possible mechanism that consists of four steps is shown in Figure 1.11 [83]. In the first step (≦150 °C), the physically adsorbed water is desorbed. Then the anhydroglucose units are dehydrated up to 240 °C. Afterwards, cellulose is decomposed by cleavage of glycosidic and other C-O bonds as well as of C-C bonds up to 400 °C. In the final step (> 400 °C), the aromatization of the remaining residue with four carbon atoms occurs [84]. Due to low carbon yield and low mechanical properties of Rayon based carbon fiber, PAN has been the predominant precursor to make carbon fiber. Nowadays, due to the high cost and environmental concerns of PAN-based carbon fibers, cellulose and lignin have been proposed as potential cost effective alternatives for carbon fiber precursor as a renewable feedstock. However, cellulose-based and lignin-based carbon fiber showed considerably lower tensile strength and modulus than PAN-based carbon fibers [85-90]. In order to take full advantage of PAN fiber's mechanical properties and to use renewable resources, composite fibers such as PAN/cellulose and PAN/lignin based carbon fibers are manufactured [91-94]. In manufacturing these composite fibers, one of the challenges is how to make micro-voids free carbon fibers [95].

1.6 Challenges for making PAN/CNC composite precursor and carbon fibers

CNCs are hydrophilic due to the presence of hydroxyl groups at their surfaces. While PAN is a hydrophobic polymer, it can be only dissolved in organic solvents such as DMF, DMSO, and DMAc. Due to the nano-sized dimension and high surface area,

CNCs are highly agglomerated. The first challenge is how to effectively prepare well-dispersed CNCs in organic solvents. As discussed above, elastic modulus of CNCs in axial direction is much higher than in the transverse direction. To make CNC reinforcement more efficient in fibers, how to make the orientation of CNCs along the fiber axis is another challenge. As a renewable material, more CNCs concentration is expected to incorporate into PAN fibers. However, the strain to failure of polymer nanocomposites decreases with increasing CNC concentration. In other words, these high-CNC loaded polymer fibers become brittle, which limits the applications of these fibers. So to make PAN/CNC fibers with high CNC concentration as well as good ductility is another challenge. Furthermore, the load transfer between polymer matrix and CNC need investigation since effective load transfer in these composite fibers also determine the fiber's properties. As mentioned above, the stabilization reactions are different between PAN and CNC, understanding the effect of CNC on the stabilization kinetics of PAN is critical to get good properties of PAN/CNC based carbon fibers.

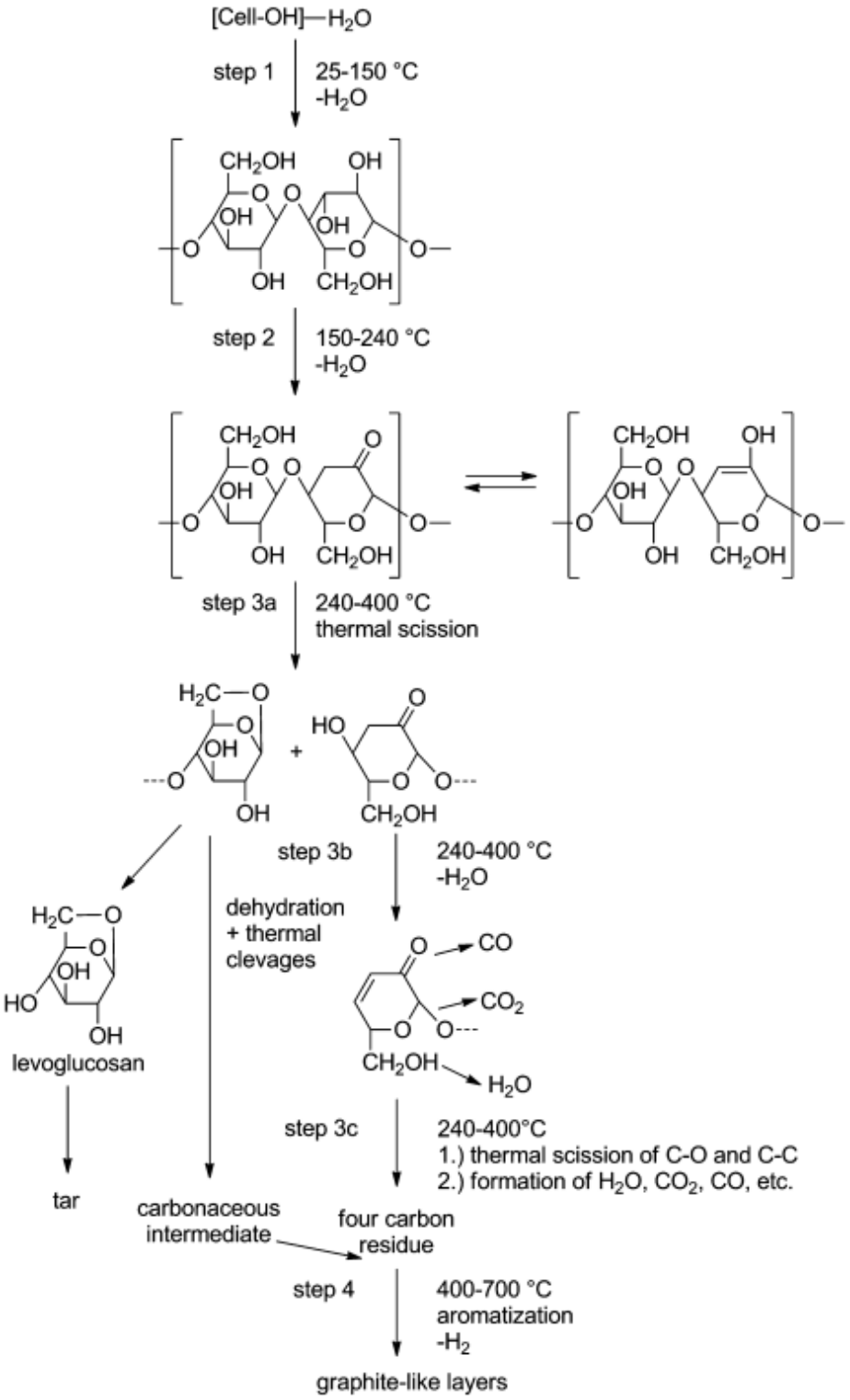

Figure 1.11. Proposed pyrolysis mechanism for the conversion of cellulose to carbon [83, 84].

1.7 Thesis objectives

The broad objectives of this thesis are to investigate the effect of cellulose nanocrystals (CNCs) on the structure, mechanical, and thermal properties of polyacrylonitrile (PAN) precursor fibers, and of the resulting carbon fibers. The following studies will be carried out to achieve these objectives.

- Study the dispersion behavior of CNCs in organic solvents such as N,N-dimethyl formamide (DMF).
- Study the effect of CNCs and post-drawing on the structural, mechanical, and thermal properties of gel-spun PAN fiber.
- Study the orientation and stress transfer in PAN/CNC composite fibers.
- Study the stabilization and carbonization behavior of PAN/CNC composite fibers**.**

CHAPTER 2. INDIVIDUALLY DISPERSED WOOD-BASED CELLULOSE NANOCRYSTALS

2.1 Introduction

In polymer composites , good dispersion of fillers in the polymer matrix is one of the key factors for obtaining good mechanical properties [96]. Although it is reported that a small amount of water is critical to disperse CNCs in organic solvents such as DMF and DMSO [45, 97], there is no systematic study to investigate the effect of water on the dispersibility of CNCs in organic solvents. In this chapter, the effect of water on the dispersibility of CNCs in DMF is systematically investigated.

2.2 Experimental

2.2.1 Materials

Cellulose nanocrystals (CNCs) with approximately 5 nm in diameter and 150-200 nm length was obtained from Process Development Center, University of Maine (freeze-dried powder, lot# 2012-FPL-CNC-48/051, 1.05 wt % sulfur)[22, 98]. SEM images of the CNCs used in this study are shown in Figure 2.1.The as-received CNCs are highly agglomerated micro-size sheets and individual CNC are visible at the edge of the sheet. Dimethyl formamide (DMF) obtained from BDH, Inc. was purified by distillation before use.

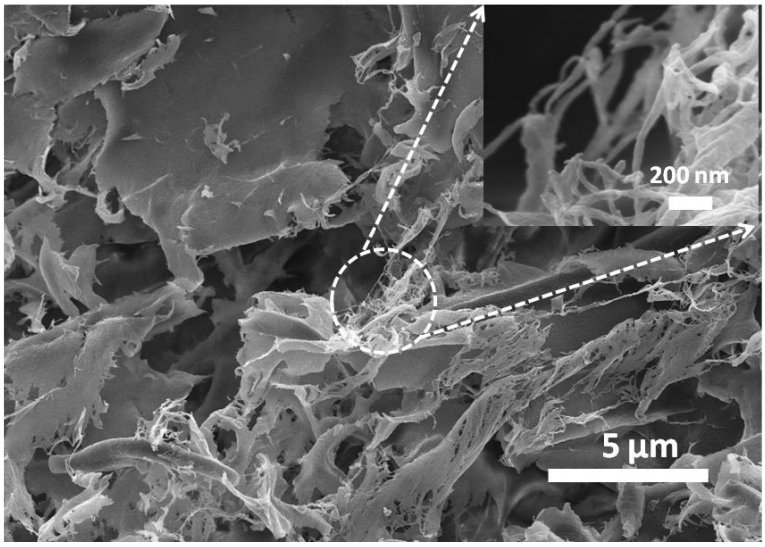

Figure 2.1. SEM image of the as-received CNCs.

2.2.2 Preparation of CNC/DMF dispersion

The moisture content of as-received CNCs is 3.8 wt % as determined by TGA (TA Instrument, Q500). The as-received CNCs was put in a glass bottle with loose lid and dried in oven at 105 °C for 6 – 48 hours to obtain lower moisture-containing CNCs. The moisture content of dried CNCs was then determined by TGA (Figure 2.2). Various CNCs were dispersed in DMF, DMF/water mixture, or in water in a sonication bath (Branson 3510R-MT, 100 W, 42 kHz).

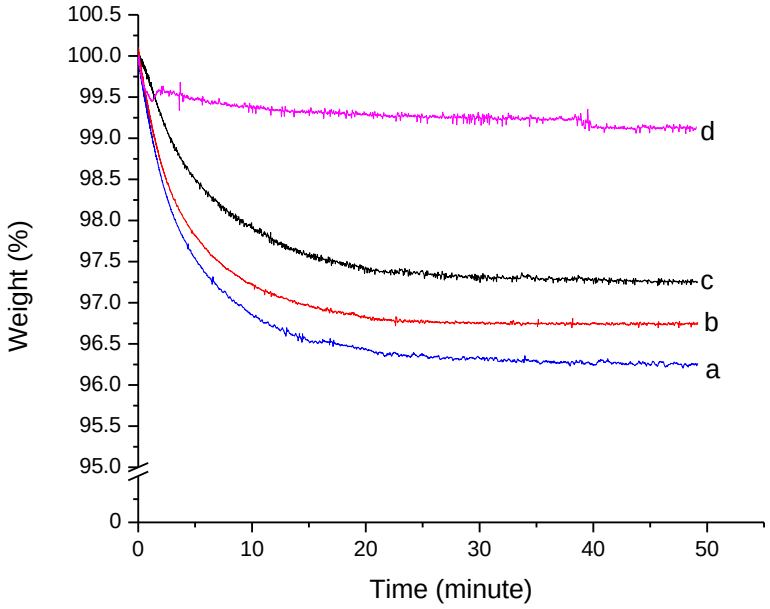

Figure 2.2. TGA of various CNCs. (a) as received CNCs. (b), (c) and (d) as received CNCs vacuum dried at 105 °C in vacuum oven for 6, 12 and 48 hours.

2.2.3 Characterization

CNCs were observed using scanning electron microscope (SEM, Zeiss Ultral60). For TEM, drops of dilute CNC solution were deposited on carbon-coated electron microscope grids and negatively stained with uranyl acetate (CF200-Cu, 200 Mesh, Electron Microscopy Sciences, Hatfield, PA). TEM images were obtained using a probe corrected scanning/transmission electron microscope JEOL JEM-ARM200cF (JEOL, Ltd, Tokyo, Japan) operated at 80kV. The dimension of CNCs was measured by ImageJ software. Dynamic light scattering (DLS) study was conducted using BI-200SM light scattering system (Brookhaven Instruments Co.), with the detector at 90 degrees, power at 11 mW, and a vertically polarized 532 nm laser. The solutions were kept at 25 °C during DLS measurement, and the data collection duration was 2 min. Each solution was

measured at least 5 times. The viscosity and refractive index of mixture of H_2O/DMF are based on literature data[99, 100] using linear interpolation method and they are summarized in Table 2.1. Zeta potential of CNC/DMF (CNC containing 3.8 wt% moisture) solutions with different sonication time was measured by Zetasizer Nano ZS90 (Malvern Instruments) as shown in Table 2.2. The solution spectra were recorded by a Nicolet Magna-560 Fourier transform infrared spectroscopy (FTIR) in attenuated total reflectance (ATR) mode. FTIR spectra were recorded in a spectral range of 4000-400 cm^{-1} with a resolution of 0.5 cm^{-1}.

Table 2.1. Viscosity and refractive index parameters used for DLS experiments.

Volume percent water in DMF	Viscosity (mPa·s)	Refractive index
0	0.815	1.428
5	1.046	1.426
25	2.246	1.413
50	2.352	1.389
75	1.563	1.358
100	0.922	1.331

Table 2.2. Zeta potential of CNC/DMF solutions after different sonication times. (CNCs concentration: 75 mg/100 mL, CNC moisture content 3.8 wt%).

Sonication time (hour)	Zeta potential (mV)
1	-14.5 ±1.6
2	-16.1 ±1.4
4	-15.2 ±1.6
8	-16.0 ± 1.7

2.2.4 Simulation

Simulations are carried out in ChemBio3D 14 for energy minimization. 4 CNCs repeat units are initialized randomly in the DMF, H_2O or H_2O/DMF mixture. Using the molecular dynamics package, the molecules were heated to 300 K and kept at that temperature for 300 picoseconds.

2.3 Results and discussion

CNCs dispersions are systematically characterized by dynamic light scattering (DLS). Hydrodynamic radius (R_h) of individual CNC is calculated as follows, which can be used to assess the dispersibility of CNCs in solvents. The hydrodynamic radius, R_h, is defined as the size of a diffusion-equivalent sphere according to the Stokes-Einstein relation:

$$R_h = \frac{KT}{6\pi\eta D_t} \qquad (2.1)$$

Where K is Boltzmann's constant, T is the absolute temperature, η is the viscosity, and D_t is the translational diffusion coefficient.

For rod-shaped macromolecules with a given length (L) and diameter (d) in dilute solution, the translational diffusion coefficient (D_t) can be approximated by the Kirkwood and Riseman results:[101]

$$D_t = \frac{KT}{3\pi\eta L} \times Ln\left(\frac{L}{d}\right) \qquad (2.2)$$

Combining equations (2.1) and (2.2), results in

$$R_h = \frac{L}{2Ln(\frac{L}{d})} \qquad (2.3)$$

Wood-based CNCs used in this study are reported to have a diameter of 5 nm and length is in the range of 150-200 nm. Using equation (2.3), the hydrodynamic radius of the individual CNC is calculated to be between 22 and 27 nm. If the CNCs are dispersed as individual CNCs in a solvent, then the experimental measurements should result in hydrodynamic radius values in this range.

In one set of experiments (at a concentration of 75 mg/ 100 mL), CNCs with 2.6, 3.2, and 3.8 weight percent moisture were dispersed in pure DMF by bath sonication for different times (moisture is determined by TGA as shown in Figure 2.2). The results show that hydrodynamic radius (R_h) of CNCs decreased with increasing sonication time (Figure 2.3). For low moisture-containing ($\leqq$ 3.2 wt %) CNCs, even after 7 days of sonication, R_h is still higher (38 and 31 nm for 2.6 and 3.2 wt% moisture containing CNCs, respectively) than the calculated value (22 to 27 nm). At moisture content of 3.8 wt %, hydrodynamic radius of 23 nm was achieved after 24 hours sonication. This is consistent with the previous study, where it was reported that a moisture content of 4 wt % in CNCs was necessary to fully disperse them in water[102].

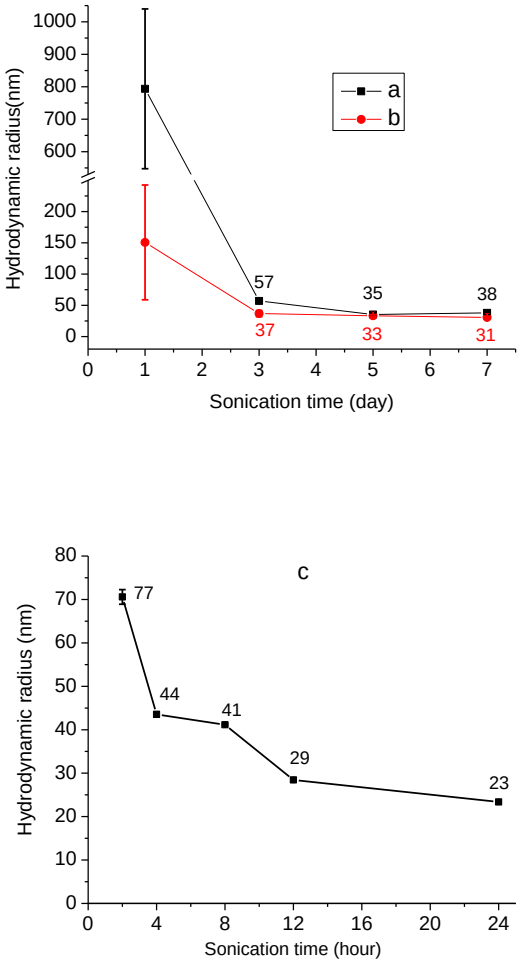

Figure 2.3. Hydrodynamic radius of CNC with different moisture contents dispersed in DMF for different sonication time. (a) 2.6 wt % moisture, (b) 3.2 wt % moisture, and (c) 3.8 wt % moisture. (CNC concentration is 75 mg/ 100 mL).

The binary mixture of solvents is gaining more interest because of combined properties from each solvent. Since above data shows that moisture significantly affects the dispersibility of CNCs in DMF, CNC dispersibility was explored in broad range of H_2O/DMF mixtures. Also, to further confirm the importance of moisture for CNC dispersion, CNC moisture was removed by heating in oven at 105 °C for 48 hours under vacuum. Dried CNCs (0.6 wt % water) were dispersed at concentration of 75 mg/100 mL

in pure DMF, and in 50-50 volume percent H_2O/DMF mixture, and these dispersions were still cloudy even after bath sonication for 1 week, as CNCs were not dispersible. For 3.8 wt% moisture-containing CNCs, hydrodynamic radius of about 22 nm was obtained in a broad solvent concentration range of 5 to 75% water in DMF (Figure 2.4). After 6 hours sonication, hydrodynamic radius (R_h) of CNCs (3.8 wt% moisture-containing) in pure DMF and pure H_2O are 50 nm and 60 nm, respectively, which are significantly higher than the calculated R_h of individual CNCs. However, for 5 and 25 volume percent H_2O in DMF, predominantly individually dispersed CNCs were achieved within 6 hours of sonication, where R_h is below 27 nm. CNCs were predominantly individually dispersed in all co-solvents (when water concentration was in the range of 5 to 75 vol%) within 12 hours of sonication. For pure DMF or pure water, even after 18 hours of sonication, it does not reach to individual CNC status (Figure 2.4).

We also investigated the dispersibility at relatively high CNC concentration of 3 g/100 mL (CNCs contained 3.8 wt % water) (Figure 2.5). For 25-75 volume percent H_2O/DMF mixture, mostly individually dispersed CNCs could be achieved in 24 hours of bath sonication. However, at this CNC concentration, in pure water, sonication had little effect on the R_h of CNC, when sonication time increased from 24 to 66 hours. R_h of CNC in pure water is about 3 times larger than that for 25 and 50 volume percent H_2O co-solvents after 66 hours sonication. In a subsequent experiment, different CNC concentrations were dispersed in 25-75 and 50-50 volume H_2O/DMF co-solvent as well as in pure water (Figure. 2.5b). After 24 hours of bath sonication, individually dispersed CNCs were achieved in H_2O/DMF co-solvents at all CNC concentrations (75 mg to 3 g/100 mL). On the other hand, in pure water, R_h of CNC is slightly larger than that in co-

solvents at low CNC concentration, and it was significantly higher at high CNC concentrations. This suggests that CNCs were not individually dispersed in water, and that they can be individually dispersed very effectively in H_2O/DMF co-solvent at high concentration and for relatively low sonication duration. TEM images obtained from extremely dilute dispersions are included in Figure 2.6, and the average CNC dimensions based on the TEM images are given in Table 2.3.

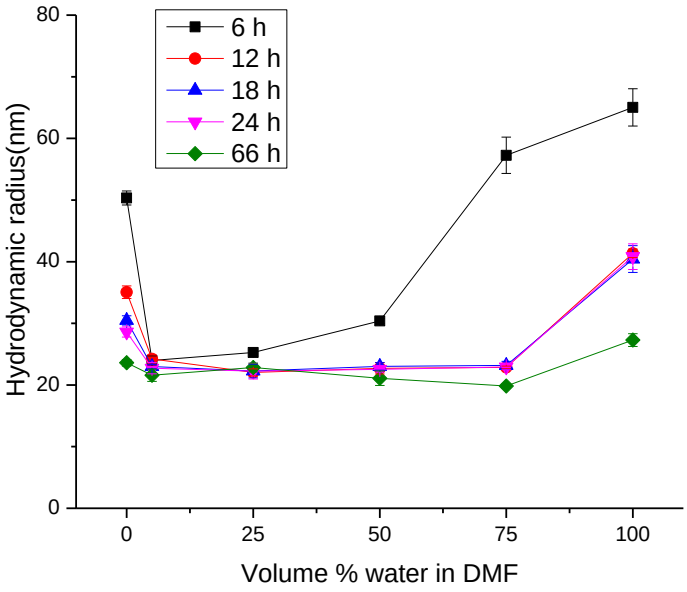

Figure 2.4. Hydrodynamic radius of 3.8 wt% moisture-containing CNCs in H_2O/DMF mixture for different sonication time. (CNC concentration is 75 mg/100 mL).

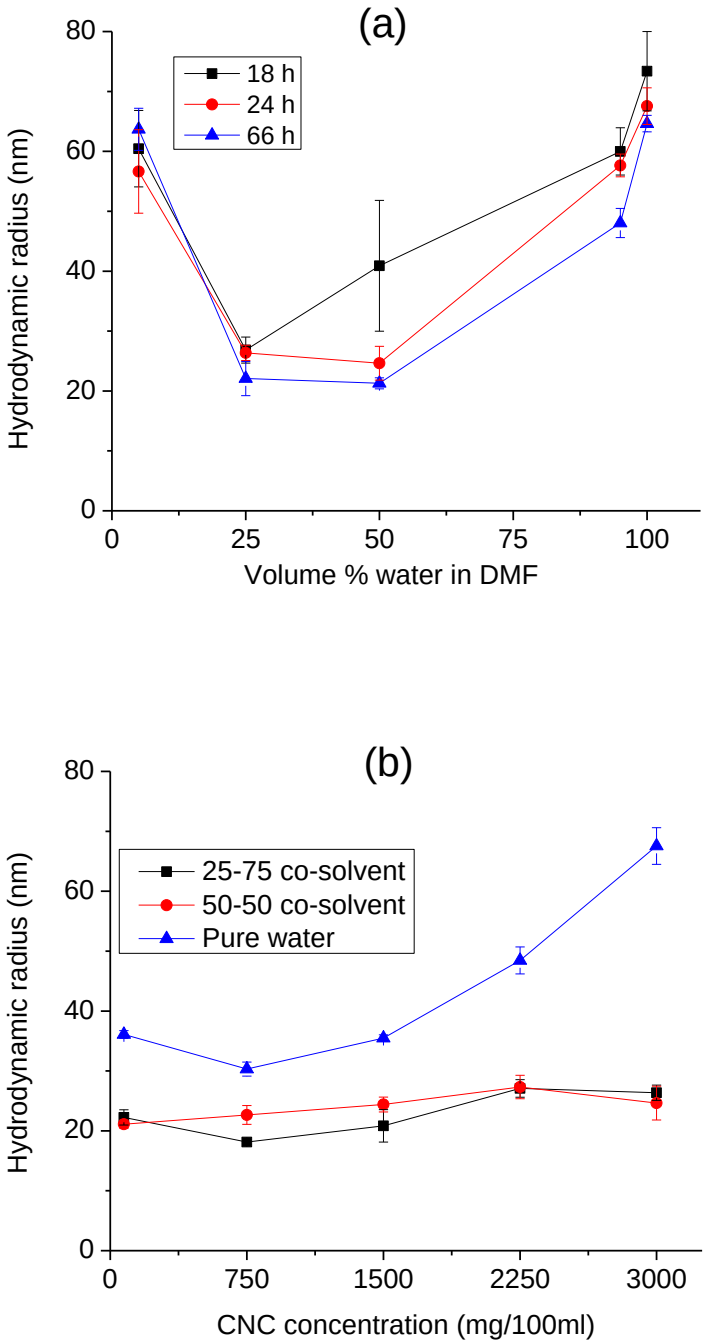

Figure 2.5. Hydrodynamic radius of 3.8 wt % moisture-containing CNCs in solvents. (a) under different sonication time (concentration 3 g/100 mL) and (b) different concentrations after 24 hours sonication.

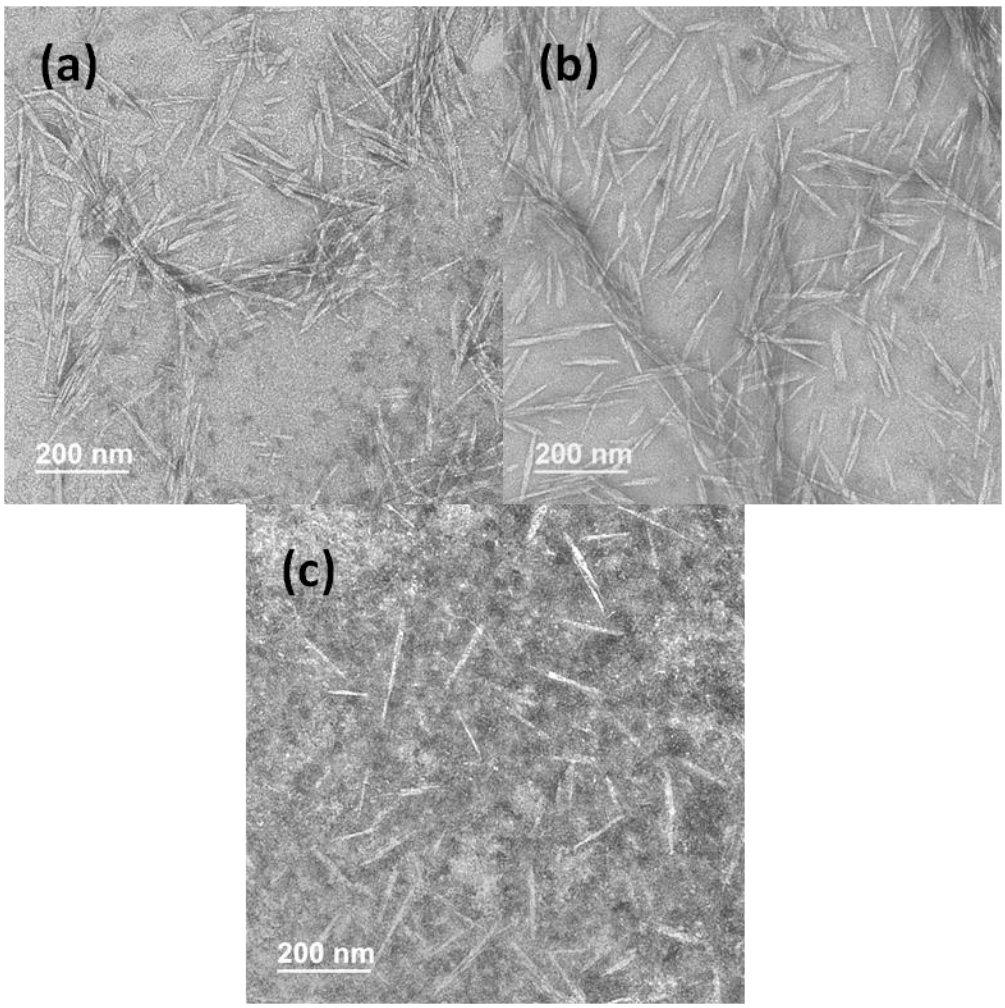

Figure 2.6. Representative TEM images of high CNC concentration (3 g/100 mL, 3.8 wt% moisture) in (a) 5-95 volume percent H_2O/DMF mixture, (b) water, and (c) 25-75 volume percent H_2O/DMF mixture.

Table 2.3. Dimensions of CNC obtained from TEM dispersed in different solvents and the calculated hydrodynamic radius (R_h).

	5-95 H_2O-DMF	25-75 H_2O-DMF	Water
Length (nm)	204 ± 57	153 ± 38	178 ± 27
Diameter (nm)	12.3 ± 2.5	6.3 ± 2.2	10.5 ± 2.2
Calculated R_h	27 - 45	21 - 30	26 - 37

Molecular simulation study was done to understand the CNC dispersion. For this purpose cellulose repeat units were dispersed in 100% DMF, 100% water, and in 25-75 volume H_2O/DMF mixture. In pure DMF, CNC repeat units aggregate in the center, while in pure water CNC repeat units are mostly on the outside (Figures 2.7a and 2.7b). On the other hand, in H_2O/DMF mixture, CNC repeat units were found to be individually dispersed (Figure 2.7c). These are consistent with our experimental results.

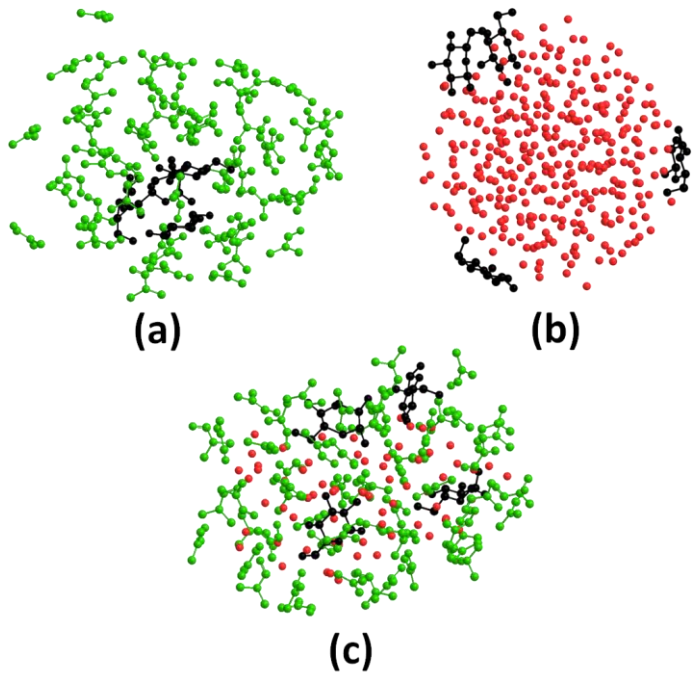

Figure 2.7. CNC repeat unit (black) dispersion in solvents: (a) DMF (green), (b) H_2O (red), and (c) 25-75 H_2O/DMF co-solvent.

Hydrogen bond (H-bond) is formed through hydroxyl groups in CNCs, resulting in CNC aggregates. Water molecules interact with cellulose to form H-bond, and thus results in reduced number of intermolecular hydrogen bonds in cellulose[103]. In moisture-containing CNCs, cellulose-water H-bond forms on the CNC surface, and thus weakens the interaction between two CNCs, thus moisture containing CNCs result in

better dispersion than CNCs without moisture. Water−water hydrogen bonds have lower binding energy than cellulose-water hydrogen bonds[102, 104] Also, due to the strong interaction between water and amide, it is easy to form H-bond between the DMF and water. On the CNC surface, H-bond forms between DMF and H_2O. DMF surrounded individual CNC can effectively prevent the H-bond formation between CNCs. The proposed mechanism is shown in Figure 2.8. Water-DMF molecules have strong interaction. This is well known and is verified by FTIR spectroscopy (Figure 2.9). H_2O/DMF molecules diffuse in between cellulose nanocrystals in H_2O/DMF solvent mixture. Therefore, under same sonication conditions, it is easier to separate CNCs to the individual CNC in H_2O/DMF co-solvent when compared to 100 % H_2O or 100 % DMF.

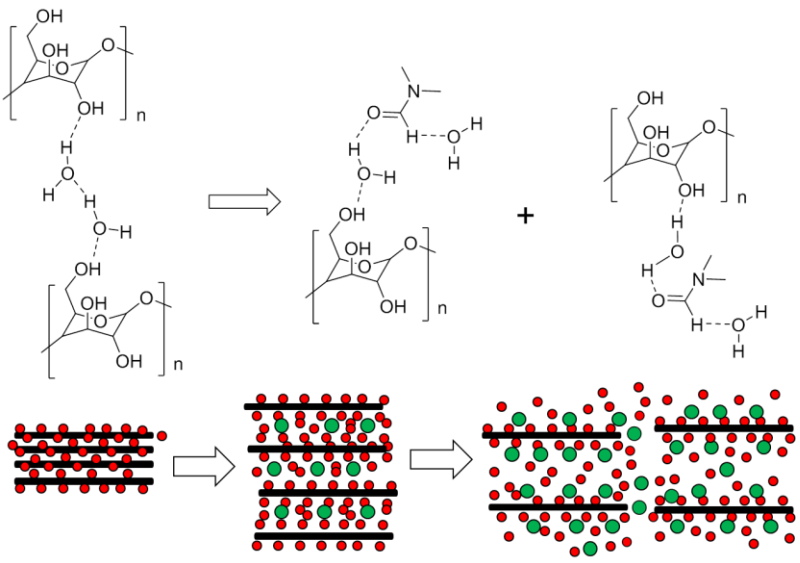

Figure 2.8. Proposed mechanism to disperse CNCs in H_2O/DMF co-solvent.

(CNC, DMF, H_2O)

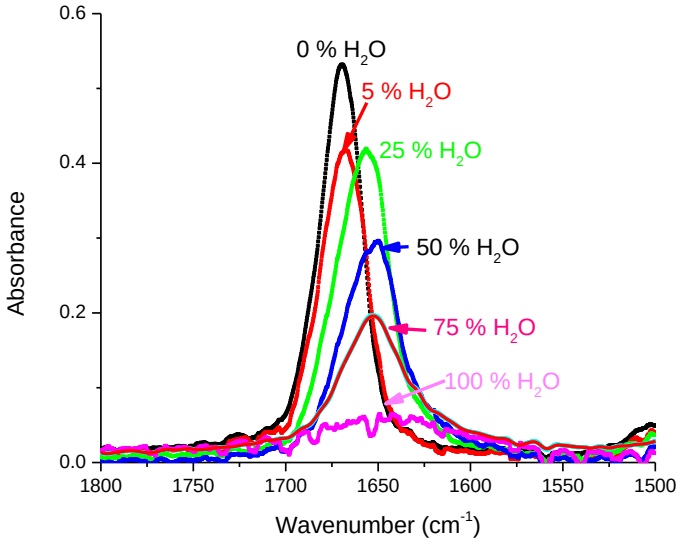

Figure 2.9. ν(CO) stretching region in FTIR spectra of CNC/DMF/H_2O dispersion.

2.4 Conclusions

Individually dispersed CNCs in solvents including pure DMF, pure water, and mixture of H_2O/DMF have been successfully prepared. The critical moisture (≥3.8 wt %) in CNC is required to disperse individual CNCs. Compared with pure solvents such as DMF and H_2O, H_2O/DMF co-solvent can more effectively disperse individual CNC. This co-solvent system will help in achieving better dispersions of CNCs in both hydrophilic and hydrophobic polymer matrices.

CHAPTER 3. GEL SPINING OF POLYACRYLONITRILE/CELLULOSE NANOCRYSTALS COMPOSITE FIBERS

3.1 Introduction

Gel spinning results in high strength and high modulus fibers due to low degree of polymer entanglement as compared to other spinning methods [10, 73]. CNCs with outstanding properties have been introduced in different polymer fibers such as poly (vinyl alcohol) (PVA), cellulose acetate and alginate fibers using electrospinning, dry spinning, or wet spinning [64, 65, 105]. Few studies have been conducted on polymer/CNC fibers utilizing gel spinning[106, 107]. Poly(vinyl alcohol), a hydrophilic polymer, is used in these studies and fibers show improved mechanical properties. In this chapter, as a hydrophobic polymer, PAN fibers containing up to 10 wt% CNC loadings were produced by gel spinning and the structure, morphology, and mechanical properties of these fibers were investigated.

3.2 Experimental Section

3.2.1 Materials

Polyacrylonitrile-co-methacrylic acid (PAN-co-MAA; 4 wt % of MAA content, viscosity average molecular weight: 2.5 X 10^5 g/mol) was obtained from Japan Exlan, Co. Dimethyl formamide (DMF) obtained from BDH, Inc. was purified by distillation before use.

3.2.2 Solution Preparation

As an example, a description of PAN/CNC 1wt % solution is given below. CNCs (0.225 g) were dispersed in DMF by sonication (Branson 3510R-MT, 100 W, 42 kHz) at a concentration of 75 mg/100 mL until an optically homogeneous dispersion was achieved. PAN polymer powder (22.225 g) was dried in a vacuum oven at 100 °C for 24 hours and then dissolved in DMF (150 mL) at 80 °C. The CNC/DMF dispersion was added to the PAN/DMF solution and the excess amount of solvent was evaporated by distillation to meet the desired solid content in the solvent (15 g solids (PAN+CNC)/100 mL solvent). PAN/CNC solution at 5, and 10 wt % CNC were prepared using similar protocol and control PAN solution was also prepared at the same solid concentration. However, no solvent evaporation step was involved in control PAN solution preparation. The solid content in all cases was 15 g (PAN+CNC) per 100 mL of solvent. In the following study, composites containing 1, 5, and 10 wt% CNCs will be referred to as PAN/CNC-1, PAN/CNC-5, and PAN/CNC-10.

3.2.3 Fiber Spinning

The control PAN fiber and PAN/CNC composite fibers were spun utilizing the gel spinning technique using a Hills, Inc. (Melbourne FL) spinning unit with a single hole (200 μm diameter) spinneret. The prepared solution was spun into a cold methanol gelation bath (-50 °C) with an air gap of 5 cm. The as-spun fibers were collected with a take-up roller (speed 32 m/min), followed by room temperature drawing. The second stage drawing was performed by passing the fiber through a glycerol bath maintained at 165 °C, followed by washing in methanol. To compare fiber properties under similar

processing conditions, both the control PAN and composite fibers were drawn to the same draw ratio. After drawing, fibers were then kept in oven at 60 °C for 3 days, prior to testing.

3.2.4 Characterization

Rheology frequency sweep tests were conducted using an ARES rheometer (Rheometric Scientific, Co.) with parallel plate geometry (50 mm plate diameter and 1 mm gap between plates) at room temperature. The angular frequency (ω) range was set from 0.1 to 300 rad/s at a fixed strain of 1 %. As-received CNCs and fracture surfaces of fibers were coated by gold and observed by scanning electron microscope (Zeiss Ultra-60 SEM operated at 5 kV). Dynamic mechanical tests were conducted on 32-filament bundles at 0.1, 1 and 10 Hz using a heating rate of 1 °C /min at a 25.4 mm gauge length using RSA III solids analyzer (Rheometric Scientific Co.). Single filament tensile testing was performed using a gauge length of 25.4 mm at a strain rate of 1%/s on FAVIMAT tensile testing instrument. For each fiber sample, at least 50 filaments were tested. Work of rupture is the area under the stress-strain curve. Densities of the composite fibers were estimated from the density of PAN[108] (1.18 g/cm^3) and CNC[21] (1.59 g/cm^3). Fourier transform infrared spectroscopy (FTIR) spectra from 4000 to 400 cm^{-1} of PAN and PAN/CNC fibers mixed with potassium bromide (KBr) pellets were recorded using a Magna 560 FTIR (Nicolet Instruments). A blank KBr pellet was used as the reference. Wide-angle X-ray diffractions (WAXD) of PAN and PAN/CNC composite fibers were investigated by a Rigaku MicroMax 002 X-ray generator to produce Kα radiation (λ = 1.5418 Å), equipped with a R-axis IV++ detector. The crystallinity was calculated by fitting the integrated scan using MDI Jade 8.5.2 software, and the crystal size was

calculated from the FWHM (Full Width at Half Maximum)of the crystalline peak from the equatorial scan using Sherrer equation.[109] The Herman's orientation factors of PAN crystal and CNCs were calculated from azimuthal scans of the PAN ($2\theta = 16.7°$) and CNC ($2\theta = 22.6°$) WAXD peaks following previously described methods.[110, 111]

3.3 Results and discussion

Complex viscosity of the PAN and PAN /CNC solutions are plotted in Figure 3.1 (a) as a function of angular frequency. The PAN solution showed Newtonian behavior at frequency below 2 rad/s. Above this frequency, PAN solution viscosity decreased with increasing frequency. However, for PAN/CNC solutions, the plateau disappeared even at the low CNC concentration of 1 wt %. All the samples containing CNC displayed a significant shear-thinning behavior. Similar phenomenon was observed in dilute CNC suspension and polymer/CNC mixture such as polyethylene oxide and polyurethane.[61, 112, 113] CNCs are randomly distributed in the PAN solution. This results in enhanced resistance to flow, as complex viscosity increases with increased CNC loading. At high frequency, the viscosity decreases due to alignment of polymer in the presence of CNC and the viscosity of the composite solution is lower than that for the control PAN polymer solution at the same solid content. Similar viscosity behavior is observed for polymer/CNT [114, 115] systems including PAN/CNT.[116]

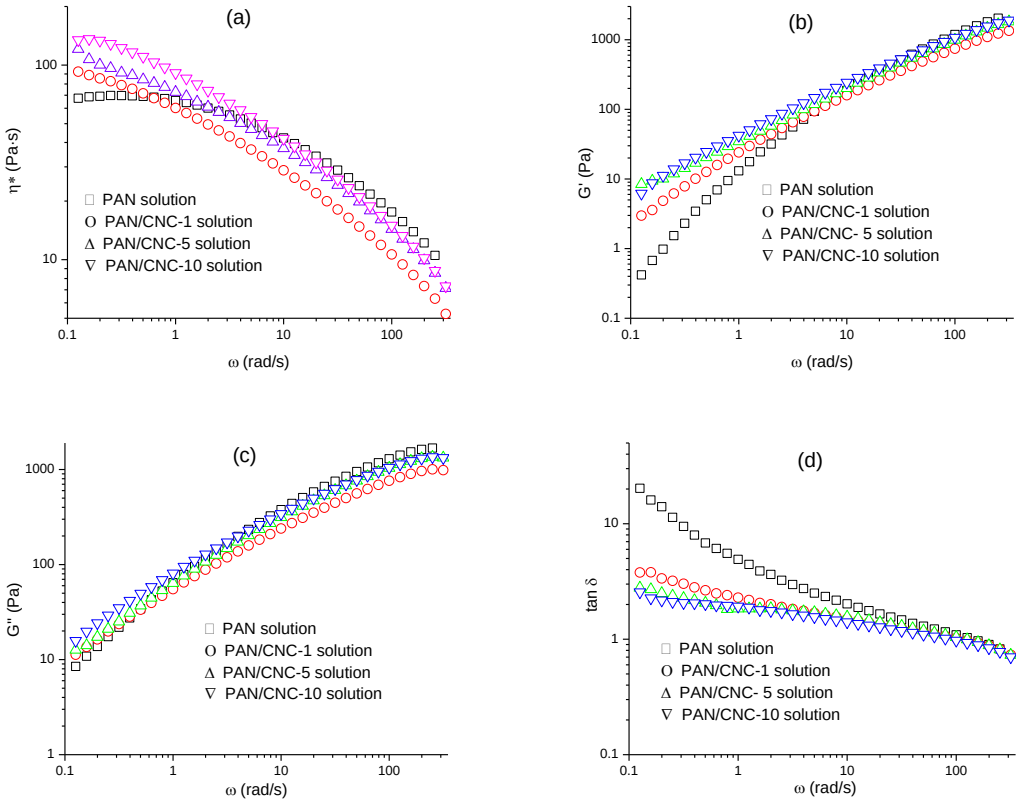

Figure 3.1. Rheological behavior of PAN and PAN/CNC solutions. (a) complex viscosity versus frequency, (b) storage modulus (G') versus frequency, (c) loss modulus (G'') versus frequency, and (d) Tan δ versus frequency.

Figure 3.1 (b) and (c) show the storage modulus (G') and the loss modulus (G") response as a function of angular frequency for PAN and PAN/CNC solutions. At a low frequency, the storage modulus increased by more than one order of magnitude as CNC loading increased to 10 wt %. At high frequencies, the storage modulus for all solutions is very comparable. At lower frequency, the loss modulus of the composite solutions is somewhat higher than that for the control PAN solution, while at higher frequency, the viscosity of the composite solutions is somewhat lower. However, this difference in the loss modulus between PAN and PAN/CNC solution was relatively small. Somewhat rigid structure of CNCs contributes more to the storage modulus than to the loss modulus. At

high frequency, the contribution from the PAN molecules becomes dominant since the network structure is broken due to alignment of CNC induced by high shear rate. When tan δ is smaller than one, sample behaves more like an elastic liquid. Figure 3.1 (d) shows the tan δ values as a function of angular frequency. The tan δ decreases as CNC loading increases at low angular frequencies. As discussed above, this is due to CNC network structure that is able to transmit elastic stresses when deformed [117].

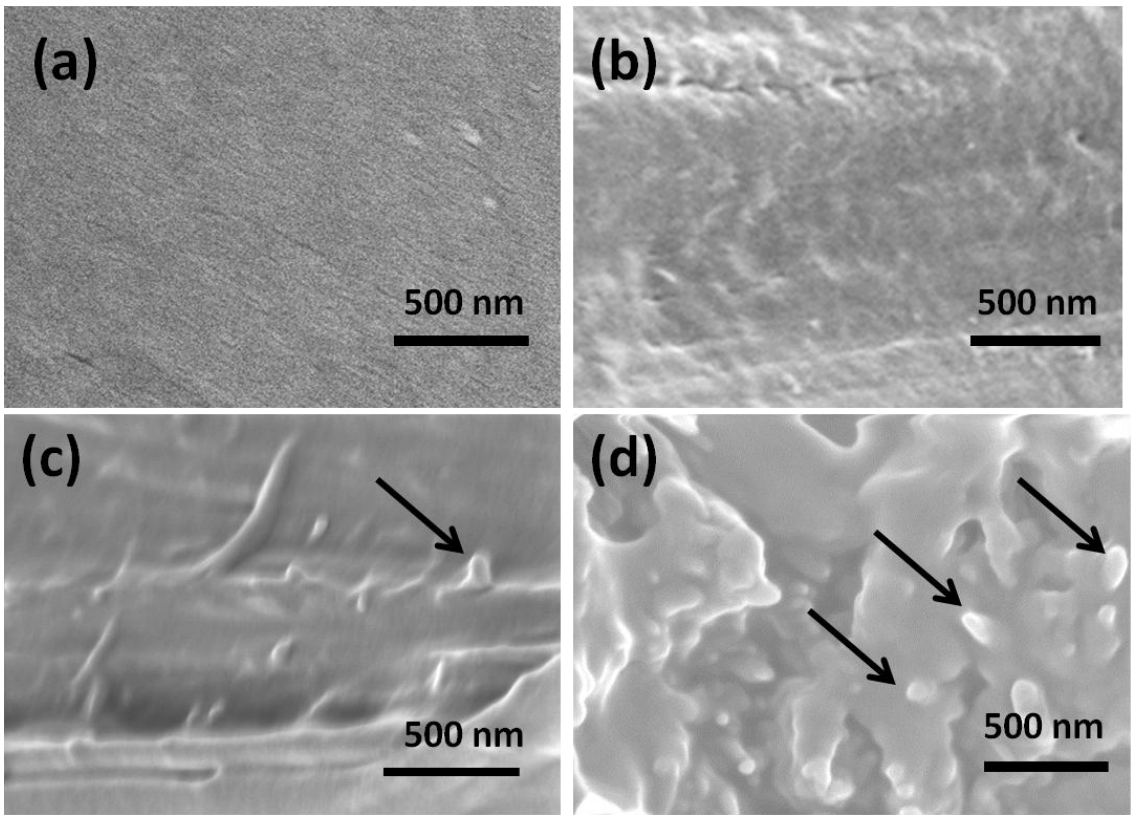

Figure 3.2. SEM images of fracture surface of fibers. (a) PAN, (b) PAN/CNC-1, (c) PAN/CNC-5, and (d) PAN/CNC-10. (arrows show the CNC).

The fracture surface of PAN and PAN/CNC composite fibers are shown in Figure 3.2. As compared to control PAN fiber, the fracture surface roughness of composite fibers increases due to the existence of CNC. In high CNC loading composite fibers,

CNC can be identified and its concentration on the fracture surface increases as CNC loading increases from 5 to 10 wt %.

The FTIR spectra of CNC, PAN fiber, and PAN/CNC fibers are presented in Figure 3.3. The vibrations characteristic of PAN structure are those of CN nitrile group at ca. 2243 - 2241 cm^{-1}, the band at 1732 cm^{-1} is attributed to the C=O stretching due to the presence of methacrylic acid, and the bands in the regions 2931 - 2870, 1460 - 1450, 1380 - 1350, and 1270 - 1220 cm^{-1} are assigned to the aliphatic CH group vibrations of different modes in CH, CH_2, and CH_3.[118] Characteristic absorbance peaks for the CNC are O-H stretching at ca. 3700 - 3100 cm^{-1}, the O-H bending of adsorbed water at 1651 cm^{-1}, the C-H stretching at 2900 cm^{-1}, and the C - OH deformation mode at 1034 cm^{-1}.[61] FTIR spectra of PAN/CNC fibers showed the characteristic absorption bands of CNC O-H peaks such as 3700 – 3100 cm^{-1} and 1034 cm^{-1} and these peaks become more obvious as the CNC loading increases in PAN/CNC composite fibers.

From WAXD studies, peak height and peak deconvolution methods are commonly used to determine crystallinity. The high crystallinity values (80 ~ 90 %) of CNCs were obtained by peak height method [119, 120]. However, the peak height method has several shortcomings [25] and this method overestimates crystallinity. In this study, the deconvolution method was used and the as-received CNCs crystallinity was determined to be 70 % (Figure 3.4).

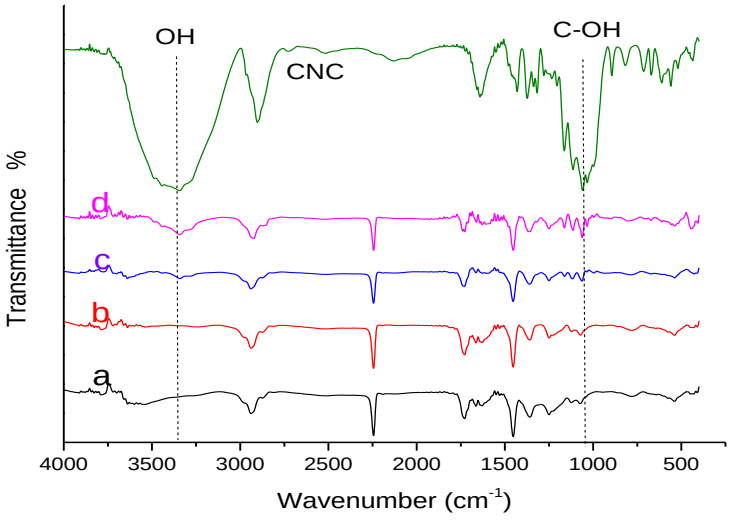

Figure 3.3. FTIR spectra of CNC and fibers. (a) PAN, (b) PAN/CNC-1, (c) PAN/CNC-5, and (d) PAN/CNC-10.

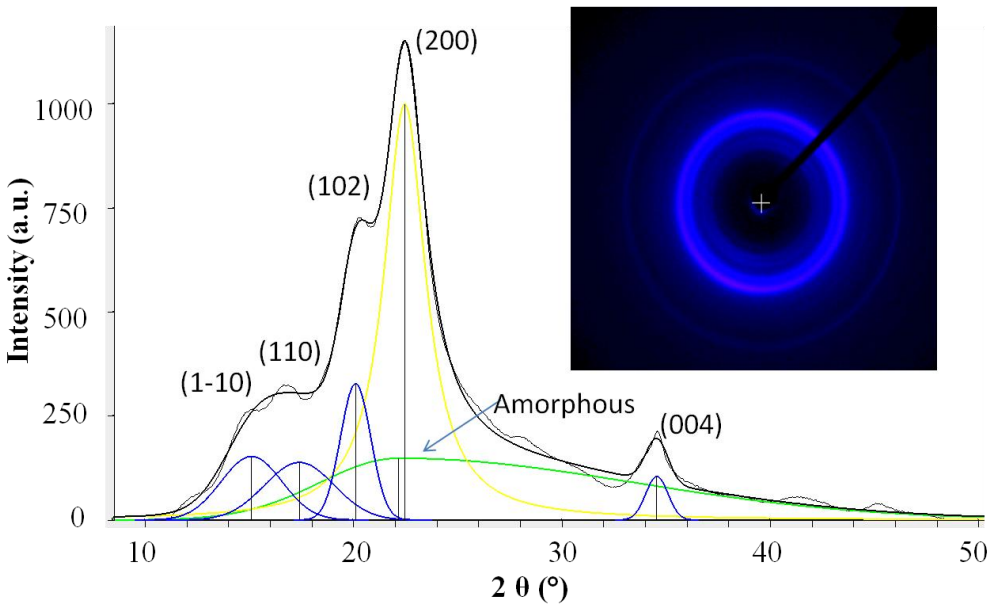

Figure 3.4. WAXD pattern and integrated radial scan of as-received CNCs.

The wide-angle X-ray diffraction (WAXD) patterns and equatorial WAXD scans of PAN and PAN/CNC fibers (Figure 3.5) confirmed that the CNCs were successfully incorporated into the PAN matrix. PAN is a semicrystalline polymer with characteristic

peak at 2θ = 16.7 °. With the addition of CNCs in the PAN matrix, a diffraction peak at 2θ = 22.6 ° appears. At 1 wt % CNC loading, the diffraction intensity of CNC peak is very weak. As CNC loadings increased to 5 and 10 wt %, the PAN/CNC composite fibers show a clear peak at 2θ = 22.6 °, attributed to the (200) plane of the CNCs. The calculated PAN crystallinity in control PAN fiber is 50 %. PAN crystallinity in composite fibers increases from 50 to 62 % as CNC loading increases from 0 to 10 wt % (Table 1). PAN/CNC 1 and 5 wt % CNC loaded composite fibers show higher PAN crystallite orientation factor (0.89) than that in the control PAN fiber (0.85). For composite fiber with 10 wt % CNCs, the PAN orientation factor (0.85) is comparable to that of the control PAN fiber.

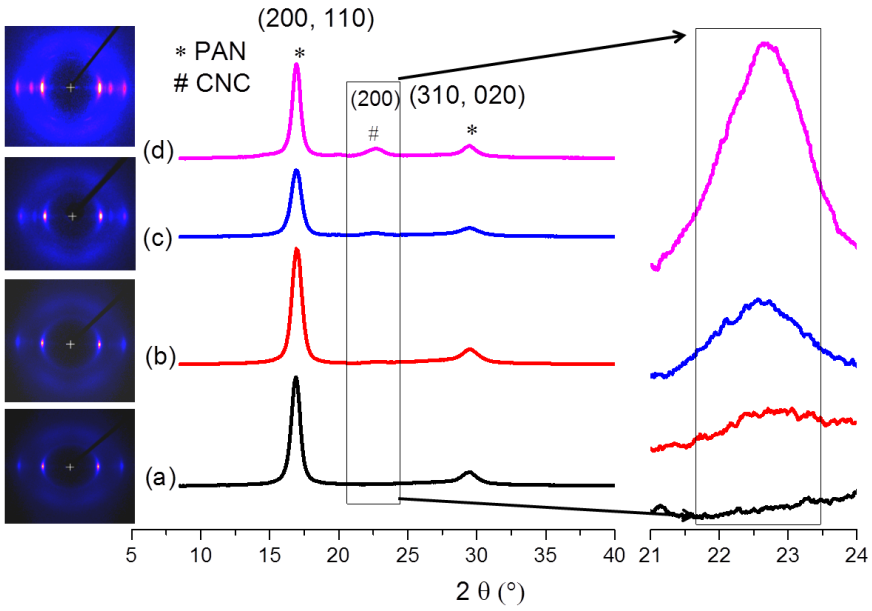

Figure 3.5. WAXD patterns and equatorial scans of fibers. (a) PAN, (b) PAN/CNC-1, (c) PAN/CNC-5, (d) PAN/CNC-10.

Due to different spinning method, polymer matrix and CNC assembly behavior, the orientation of CNC differs in different polymer fiber as the CNC concentration

increases. In cellulose acetate fiber, Herman's order parameter of CNC increases as CNC content increases in fiber, which results in higher mechanical properties in composite fibers.[65] However, in alginate fiber, the Herman's order parameter decreases as CNC loading increases. Based on WAXD analysis, Urena-Benavides et al. claim that CNCs try to twist during fiber spinning, which is accentuated as CNCs loading is increased. This structure results in a reduction in tenacity and modulus, and an increase in elongation at break.[111]

If WAXD meridional peak position of PAN fibers shifts to lower value (2θ in the range of 40° to 36 °), it suggests more zigzag sequence of PAN, and when it shifts to higher 2θ value, then it suggests more helical sequences.[9, 121] Meridional peak shifts to lower 2θ value as the CNC content increases in PAN/CNC composite fibers (Table 1), and this suggests more planar zigzag PAN sequences in the composite fibers as compared to the control fiber. Thus the prevalence of extended PAN chain conformation increases in high CNC loaded composite fibers, which contributes to composite fiber modulus improvement.

Fiber tensile properties are listed in Table 3.1. Tensile modulus and work of rupture of PAN/CNC composite fibers increases from 14.5 to 19.6 GPa and from 30 to 39 MPa, respectively, as CNC loading increases from 0 to 10 wt %. The PAN/CNC fiber with 5 wt % CNCs loading show highest tensile strength at 733 MPa, a 17 % increase as compared to that of the control PAN fiber of the same draw ratio. The elongation at break of composite fibers is very comparable to that of the control fiber. Higher PAN crystallinity in PAN/ CNC fibers as compared to PAN fiber can at least partially account

for improved mechanical properties in the composite fiber. Improved PAN molecular alignment and the presence of CNC also contribute to enhanced mechanical properties.

It was reported that the addition of CNCs into the polymer matrix, such as poly acrylic acid, cellulose acetate and waterborne polyurethane, increases the tensile strength and modulus but decrease the elongation at break.[41, 57, 65] However, for PAN/CNC composite fibers, the increased tensile strength and modulus values were not at the expense of elongation at break. It was demonstrated that nano-fillers can provide load transfer across the filler-matrix interface, thus toughening the composite materials.[77] As observed from the SEM images of the fracture surfaces, pull-out CNCs can be observed, indicating load transfer across the CNC/PAN interface during elongation. This may explain why PAN/CNC composite fibers show improved tensile strength and tensile modulus and maintain the elongation at break.

Dynamic mechanical storage modulus and tan δ plots for the drawn fibers at 10 Hz frequency are shown in Figures 3.6 and 3.7. For PAN fibers, the storage modulus decreases slightly with temperature at low temperature (below 80 °C). When temperature increased to 80 °C, storage modulus significantly dropped where a typical β_c transition appeared.[122] The storage modulus of PAN/CNC composite fibers increases as the CNC loading is increased from 0 to 10%. The storage modulus of PAN/CNC 10 wt % fiber increases by about 50 % as compared to the control PAN fiber at 30 °C. This is qualitatively consistent with the tensile modulus results at room temperature.

Table 3.1. Mechanical properties and structural parameters of PAN and PAN/CNC composite fibers.

	PAN	PAN/CNC-1	PAN/CNC-5	PAN/CNC-10
Draw ratio (DR) [+]	10	10	10	10
Linear density (dtex)	3.7 ± 0.3	3.4 ± 0.3	3.2 ± 0.4	3.6 ± 0.8
Calculated density (g/cm^3)	1.18	1.18	1.20	1.22
Effective diameter (μm)	20.1 ± 0.8	19.2 ± 0.8	18.3 ± 1.2	19.3 ± 2.3
Modulus (GPa)	14.5 ± 0.9	15.7 ± 0.7	17.5 ± 1.4	19.6 ± 1.3
Strength at break (MPa)	624 ± 61	612 ± 71	733 ± 91	709 ± 98
Elongation at break (% strain)	8.9 ± 0.5	8.4 ± 1.1	8.8 ± 0.5	9.5 ± 0.9
Work of rupture (MPa)	30.5 ± 3.6	30.0 ± 6.1	34.6 ± 5.0	39.1 ± 4.9
PAN crystallinity (%)	50	53	59	62
PAN crystal size (nm)	11.7	10.5	9.8	11.8
f^*_{PAN}	0.85	0.89	0.89	0.85
f^*_{CNC}	-	-	0.90	0.90
$PAN_{2\theta meridional}$ [#]	39.8	39.7	39.4	38.9

[+] DR= (as spun 1x) x (cold drawn 2x) x (hot drawn 5x)
*Herman's orientation factor, [#] meridional peak position

The tan δ peak temperature (Tg) increased from 93 °C for the control PAN fiber to 103 °C for the PAN/CNC 10 wt % composite fiber. The magnitude of tan δ peak decreased from 0.15 for the control PAN fiber to below 0.12 for the PAN/CNC composite fibers. In the PAN/CNC composite fibers, it is believed that high crystallinity and rigid rod-like CNCs can effectively constrain the PAN chain mobility, which results in relatively higher activation energy and increased β_c transition temperature. The activation energy for the dynamic mechanical transition for PAN and PAN/CNC fibers in the current study is calculated using Arrhenius plot. The observed glass transition temperature (tan δ peak temperature) depended on the test frequency,

$$\mathrm{Ln}(f) = \mathrm{Ln}(A) - \frac{Ea}{RT}, \qquad (3.1)$$

where f is frequency, A is the pre-exponential factor, T is temperature, and Ea is activation energy. By plotting the natural logarithm of frequency versus 1/T, the slope can be used to calculate the activation energy. As shown in Figure 3.8, the calculated activation energy of glass transition is higher in the composite fibers than that in the control PAN fibers and it increases as CNC loading increases.

Previous research showed that βc relaxation of PAN with more planar zigzag sequences exhibited lower tan δ peak.[123] Based on WAXD analysis, the high alignment of CNCs helps to align PAN chain orientation. Therefore more planar zigzag sequence will be present in PAN/CNC composite fiber, which is confirmed by decreased meridional 2θ peak position in the PAN/CNC composite fibers as compared to the control PAN fiber (Table 1). In summary, high PAN crystallinity and rigid rod-like CNCs in

PAN fibers can restrain PAN chain mobility and help to extend PAN chain, which results in higher tan δ peak temperature, and lower magnitude of βc relaxation.

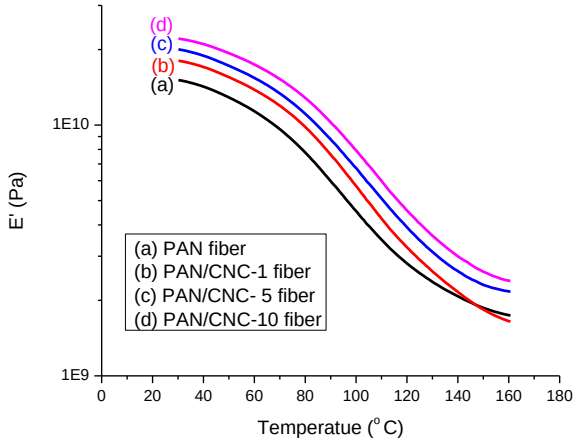

Figure 3.6. Dynamic mechanical storage modulus of PAN and PAN/CNC fibers at a frequency of 10 Hz.

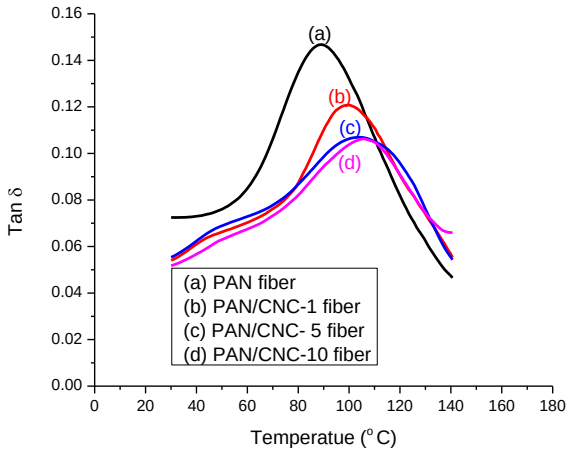

Figure 3.7. Dynamic mechanical tan δ of PAN and PAN/CNC fibers at a frequency of 10 Hz.

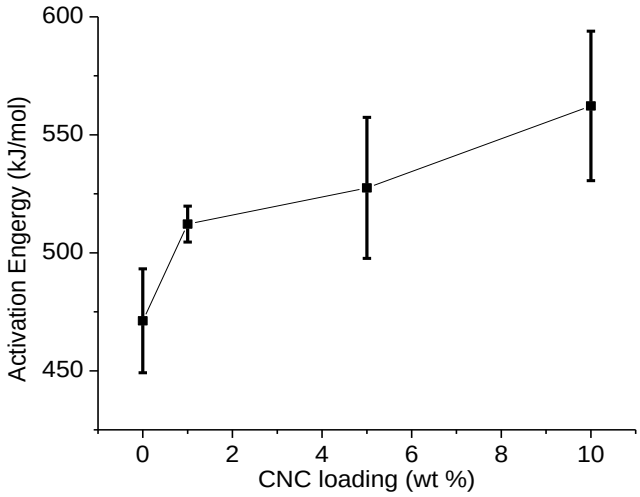

Figure 3.8. Activation energy of dynamic mechanical transition in PAN and PAN/CNC composite fibers.

3.4 Conclusions

The PAN solution rheological properties are affected with the incorporation of CNCs. With the presence of CNC, solution behavior changes from newtonian fluid to shear-thinning fluid at lower angular frequency. PAN/CNC composite fibers were successfully spun by gel spinning method. Compared with the control PAN fiber, incorporation of CNC into PAN matrix contributes to PAN alignment and increases PAN crystallinity. Composite fiber with 5 wt % CNC loading showed highest tensile strength at 733 MPa, a 17 % increase as compared to that of control PAN fiber. Composite fiber with 10 wt % CNC loading showed highest tensile modulus at 19.6 GPa, a 35 % increase as compared to that of control PAN fiber.

CHAPTER 4. DUCTILE POLYACRYLONITRILE FIBERS WITH HIGH CELLULOSE NANOCRYSTALS LOADING

4.1 Introduction

One drawback of nanocomposites is that the elongation at break of the nanocomposites decreases with increasing concentration of fillers in the polymer, as compared to the control polymer [54, 56, 57]. For example, the elongation at break of PAN film significantly decreased from 27% without any CNCs to 4% with 40 wt% CNCs[56]. Therefore, it is still a challenge to make ductile polymer nanocomposites with high CNC loading. In chapter 2, dimethylformamide(DMF)/H_2O cosovlent system has been shown to individually disperse CNCs. In this chapter, we use this co-solvent approach to process PAN/CNC fibers. Structure and properties of various draw ratios of PAN and PAN/CNC fibers with up to 40 wt% CNC loading have been systematically investigated, and it has been show that the fully drawn PAN/CNC fibers at all CNC concentrations show practically no loss in strain to failure when compared to the control PAN fiber at the highest draw ratio.

4.2 Experimental

Materials and solution preparation of PAN, PAN/CNC-1, PAN/CNC-5 and PAN/CNC-10 are described in chapter 3. For 20 and 40 wt% CNC loading in PAN solution, CNCs was dispersed in DMF/H_2O (75/25 ratio by volume) mixture at a concentration of 3 g/100 mL, as this solvent mixture has been effectively shown to disperse individual CNCs in chapter 2. Then CNC/DMF/H_2O dispersion was added to

PAN/DMF solution and the excess amount of solvent was evaporated by distillation to achieve the same solid concentration as in control PAN solution. Excessive presence of H_2O from CNC/DMF/H_2O mixture in PAN/DMF solution can deteriorate solution homogeneity. Therefore, CNC/DMF/H_2O mixture was added stepwise in the PAN/DMF solution, followed by partial solvent evaporation. This process was repeated multiple times, until all the required CNCs have been added. The detailed preparation conditions are summarized in Table 4.1. Rheological data of PAN and various PAN/CNC solutions is plotted in Figure 4.1. In the following study, composites containing 1, 5, 10, 20, and 40 wt% CNCs will be referred to as PAN/CNC-1, PAN/CNC-5, PAN/CNC-10, PAN/CNC-20, and PAN/CNC-40.

Table 4.1. Solution preparation conditions.

Solutions	PAN (g)	CNCs (g)	CNC dispersion solvent	CNC dispersion concentration (g/ 100 mL)	CNC sonication Time (hours)
PAN	15.00	0	-	-	-
PAN/CNC-1	14.85	0.15	DMF	0.075	24
PAN/CNC-5	14.25	0.75	DMF	0.075	24
PAN/CNC-10	13.50	1.50	DMF	0.075	24
PAN/CNC-20	12.00	3.00	DMF/H_2O (75/25) #	3	48
PAN/CNC-40	9.00	6.00	DMF/H_2O (75/25) #	3	48

Volume percent

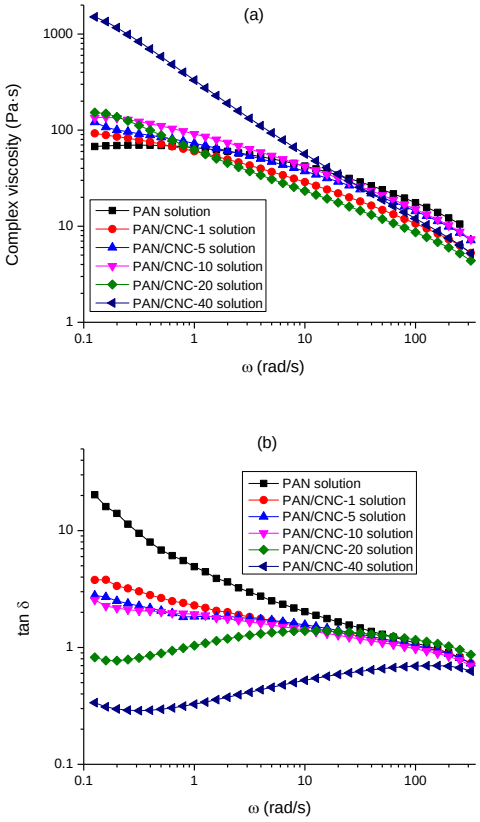

Figure 4.1. Rheological behavior of PAN and PAN/CNC solutions. (a) complex viscosity versus angular velocity and (b) tan δ versus angular velocity.

The prepared solutions were spun using a spinning system (Hills, Inc. Melbourne FL) equipped with a single-hole spinneret of 200 μm diameter. The solution was spun into a methanol bath maintained at −50 °C using an air gap of about 5 cm. The as-spun draw ratio was 3 and the as-spun fibers were followed by first-stage drawing at room temperature (draw ratio 1.3). Then second-stage drawing was performed by passing the fiber through a glycerol bath (165 °C) and then washed by methanol. The draw ratios of fibers are listed in Table 4.2.

Table 4.2. Draw ratios of PAN and PAN/CNC fibers.

	Total draw ratio				Maximum draw ratio
PAN	4x	15x	20x	23x	23x
PAN/CNC-1	4x	15x	20x	23x	26x
PAN/CNC-5	4x	15x	20x	23x	23x
PAN/CNC-10	4x	15x	20x	23x	23x
PAN/CNC-20	4x	15x	20x	23x	29x
PAN/CNC-40	4x	*	20x	23x	29x

*: data is not available

Transmission electron microscopy (TEM) image of CNCs were obtained using scanning/transmission electron microscope JEOL JEM-ARM200cF (JEOL, Ltd, Tokyo, Japan) operated at 80 keV. Raman spectra were collected on a single fiber using a 785 nm laser on a Raman microscope system from HORIBA Scientific. For SEM, fiber bundles were embedded in epoxy resin (Epo-Fix, Electron Microscopy Sciences) and then sliced into 10-15 μm thick sections using a microtome (Leica, RM2255). The fiber cross-sections were characterized by scanning electron microscopy (Zeiss Ultra-60 SEM operated at 5 kV). Single filament tensile testing was done at a gauge length at 25.4 mm at a strain rate of 1%/second using FAVIMAT tensile testing instrument. The linear densities of the fibers were measured by an inline vibroscope prior to tensile testing. The measured linear density was converted to an effective fiber diameter using the calculated fiber density. For each fiber sample, at least 20 filaments were tested for tensile properties. Dynamic mechanical tests were conducted on 32 filament bundles at a

frequency of 10 Hz using a heating rate of 1 °C /min at 25.4 mm gauge length using RSA III solids analyzer (Rheometric Scientific Co.).

The crystallinity, Xc, of PAN in composite fibers was calculated using Equation:

$$X_c(\%) = \left(\frac{A_c}{A_c + A_a}\right) \times 100 \qquad (4.1)$$

where A_c and A_a represents the PAN crystalline and amorphous areas, respectively, of deconvoluted XRD patterns. The CNC crystalline area (from the peak fitting) and amorphous region were excluded. Herman's orientation factor (f) was calculated from $I(\phi)$ based on the procedure described elsewhere[111], where intensity from (200) planes in PAN and in CNCs are used.

4.3 Results and discussion

The cross-sections of PAN and PAN/CNC-40 fibers are shown in Figure 4.2. CNCs can be seen protruding in the composite fiber cross-section, while such morphology is not observed in the control PAN fiber. Both the PAN and PAN/CNC fibers exhibited similar cross-sectional shape, which looks like the shape of a kidney bean. Fiber linear density ranged from 0.9 to 13.6 dtex and the calculated effective diameters ranged from 9.5 to 25.8 μm. The linear density and calculated effective diameter of various fibers at various draw ratios are listed in Table 4.3 and Table 4.4.

Table 4.3. Linear density (dtex) of PAN and PAN/CNC fibers at various draw ratios.

Draw ratio	4x	15x	20x	23x	Maximum draw ratio[#]
PAN fiber	9.4 ± 0.9	2.1 ± 0.1	1.8 ± 0.2	1.8 ± 0.2	1.8 ± 0.2 (23x)
PAN/CNC-1	8.0 ± 0.8	2.5 ± 0.3	1.8 ± 0.2	1.6 ± 0.3	1.3 ± 0.2 (26x)
PAN/CNC-5	8.6 ± 1.3	2.3 ± 0.5	1.6 ± 0.3	1.4 ± 0.3	1.4 ± 0.3 (23x)
PAN/CNC-10	9.8 ± 2.1	2.3 ± 0.6	1.8 ± 0.3	1.4 ± 0.5	1.4 ± 0.5 (23x)
PAN/CNC-20	7.9 ± 0.9	2.2 ± 0.1	1.3 ± 0.1	1.2 ± 0.1	0.9 ± 0.1 (29x)
PAN/CNC-40	13.6 ± 0.9	※	2.7 ± 0.2	2.2 ± 0.1	1.8 ± 0.1 (29x)

Maximum draw ratio is in the bracket
※ Data is not available

Table 4.4. Effective diameter (μm) of PAN and PAN/CNC fibers at various draw ratios calculated from linear density.

Draw ratio	4x	15x	20x	23x	Maximum draw ratio[#]
PAN fiber	31.7 ± 1.5	15.0 ± 0.5	14.0 ± 0.9	13.9 ± 0.7	13.9 ± 0.7 (23x)
PAN/CNC-1	29.3 ± 1.5[a]	16.9 ± 0.8	14.0 ± 0.7	13.2 ± 1.0	11.6 ± 1.0 (26x)
PAN/CNC-5	30.2 ± 2.2	15.4 ± 2.0	13.1 ± 1.4	12.0 ± 1.3	12.0 ± 1.3 (23x)
PAN/CNC-10	31.9 ± 3.3	15.5 ± 2.1	13.6 ± 1.1	11.9 ± 2.0	11.9 ± 2.0 (23x)
PAN/CNC-20	28.2 ± 1.6	15.0 ± 0.2	12.4 ± 0.4	11.1 ± 0.4	9.5 ± 0.4 (29x)
PAN/CNC-40	35.8 ± 1.2	※	15.9 ± 0.5	14.3 ± 0.4	12.9 ± 0.4 (29x)

Maximum draw ratio is in the bracket
※ Data is not available
[a] Densities of the composite fibers were estimated from the density of PAN (1.18 g/cm^3) and CNC (1.59 g/cm^3)

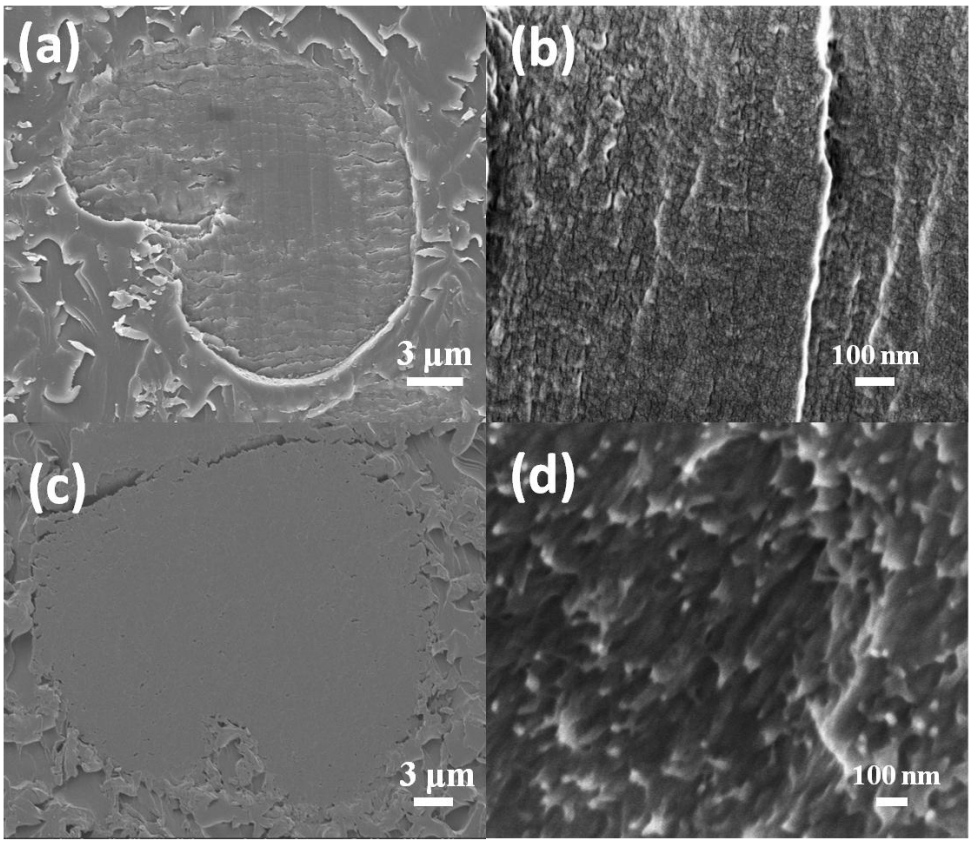

Figure 4.2. Representative SEM images of cross-sections of (a, b) PAN, and (c,d) PAN/CNC-40 fibers with draw ratio of 4.

Raman spectroscopy has been used to investigate cellulosic materials[71, 124]. Cellulose exhibits well-defined 1095 cm^{-1} Raman band, which is associated with C-O ring stretching of the cellulose backbone. Raman spectra of PAN and PAN/CNC fibers were collected from 1000 to 1200 cm^{-1}. As shown in Figure 4.3, PAN fiber does not exhibit any peak in the range of 1000-1200 cm^{-1}. Also, PAN/CNC composite fibers do not show CNC Raman peak at low CNC concentrations of up to 10 wt%. At higher CNC concentrations of 20 and 40 wt%, 1095 cm^{-1} cellulose Raman band can be observed, and thus can be used to determine CNC orientation in the composite fibers.

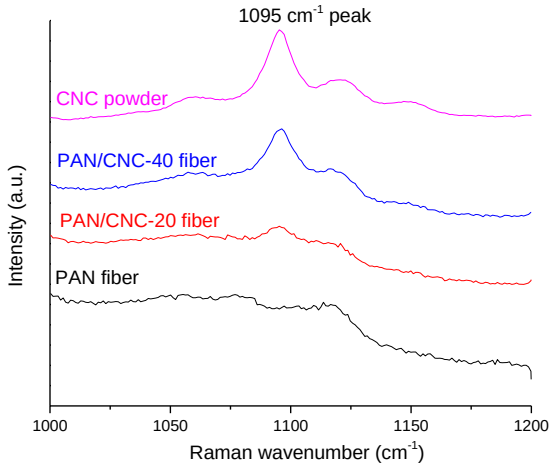

Figure 4.3. Raman spectra of PAN and PAN/CNC fibers.

Crystal structure of polyacrylonitrile (PAN) is reported to be either hexagonal or orthorhombic (pseudohexagonal) [16, 125, 126]. Schematic of the possible PAN crystal structures was shown in Figure 4.4. Figure 4.4 (a) represents hexagonal packing in which a unit cell with the ratio of axes a/b = $\sqrt{3}$ (or 1.732) where a is the d-spacing between (200) planes and b is the d-spacing between (020) planes. Figure 4.4 (b) represents orthorhombic structure where a/b ratio is less than 1.732. In previous study, it was shown that the a/b ratio (1.705) of as-spun PAN fiber is less than the value (1.732) for hexagonal packing and this ratio approaches the value 1.732 upon drawing the PAN fiber [9]. WAXD patterns for PAN and PAN/CNC-40 with 23x draw ratio fibers are given in Figure 4.5 and WAXD patterns for all the fibers are given in Figure A.1 (Appendix A). PAN (200, 110) at 2θ ~ 17° is the strongest peak. As shown in WAXD equatorial scans in Figure 4.6 (A), the CNC (200) peak at 2θ ~ 22.5° becomes more obvious as the CNCs loading increases from 1 to 40 wt%. Structural parameters of PAN and PAN/CNC fibers with various draw ratios determined from WAXD are listed in Tables A.1 – A.6

(Appendix A). For the control PAN fibers, the d-spacing at 2θ ~ 17° and 30° decreased when draw ratio increased from 4x to 15x (Table A.1, Appendix A). In addition, a/b ratio approaches to 1.732 with increasing draw ratio (Figure 4.6 (B)). This is consistent with the literature reports[9, 121]. For PAN/CNC composite fibers with up to 10 wt% CNC loading, a/b ratio is lower than that of PAN fiber at 4x draw ratio and it approaches to 1.732 with increasing draw ratio. However, for PAN/CNC composite fibers with 20 and 40 wt% CNC loading, a/b ratios are significantly less than 1.732 even at high draw ratios. Therefore, the structure of the fully drawn PAN fiber, and PAN/CNC fiber (when CNC<10 wt%), are approaching hexagonal crystal structure, while in fully drawn PAN/CNC fibers at 20 and 40 wt% CNC, structure is orthorhombic crystals.

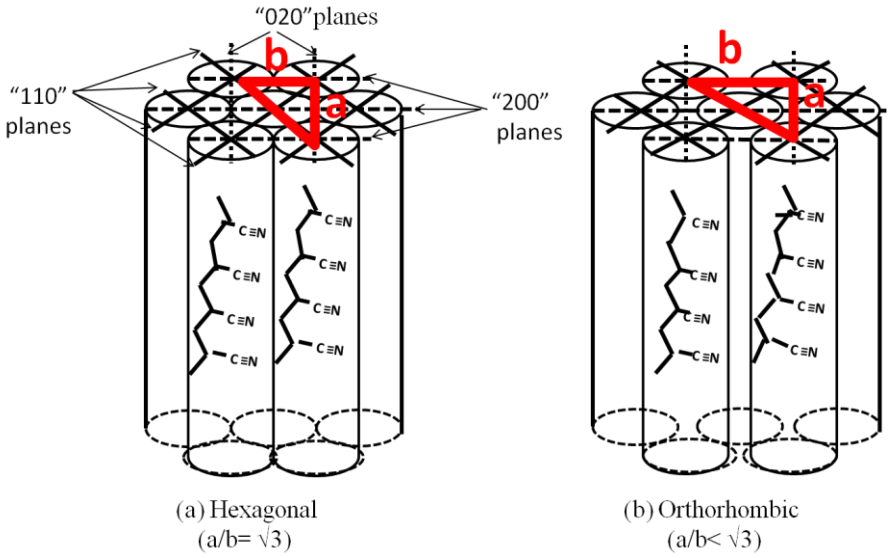

Figure 4.4. Schematic of the possible PAN crystal structures.

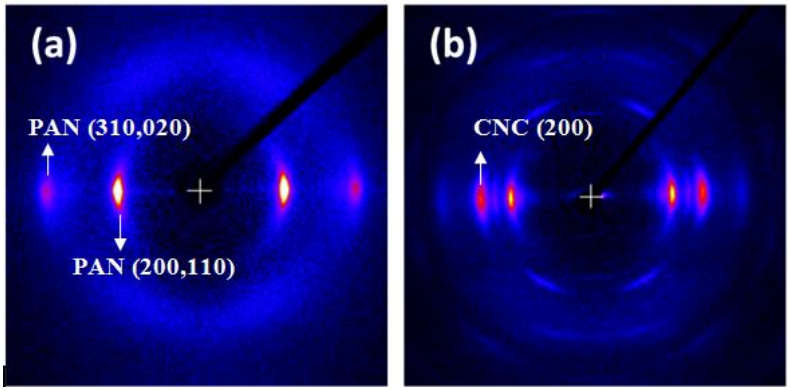

Figure 4.5. Representative WAXD patterns of (a) PAN fiber and (b) PAN/CNC-40 fiber.

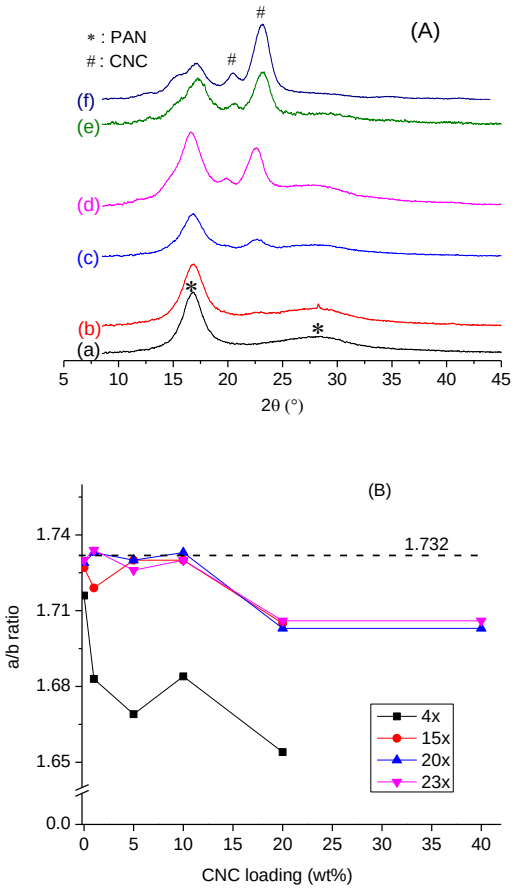

Figure 4.6. (A) WAXD equatorial scans of fibers: (a) PAN, (b) PAN/CNC-1, (c) PAN/CNC-5, (d) PAN/CNC-10, (e) PAN/CNC-20, and (f) PAN/CNC-40 (draw ratio = 4). (B) a/b ratio of PAN and PAN/CNC fibers with various draw ratios.

As seen from the data in Table 4.5 and Tables A.1 – A.6 (Appendix A), the f_{CNC} is significantly higher than f_{PAN} at low draw ratio (4x) and slightly higher at high draw ratios. The highly orientated CNCs help align the PAN chain in composite fibers. It has been shown that in meridional scan of PAN fibers, 2θ would shift to lower value (36° < 2θ < 40°) if more extended zigzag sequence appears in PAN based composite fibers[9, 121]. With the increase of CNC loading, meridional peak position shifts to lower value at a given draw ratio. At CNC loading of greater than 10 wt.%, PAN WAXD meridional peak (36° < 2θ < 40°) could not observed, while two meridional peaks at 2θ ~ 17.2° and 35.5° are observed resulting from (002) and (004) diffractions in cellulose. In previous study, it showed that highly oriented cellulose exhibits mainly two strong distinct reflections of the (002) and (004) planes in the WAXD meridional scan [127] (Figure 4.7). This also shows that CNCs are highly oriented in PAN/CNC composite fibers.

Table 4.5. Structural parameters of PAN and PAN/CNC-10 fibers

	draw ratio	4x	15x	20x	23x
PAN fiber	f_{PAN}#	0.57	0.82	0.83	0.87
	Meridional peak position (2θ, degree)	39.8	39.1	39.1	39.0
PAN/CNC-10 fiber	f_{PAN}#	0.57	0.83	0.85	0.89
	f_{CNC}#	0.91	0.91	0.92	0.94
	Meridional peak position (2θ, degree)	*	38.3	38.3	*

f: Herman's orientation factor; * PAN peak is overlapped with CNC peak

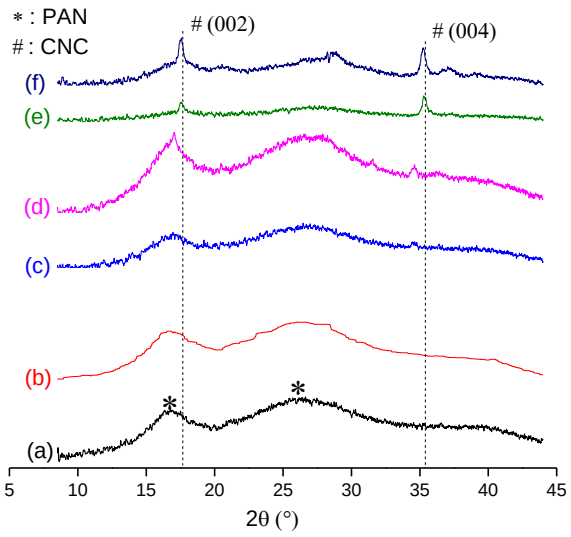

Figure 4.7. WAXD meridional scans of fibers at a draw ratio 4. (a) PAN, (b) PAN/CNC-1, (c) PAN/CNC-5, (d) PAN/CNC-10, (e) PAN/CNC-20, and (f) PAN/CNC-40.

As shown in Figure 4.8 (a), PAN crystallinity in PAN fibers and PAN/CNC composite fibers significantly increases as the draw ratio increases from 4x to 15x. For low draw ratio (4x), PAN crystallinity slightly increases in composite fibers compared to PAN fibers. At high draw ratios, PAN crystallinity is comparable in PAN and PAN/CNC fibers. PAN crystallite size in PAN and PAN/CNC fibers at high draw ratios (draw ratio of 15 or higher) is more than two times larger than at a draw ratio of 4 (Figure 4.8 (b)).

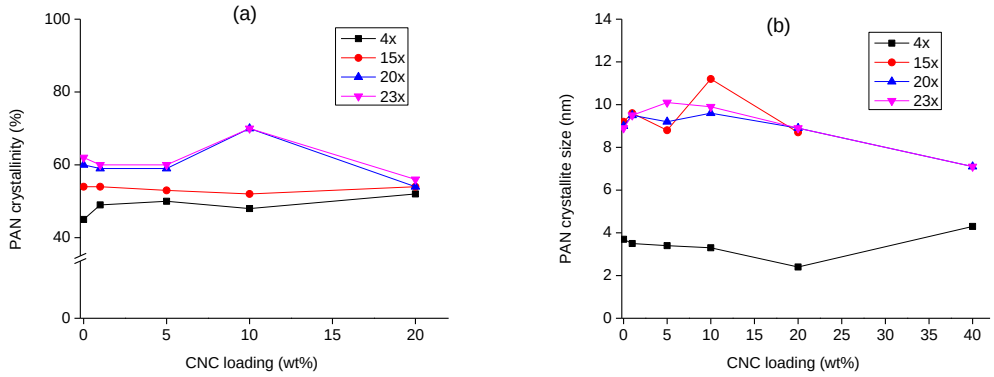

Figure 4.8. (a) PAN crystallinity and (b) PAN crystallite size ((200) plane) in PAN and PAN/CNC fibers.

The representative stress-strain curves of PAN and PAN/CNC fibers are shown in Figure 4.9. The mechanical properties of PAN and PAN/CNC fibers at various draw ratios are listed in Tables A.7 – A.10 (Appendix A). Tensile strength and tensile modulus of PAN and PAN/CNC fibers increase with the draw ratio increasing from 4x to 20x. As shown in Figure 4.10 (a), at 4x draw ratio, tensile strength of composite fibers slightly decreases as CNC loading increases. At their maximum draw ratio, the tensile strength of composite fiber is comparable to that of PAN fiber. As shown in Figure 4.10 (b), at 4x draw ratio, when CNC loading increases from 0 to 40 wt%, the tensile modulus of fibers significantly increases from 8.7 to 18.8 GPa. At maximum draw ratio, PAN/CNC-20 fiber shows the highest tensile modulus of 22.1 GPa compared to 17.8 GPa for PAN fibers.

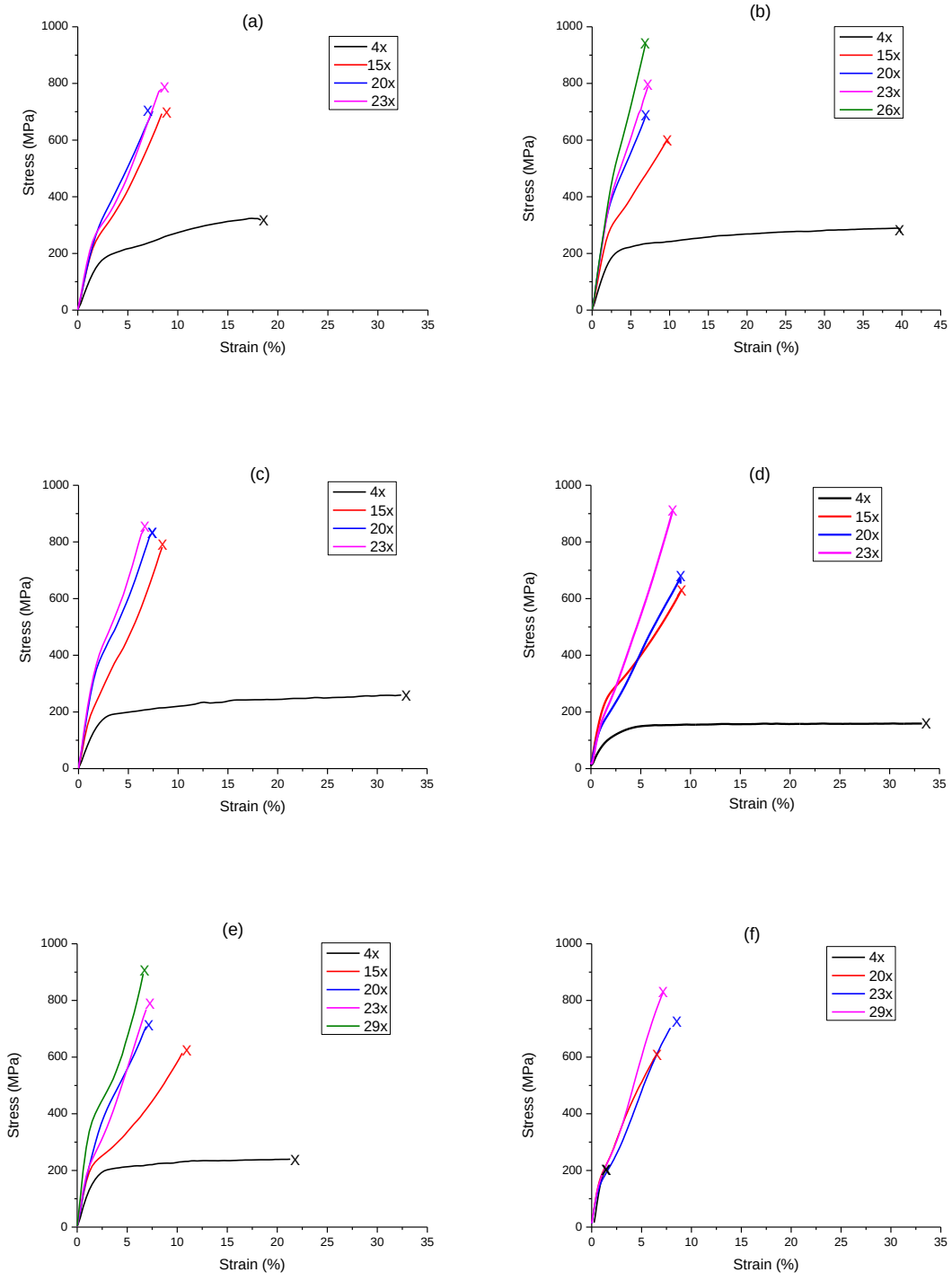

Figure 4.9. Representative stress-strain curves of PAN and PAN/CNC fibers with various draw ratios. (a) PAN fiber, (b) PAN/CNC-1 fiber, (c) PAN/CNC-5 fiber, (d) PAN/CNC-10 fiber, (e) PAN/CNC-20 fiber, and (f) PAN/CNC-40 fiber.

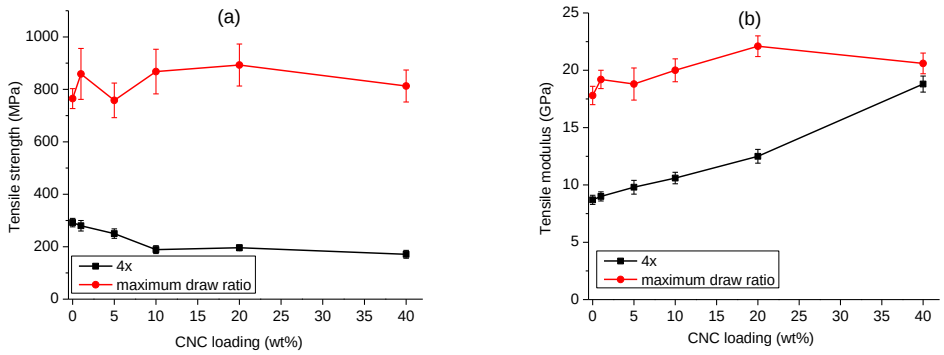

Figure 4.10. (a) Tensile strength and (b) tensile modulus of PAN and PAN/CNC fibers as a function of CNC loading.

For PAN and PAN/CNC fibers with up to 20 wt% CNC loading, elongation at break decreases with increasing draw ratio (Figure 4.11 (a)). At 4x draw ratio, the elongation at break is significantly higher in composite fibers (at ≤ 20 wt% CNC loading) than in PAN at the same draw ratio. At their maximum draw ratio, the elongation at break in PAN and all the PAN/CNC fibers is comparable to each other and is between 6.6 to 8.4%. However, at 4x draw ratio, the elongation at break for PAN/CNC-40 composite fiber is significantly lower at only 1.5%, while for PAN and the PAN/CNC fibers up to 20% CNC, it is in the range of 19 to 45%. Surprisingly, the elongation at break for PAN/CNC-40 composite fiber at the maximum draw ratio of 29x is 8%, and is comparable to the elongation at break for the other fibers.

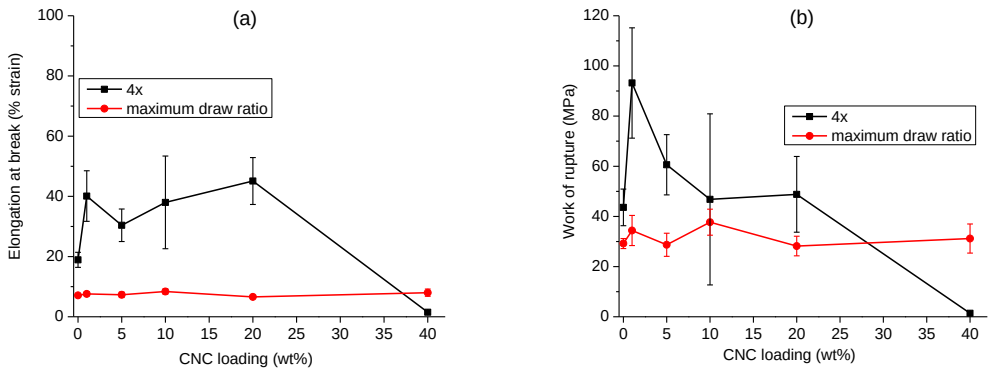

Figure 4.11. (a) Elongation at break and (b) work of rupture of PAN and PAN/CNC fibers as a function of CNC loading.

In PAN/CNC composite fibers at low draw ratio (e.g. 4x draw ratio) containing 40 wt.% CNC (33 volume % CNC), a CNC network is expected. As a result of this network, low strain to failure of only 1.5% is achieved. However, when this fiber is drawn to a draw ratio of 29x, CNCs align along the fiber axis, and thus the CNC interconnecting network points are reduced. In the process, the elongation at break for PAN/CNC-40 fiber increases from 1.5% at draw ratio of 4x to 8% at draw ratio of 29x. To the best of our knowledge, this is most likely the first study, where elongation to break increases with increased draw ratio and hence with increased orientation of both the polymer matrix and the nanofiller. As shown in Figure 4.11 (b), at 4x draw ratio, a small amount of CNC (1 wt% CNC) increases fiber's work of rupture by more than a factor of two, as compared to the control PAN fiber at the same draw ratio. On the other hand, at the maximum draw ratio, all fibers have the comparable work of rupture values.

For electrospun polystyrene and poly(vinyl alcohol) nanofibers containing 10 and 20 wt% CNCs, both oriented and unoriented regions of CNCs are found in the fibers based on TEM images [124]. Gel spun polyvinyl alcohol/CNC fibers with up to 60 wt%

CNC concentration have been reported [107]. At 40 wt % CNC loading, the strength and stiffness of fibers were 880 MPa and 29.9 GPa, respectively. However, the elongation at break of composite fibers significantly decreased from ~ 35 % to ~ 5 % as CNCs concentration increased from 0 to 40 wt%[107]. In our current PAN/CNC study, at their maximum draw ratio, elongation at break of PAN/CNC-40 composite fiber is comparable to that of the PAN fiber. This is attributed to the well-dispersed and highly oriented CNC in PAN fibers.

Figure 4.12(a) shows the storage moduli of PAN and PAN/CNC composite fibers with 4x draw ratio. The storage modulus of PAN fiber is increased with incorporation of CNCs, which is particularly significant at higher CNCs loading. For example, at lower temperature (30°C), the modulus of PAN/CNC-40 fiber is about 3 times of that of PAN fiber, which is quantitatively consistent with tensile tests results. β_c relaxation appears around tan δ peak temperature, which results from the molecular motion from helical sequences in the paracrystalline regions[9]. Also β_c relaxation of PAN with more planar zigzag sequences exhibited a lower magnitude and broader tan δ peak [123]. Figure 4.12 (b) shows the tan δ peaks of PAN and PAN/CNC composite fibers with 4x draw ratio. Lower tan δ peak magnitude and broader tan δ peak is observed as CNC loading increases in PAN/CNC composite fibers. This suggests that higher rod-like CNCs loading attribute to more zigzag sequences of PAN in the vicinity of CNC, which is consistent with the WAXD analysis.

Figure 4.12(c) shows the storage moduli of PAN and PAN/CNC composite fibers at their maximum draw ratio. Comparable to 4x draw ratio, PAN fiber and PAN/CNC composite fibers ($\leqq$20 wt% CNC) show significantly increased storage modulus at their

maximum draw ratio. At temperature of 30°C, storage modulus of fibers is increased with incorporation of CNCs, but the increase is relatively smaller compared with fibers with low draw ratio (4x). This is attributed to higher PAN crystallinity and orientation, which increases with the increasing draw ratio. At lower draw ratio, the storage modulus of high CNC loading composite fibers mainly depends on the CNCs where CNC modulus is higher than PAN. While at higher draw ratio, the PAN crystalline plays a significant role on the fiber's storage modulus. As shown in Figure 4.12(d), tan δ peak magnitude follows the similar trend with fibers at 4x draw ratio, which decreases with increasing CNC loading. β_c transition temperature increases as the CNC loading increases. Since the PAN crystallinity of PAN and PAN/CNC composite fibers is similar at high draw ratio, increased β_c transition temperature is mainly attributed to increased CNC concentration.

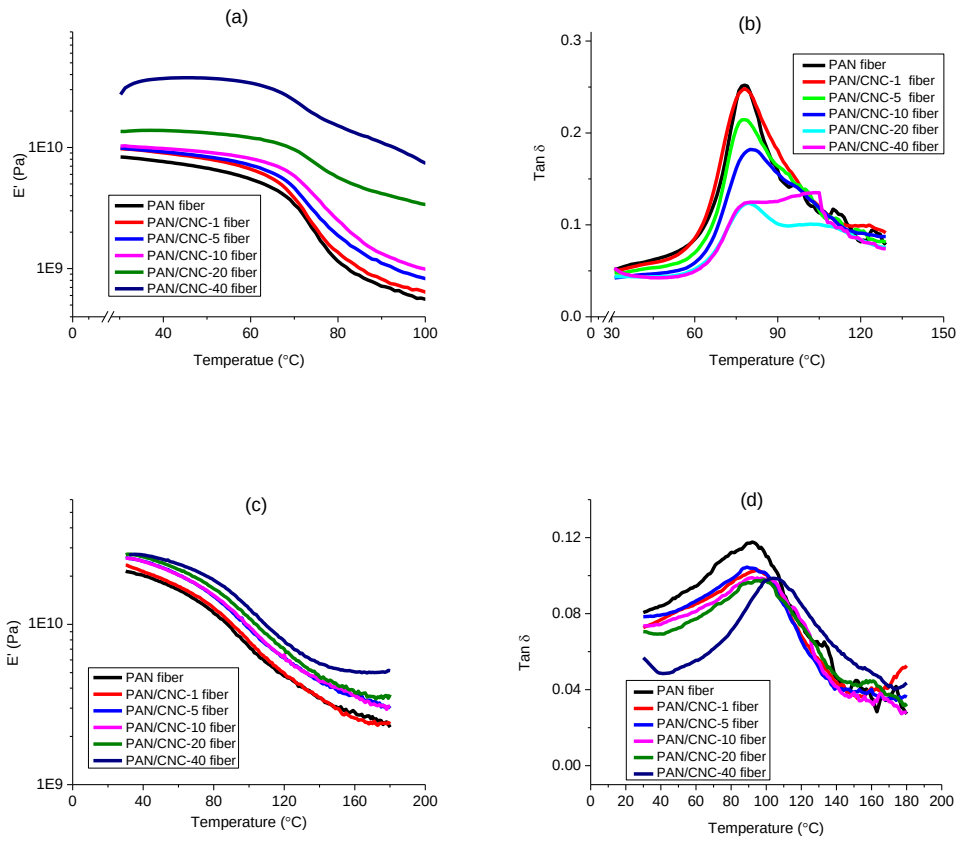

Figure 4.12. Storage modulus (E') and tan δ of PAN and PAN/CNC fibers. (a-b) at 4x draw ratio and (c-d) at maximum draw ratio.

4.4 Conclusions

PAN/CNC fibers with up to 40 wt% CNC were gel spun. The CNC reinforcement efficiency is more pronounced in fibers at low draw ratios. At a draw ratio of 4x, addition of CNCs to PAN fiber significantly increased work of rupture from 43.6MPa for the control PAN fiber to 93.2 MPa for PAN/CNC-1 composite fiber, and the tensile modulus increased from 8.7 GPa for the control PAN to 18.8 GPa for PAN/CNC-40 composite fiber. The drawing process increases PAN crystal size, PAN crystallinity and PAN crystallite orientation in all fibers, resulting in improved tensile strength and tensile modulus. Like other nanocomposite fibers, the drawing process decreases the elongation

at break of PAN/CNC fibers when CNC loading is up to 20 wt%. However, for PAN/CNC-40 composite fiber, the drawing process improves the PAN/CNC-40 composite fiber strain to failure from 1.5% for 4x draw ratio to 8.0 % for 29x draw ratio. Elongation at break of PAN/CNC-40 composite fibers at the highest draw ratio is comparable to the control PAN fiber also at its highest draw ratio. Dynamic mechanical tests show the same trend where storage modulus increases with increasing CNC loading. This high loading CNC reinforced composite fibers with good properties may expand the applications of CNCs in green nanocomposites.

CHAPTER 5. ORIENTATION AND INTERFACIAL STRESS TRANSFER OF CELLULOSE NANOCRYSTALS NANOCOMPOSITE FIBER

5.1 Introduction

Understanding the polymer/CNC interface and the orientation of CNCs in the fiber is important to explain and exploit their mechanical properties. High orientation of CNCs along the fibers axis is desired, as CNCs show much higher mechanical properties in axial direction than in the transverse direction. The stress transfer between PAN matrix and CNCs also affect the CNCs reinforcement efficiency. Polarized Raman spectroscopy is a powerful tool to characterize the orientation of CNCs in polymer composites as well as stress transfer between CNC and the polymer matrix. In this chapter, PAN fibers containing 20 and 40 wt% CNCs have been investigated using Raman spectroscopy to characterize CNC orientation and interfacial stress transfer between PAN and CNC.

5.2 Experimental

The solution preparation and fiber spinning can be found in chapter 4. Raman spectra were collected on a single fiber using a 785 nm laser on a Raman microscope system from HORIBA Scientific. The orientation of the CNCs in the composite fibers was determined using a rotation stage with fiber axis rotated in 10° increments from 0 to 360 ° under parallel (VV, vertical/vertical) and crossed (VH, vertical/horizontal) polarizers. In situ Raman deformation analysis of the fibers was conducted at a gauge length of 25 mm by mounting single fiber onto paper tabs and adhering with

cyanoacrylate adhesive. Fiber was strained in 25 μm steps using a stretching rig. Raman spectra were collected at each strain with fiber axis parallel to the polarized incident laser and analyzer. The spectral resolution is 0.4 cm^{-1}. At least four samples were tested to ensure data consistency. To minimize signal noise, an exposure time of 20 s was used and four spectra were accumulated for each measurement. Wide-angle X-ray diffraction (WAXD) of PAN/CNC composite fibers was conducted using Rigaku MicroMax 002 X-ray generator with Kα radiation (λ = 1.5418 Å), equipped with a R-axis IV++ detector. Herman's orientation factor (f) was calculated from $I(\phi)$ based on the procedure described elsewhere[111], where intensity from (200) planes in CNCs is used.

5.3 Results and discussions

5.3.1 CNC orientation in PAN/CNC fibers

Raman spectra were collected from PAN, CNC, and PAN/CNC composite films under VV configuration. A peak at approximately 1095 cm^{-1} was observed in CNC and PAN/CNC composite films, while PAN film did not show this peak (Figure 5.1). Therefore, the 1095 cm^{-1} Raman band of C-O ring stretching in cellulose can be used to characterize the CNC orientation in PAN/CNC fibers. The intensity of 1095 cm^{-1} Raman band of PAN/CNC 20 and 40 wt% composite films that are rotated in 10 ° increments from 0 to 360 ° is shown in Figures 5.2 (a) and 5.2 (b), respectively. The intensity is similar at all the rotation angles, which suggests that CNCs are isotropic in these composite films.

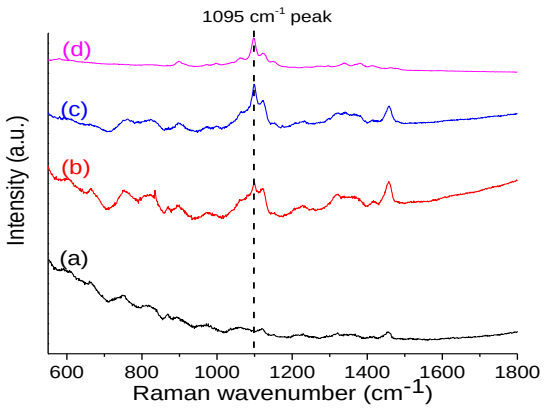

Figure 5.1. Raman spectra of various films. (a) PAN, (b) PAN/CNC 20 wt%, (c) PAN/CNC 40 wt%, and (d) CNC.

VV Raman spectra of PAN/CNC composite fibers are shown in Figures. 5.2c to 5.2f, and all the samples show angular dependence of 1095 cm^{-1} intensity. Similar phenomenon has been found in single-wall carbon nanotubes[128]. The maximum intensity of 1095 cm^{-1} occurs at 0 and 180°, where the fiber axis is parallel to laser polarization. When the fiber is rotated to 90 or 270°, the fiber axis is perpendicular to the direction of laser polarization, resulting in minimum intensity. In a previous study, it was shown that the intensity is proportional to $\cos^4\theta$ for the VV configuration[129], and can be expressed as[130] :

$$I = A \cos^4\theta + B \qquad (5.1)$$

where A and B are fitting parameters, and θ is the rotation angle and I is the intensity.

This equation has been used to fit the orientation data for different composites such as graphene oxide nanocomposites[18] and cellulose nanocrystals nanocomposite fibers[14]. It is suggested that parameter B related to un-oriented filler and B is supposed to approach to 0 for highly oriented filler in composites[130]. To characterize the CNC

orientation, the VV orientation data was fitted by the Equation 5.1. As given in Table 5.1, parameter A has comparable values in these fibers. While parameter B values approach zero as the fibers were drawn from 4x to 29x, which suggests that, as expected, stretching helps in aligning the CNCs in the composite fibers. Compared with previous study where A < 0.24 and B > 0.76 for CNC containing polystyrene and poly(vinyl alcohol) nanofibers [124], orientation of CNC in PAN/CNC composite fibers (A > 0.82 and B < 0.2) in this work is significantly higher.

In order to more accurately determine the CNC orientation, the following equation has been used: [9, 131]

$$I_{Fiber}^{VV}(\emptyset) \propto (\cos^4\emptyset - \frac{6}{7}\cos^2\emptyset + \frac{3}{35})\ \langle P_4(\cos\theta)\rangle\ + (\frac{6}{7}\cos^2\emptyset - \frac{2}{7})\ \langle P_2(\cos\theta)\rangle\ + \frac{1}{5} \quad (5.2)$$

where $\langle P_2(\cos\theta)\rangle = \frac{3\langle\cos^2\theta\rangle - 1}{2}$ represents the second order orientation parameter and is also known as Herman's orientation factor. $\langle P_4(\cos\theta)\rangle = \frac{35\langle\cos^4\theta\rangle - 30\langle\cos^2\theta\rangle + 3}{8}$ represents the fourth order orientation parameter. $\emptyset$ is the angle between the polarizer and fiber axis. θ is the angle between CNC axis and the fiber axis. The calculated orientation factors are summarized in Table 5.2. The as-spun PAN/CNC 40 wt% composite fiber with a draw ratio of 1 was also characterized and the second $\langle P_2(\cos\theta)\rangle$ and fourth $\langle P_4(\cos\theta)\rangle$ order orientation parameters are 0.78 and 0.75, respectively. This suggests that CNCs easily align even in the as spun fiber with no draw ratio, a result of flow through narrow spinneret capillary. CNC Herman's orientation factors determined from WAXD are also listed in Table 5.2.

Orientation factors calculated from Equation 5.1, Equation 5.2, and based on WAXD all confirm good CNC orientation in these fibers (Tables 5.1 and 5.2).

Table 5.1. Parameter values for fitting orientation data.

Composite fiber	A	B	R^2
PAN/CNC-20 (DR* = 4)	0.82	0.20	0.90
PAN/CNC-20 (DR= 29)	0.85	0.08	0.94
PAN/CNC-40 (DR= 4)	0.82	0.20	0.86
PAN/CNC-40 (DR=29)	0.85	0.10	0.94

*DR= draw ratio

Table 5.2. CNC orientation parameter.

Composite fiber	$\langle P_2(\cos\theta)\rangle$	$\langle P_4(\cos\theta)\rangle$	R^2	f_{CNC}#
PAN/CNC-20 (DR* = 4)	0.85	0.83	0.93	0.87
PAN/CNC-20 (DR= 29)	0.87	0.87	0.95	0.92
PAN/CNC-40 (DR= 4)	0.85	0.80	0.94	0.91
PAN/CNC-40 (DR=29)	0.87	0.85	0.96	0.91

*DR= draw ratio. #f= CNC Herman's orientation factor calculated from WAXD.

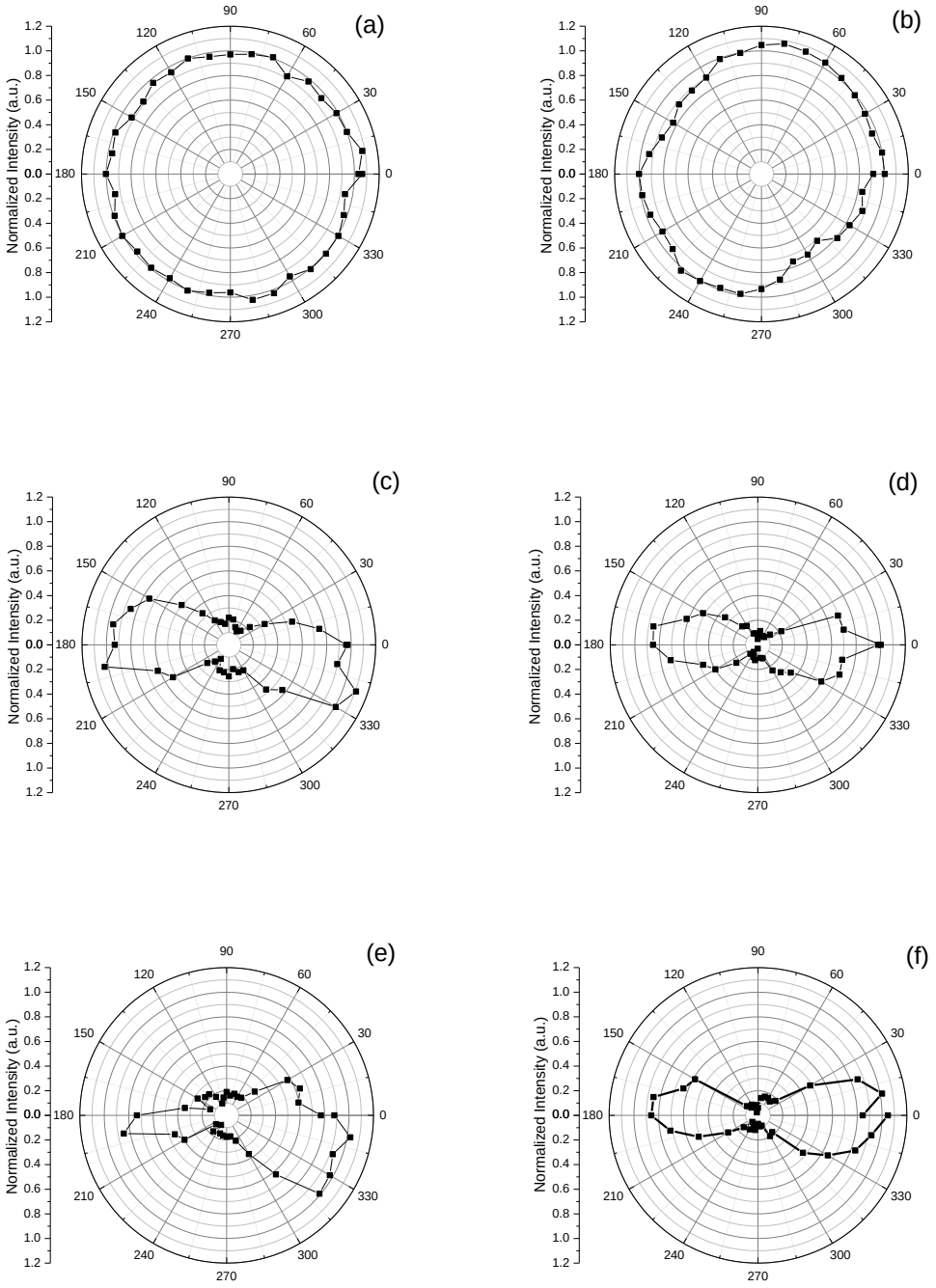

Figure 5.2. Polar plots showing the intensity of the 1095 cm^{-1} Raman band as a function of rotation angle under VV configuration. (a) PAN/CNC-20 film, (b) PAN/CNC-40 film, (c) PAN/CNC-20 fiber with 4x draw ratio, (d) PAN/CNC-20 fiber with 29x draw ratio. (e) PAN/CNC-40 fiber with 4x draw ratio, and (f) PAN/CNC-40 fiber with 29x draw ratio.

For PAN/CNC fibers, orientation dependence of the 1095 cm^{-1} Raman band intensity under VH mode was also investigated and the polar plots are shown in Figures. 5.3a to 5.3d. Unlike two-fold symmetry of 1095 cm^{-1} intensity under VV mode, under VH mode this band shows four-fold symmetry, and the intensity peaks at about 45°, 135 °, 215 ° and 315 °. For comparison, the intensity of PAN/CNC 20 wt% isotropic film under VH mode (Figure 5.3e), does not show four-fold symmetry observed in the fiber. Four-fold symmetry was also observed for the G band of isolated single wall carbon nanotubes (SWNT) [132]. In addition, highly aligned liquid crystals such as alkylcyanobiphenyl molecules also show four-fold symmetry under the VH mode in Raman spectroscopy[133]. Four fold symmetry is related to the anisotropic property of the 1D material [128]. When the CNC long-axis makes an angle of θ degrees from the laser excitation direction (V), the intensity along the CNC long-axis is $I_V \cdot \cos(\theta)$, in the VH mode, the intensity along the detection direction (H) is $I_V \cdot \cos(\theta) \cdot \cos(90° - \theta)$. So the maximum intensity in the VH mode occurs at 45°, 135°, 225°, and 270°, resulting in four-fold symmetry.

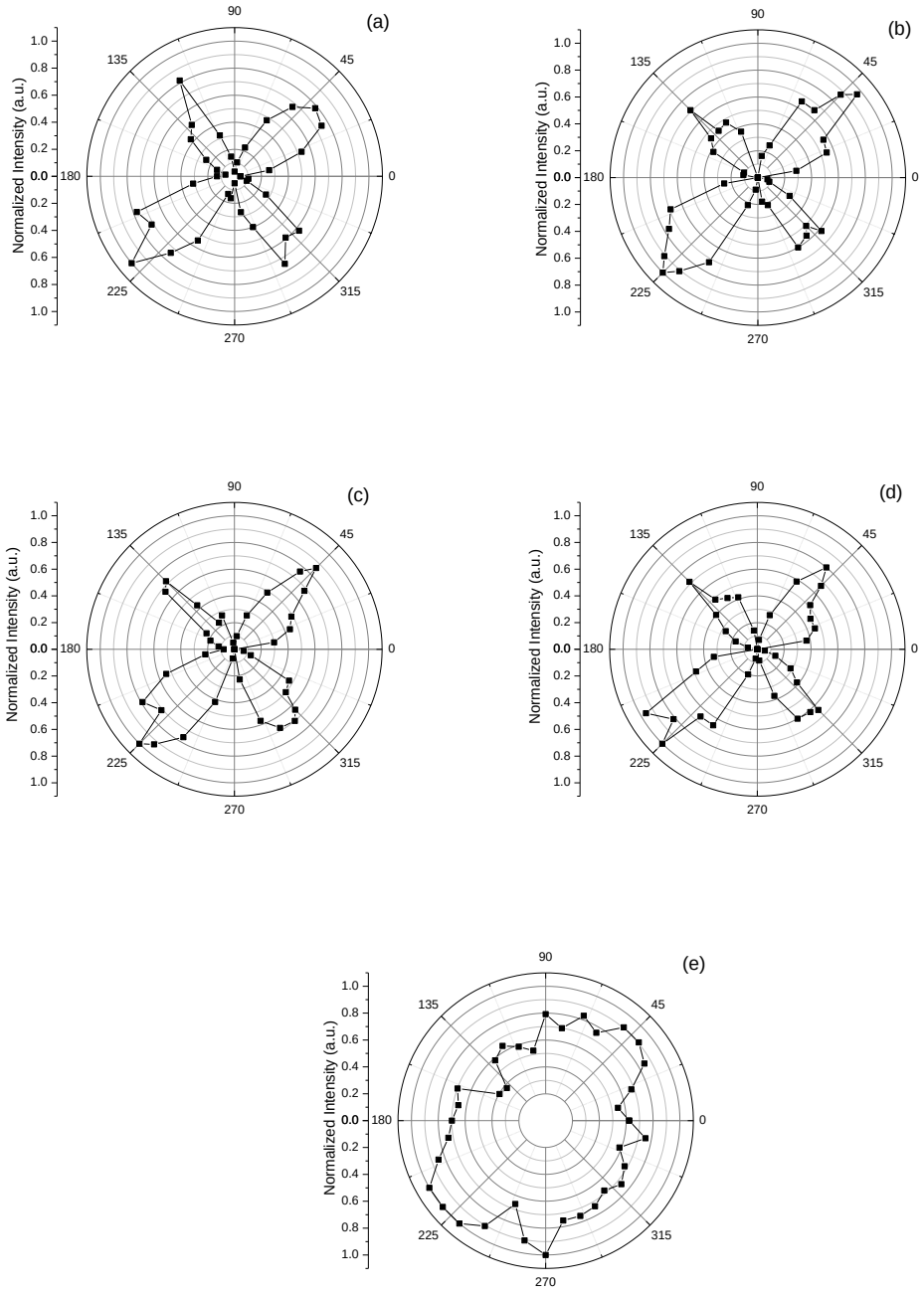

Figure 5.3. Polar plots showing the intensity of the 1095 cm^{-1} Raman band as a function of rotation angle under VH mode. (a) PAN/CNC-20 fiber with 4x draw ratio, (b) PAN/CNC-20 fiber with 29x draw ratio, (c) PAN/CNC-40 fiber with 4x draw ratio, (d) PAN/CNC-40 fiber with 29x draw ratio, and (e) PAN/CNC-20 film.

5.3.2 Stress transfer in PAN/CNC fibers

Raman spectroscopy has been used to investigate the micromechanics of deformation in different cellulosic materials including wood, regenerated cellulose fibers and composite films, and the stress-induced 1095 cm^{-1} Raman bands shift is used to monitor the deformation process[67, 69, 71]. Stress transfer was investigated in tunicate cellulose whisker/poly (vinyl acetate) nanocomposite films [69]. To date, to the best of our knowledge, this technique has not yet been used for the analysis of deformation micromechanics in CNC nanocomposite fibers.

In this study, Raman spectra of PAN/CNC fibers were obtained as a function of strain. Raman band shift of the 1095 cm^{-1} peak of PAN/CNC 20 wt% composite fiber with a draw ratio of 29 under tensile strain and under VV mode is shown in Figure 5.4. The observed peak shift has been shown to be related to the deformation of the backbone of the cellulose molecule[69]. As shown in Figure 5.5, the 1095 cm^{-1} band shifts to lower wavenumber and reaches a plateau (albeit within some experimental fluctuation). Higher Raman band shift rate indicates efficient stress-transfer between nano fillers and the polymer matrix [69, 71, 134]. It was reported that uniaxially oriented cellulose whisker showed higher Raman shift rate (-1.2 cm^{-1} $\%^{-1}$) than isotropic cellulose whiskers (-0.5 cm^{-1} $\%^{-1}$) in tunicate cellulose whisker/poly (vinyl acetate) nanocomposite films[69]. The shift rate was determined to be -2.7 cm^{-1} $\%^{-1}$ and -1.8 cm^{-1} $\%^{-1}$ for PAN/CNC 20 wt% and PAN/CNC 40 wt% fiber with 4x draw ratio. When composite fibers were stretched to 29x draw ratio, the shift rate for PAN/CNC 20 wt% and PAN/CNC 40 wt% fiber was determined to be –5.4 cm^{-1} $\%^{-1}$ and -3.5 cm^{-1} $\%^{-1}$, respectively. This is consistent with previous PAN/CNT study where drawn fibers showed a higher G′ (~2580

cm^{-1}) Raman band shift rate than as-spun fiber [134]. Based on the above analysis, stress transfer from PAN matrix to CNC is more efficient in PAN/CNC fibers at high draw ratio than that at low draw ratio.

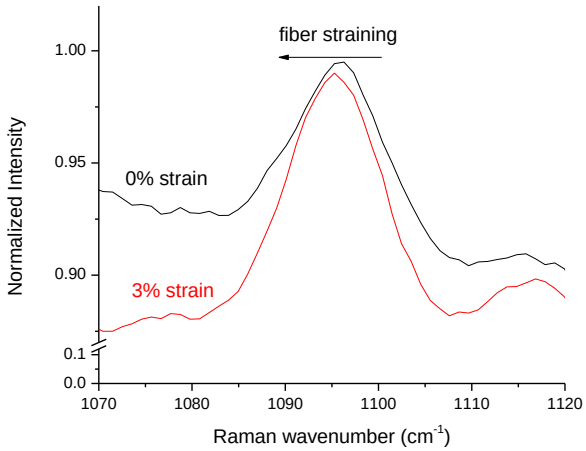

Figure 5.4. Raman band shift of 1095 cm^{-1} peak for PAN/CNC-20 composite fiber with a draw ratio of 29 under VV mode.

To quantitatively analyze the interfacial shear stress, it was calculated using the modified shear-lag equation[134]:

$$\tau_i = \frac{nE_f\,\varepsilon_i}{2}\tanh(ns) \qquad (5.3)$$

where $n = \sqrt{\frac{G_m}{E_f\ In(\frac{R}{r})}}$, E_f is the CNC modulus (150 GPa)[135], ε_i is the elongation at the PAN-CNC interface. G_m is the PAN shear modulus, which is estimated to be 1.5 GPa[134]. L is the length of CNC (153 nm) and r is the CNC radius (3.15 nm) as measured in chapter 2. s is the aspect ratio (L/2r) of CNC and the ratio R/r is defined by the geometrical spacing of the CNC, where R is the spacing between neighboring CNCs.

R values were calculated using equation 4 from ref.[116], and were found to be 15 and 10 nm for 20 and 40 wt% CNC containing fibers, respectively.

$$R = 2r\sqrt{\frac{\pi[(100-f_m)\cdot\rho + f_m\cdot\rho]}{2\sqrt{3}\cdot f_m\cdot\rho}} \qquad (5.4)$$

where r is the CNC radius. f_m is mass percentage of CNC and ρ is the density of CNC (1.6 g/cm^3). In the PAN/CNT study, the G′ Raman band shift rate of individual SWNT was used as reference to calculate the elongation at the PAN-CNT interface[134]. Since the 1095 cm^{-1} Raman band shift rate of individual CNCs has not been reported, 0.2 % iso-strain between CNC and PAN matrix was assumed for calculating the interfacial shear stress. Based on this iso-strain assumption, values of τ_i calculated from Equation 5.3 for PAN/CNC 20 and 40 wt% fibers are 16.1 and 18.4 MPa, respectively. The iso-strain model assumes the highest possible strain in the CNC, and thus the above values of 16.1 and 18.4 MPa represent the upper limits of the interfacial shear stress in the respective fibers. For comparison, we note that the values for interfacial shear stress of CNT reinforced PAN fibers determined by Raman spectroscopy was in the range of 13.1 to 44.3 MPa [134]. Interfacial shear stress determined by pullout tests using AFM tip was from ~ 32 to ~ 68 MPa for the PMMA/CNT composite and it ranged from ~ 16 to ~ 88 MPa for polyethylene-butene/CNT composite [136, 137]. In these cases, smaller diameter CNTs was reported to have higher interfacial shear strength values. A comparison of the data presented in this study for PAN/CNC system to the data on polymer/CNT systems in the literature, shows that the interfacial shear stress for PAN/CNCs is lower than in most polymer/CNTs. However, we note that this comparison is being made between the PAN/CNC system, where the CNC loading is quite high (at 20

and 40 wt% CNC) to polymer/CNT systems, where the CNT loading is relatively low (< 1 wt% CNT). Another factor that affects this behavior is the filler aspect ratio. The aspect ratio of CNC used in this study is in the range of 20 to 30, while the aspect ratio of CNT used for the interfacial study in ref. [134] was > 1000.

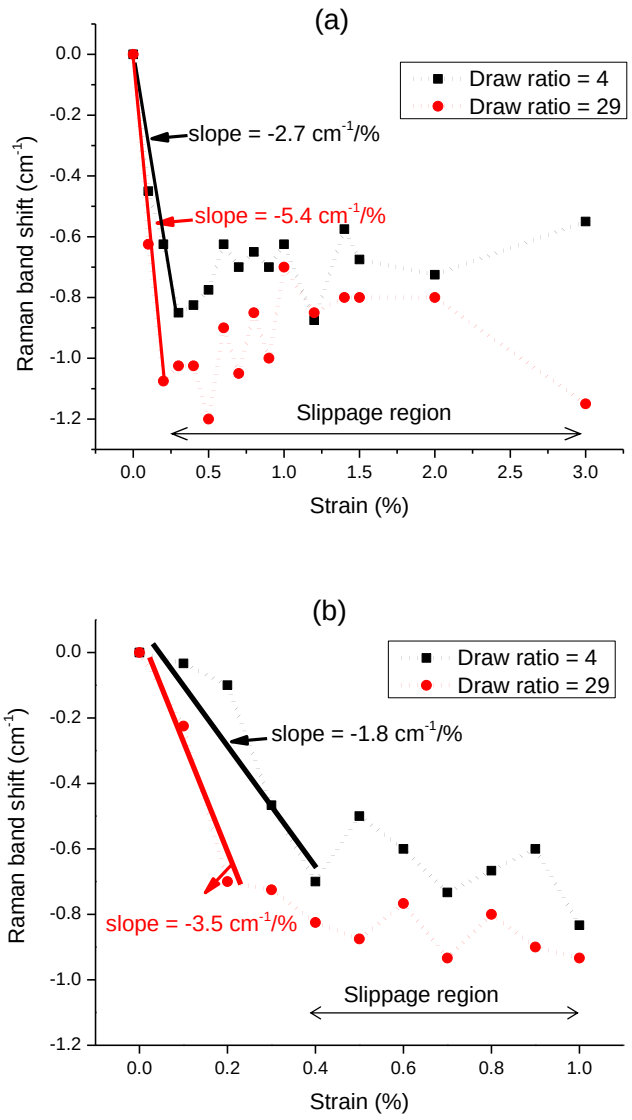

Figure 5.5. Raman band shift in 1095 cm^{-1} as a function of strain for PAN/CNC composite fibers. (a) PAN/CNC-20 fiber and (b) PAN/CNC-40 fiber.

5.4 Conclusions

Raman spectroscopy has been used to characterize CNC orientation and to study the interfacial shear stress in the PAN/CNC fibers. Polar plots of the nanocomposite fibers show four-fold symmetry under VH mode, and two-fold symmetry under VV mode, and both second and fourth order CNC orientation parameters can be obtained. Calculated interfacial shear strength in PAN/CNC-20 and PAN/CNC-40 fibers are 16.1 and 18.4 MPa, respectively.

CHAPTER 6. STABILIZATION KINETICS STUDY OF POLYACRYLONITRILE/CELLULOSE NANOCRYSTALS COMPOSITE FIBERS

6.1 Introduction

Stabilization process is a critical step to produce carbon fibers[7, 81]. In the stabilization process of PAN fibers, several reactions including cylization, oxidation and crosslinking occur. Understanding the kinetics of these stabilization reactions helps to find the optimized parameters to stabilize PAN fibers. The stabilization kinetics can be affected when incorporating other materials such as carbon nanotubes or lignin into PAN fibers [8, 138]. In this chapter, stabilization kinetics of PAN/CNC-40 fibers has been studied to understand the effect of CNC on stabilization kinetics of PAN fiber.

6.2 Experimental

Details about materials, solution preparation and fiber spinning process can be found in chapter 4. The CNC content in composite fibers is 40 wt% with respect to the weight of the PAN. The as-spun fiber spin draw ratio is 1x. Fibers with total draw ratio of 10x were used in this study. A tube furnace manufactured by Micropyretics Heaters International (Cincinnati, OH) was used for fiber stabilization. For stabilization, fibers were heated from room temperature to 265°C under 20 MPa stress in gas environment (only air, only nitrogen, or nitrogen then air) at a heating rate of 5 °C/min and hold at 265°C for different times.

Single filament tensile testing was performed on precursor and stabilized fibers using a gauge length of 25.4 mm on FAVIMAT tensile testing instrument with 1%/s strain rate. The density of stabilized PAN and PAN/CNC-40 fibers is assumed with ~1.4 g/cm^3. Fourier transform infrared spectroscopy (FTIR) spectra from 3000 to 800 cm^{-1} were collected using an infrared microscope (Spectrum one, Perkin Elmer) on PAN and PAN/CNC fibers mixed with potassium bromide (KBr). Differential scanning calorimetry (DSC, TA Instrument Q200) was performed on fibers under different gas environments and various heating rates (1, 5, 10, and 15 °C/min) to study the stabilization reaction kinetics.

6.3 Results and discussion

Mechanical properties of precursor fibers are summarized in Table 1. At a draw ratio of 10, PAN/CNC-40 composite fibers show higher tensile strength, tensile modulus, and work of rupture and a slightly lower elongation at break as compared to the control PAN precursor fibers. The mechanical properties of stabilized fibers in air are listed in Table 6.2. As compared to the precursor fibers, the tensile strength and tensile modulus of stabilized fibers in air are lower and decreases as the stabilization time increases. Representative SEM images of cross-section of stabilized fibers in air are shown in Figure B.1 (Appendix B).

WAXD patterns and integrated scans of PAN and PAN/CNC-40 precursors and the resulting stabilized fibers in air are shown in Figure 6.1. For the control PAN fiber, its characteristic peaks occur at $2\theta = 16.7$ ° corresponding to (200),(110) of PAN crystals. The intensity of this peak decreases with the increasing stabilization time, indicating

PAN undergoes a structural change during the stabilization process. For PAN/CNC-40 composite fibers, characteristic peaks of CNCs occur at 2θ = 20.5 ° and 22.6 ° corresponding to respective (102) and (200) planes of CNC crystals. After being stabilized at 265 °C for 4h, all PAN and CNC peaks disappeared completely, and only peak at 2θ = 25.7 ° exists, which is attributed to the formation of the ladder structure from PAN [7, 139]. To study the effect of CNCs on the formation of ladder structure, the orientation of the ladder structure in stabilized fibers was determined from the azimuthal WAXD scans. As shown in Figure 6.2, the azimuthal scans of stabilized PAN fibers can be fitted by one peak. For stabilized PAN/CNC-40 composite fibers, the peak of azimuthal scans is sharp, which is deconvoluted into two fitting peaks. The calculated Herman's orientation factors based on the azimuthal scans are listed in Table 6.3. According to curve fitting in composite fibers, a small amount of highly oriented (0.98-0.99) ladder structure is observed. Since stabilized cellulose does not exhibit any peak around 2θ = 25.7 ° [139], this highly oriented ladder structure should be from PAN in the vicinity of CNC. Similar result has been reported in stabilized carbon nanotubes reinforced PAN fiber [7]. Also the overall orientation of ladder structure in stabilized composite fiber shows better orientation than the control PAN fiber. This implies that the distribution of oriented CNCs in the fiber structure improves the orientation of the overall ladder structure during stabilization.

The chemical structure of precursor and stabilized fibers was also characterized by FTIR (Figure 6.3). In precursor fibers, the characteristic peak at ~ 2242 cm^{-1} is assigned to C≡N group. After stabilization in air, the peak at ~ 2242 cm^{-1} diminishes and becomes broaden. New peaks occur in the range of 1575 – 1725 cm^{-1} due to the

formation of C=C, C=N and C=O bonds, suggesting the formation of the ladder structure [140].

Table 6.1. Mechanical properties of PAN and PAN/CNC-40 composite fibers.

	PAN fiber	PAN/CNC-40 fiber
Draw ratio	10	10
Effective diameter (μm)	20.1 ± 0.8	19.1 ± 1.2
Linear density (dtex)	3.7 ± 0.3	3.9 ± 0.4
Density (g/cm^3)	1.18	1.34 [a]
Tensile modulus (GPa)	14.5 ± 0.9	20.7 ± 2.6
Tensile strength (MPa)	624 ± 61	812 ± 107
Strain to failure (%)	8.9 ± 0.5	8.2 ± 0.7
Work of rupture (MPa)	30.5 ± 3.6	36.9 ± 6.7

[a]Densities were calculated from the density of PAN (1.18 g/cm^3) and CNC (1.59 g/cm^3) using the rule of mixtures.

Table 6.2. Mechanical properties of fiber stabilized in air at 265°C under a tension of 20 MPa for 2, 4 and 6 hours.

	PAN fiber			PAN/CNC-40 fiber		
Holding time (h)	2	4	6	2	4	6
Tensile modulus (GPa)	12.2 ± 0.3	12.5 ± 0.3	12.2 ± 0.3	15.2 ± 0.3	12.5 ± 0.2	11.3 ± 0.2
Tensile strength (MPa)	318 ± 32	232 ± 12	244 ± 25	299 ± 14	220 ± 18	230 ± 9

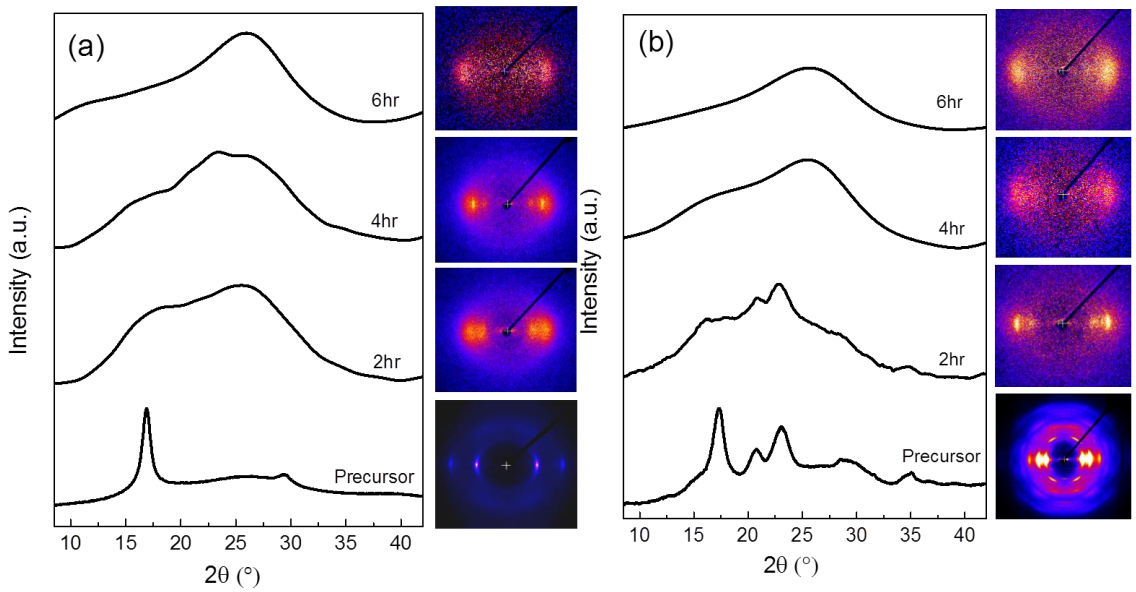

Figure 6.1. WAXD patterns and integrated scans of precursor and stabilized fibers. (a) PAN and (b) PAN/CNC-40 fibers. Fibers are stabilized in air at 265 °C under a tension of 20 MPa for 2, 4 and 6 hours.

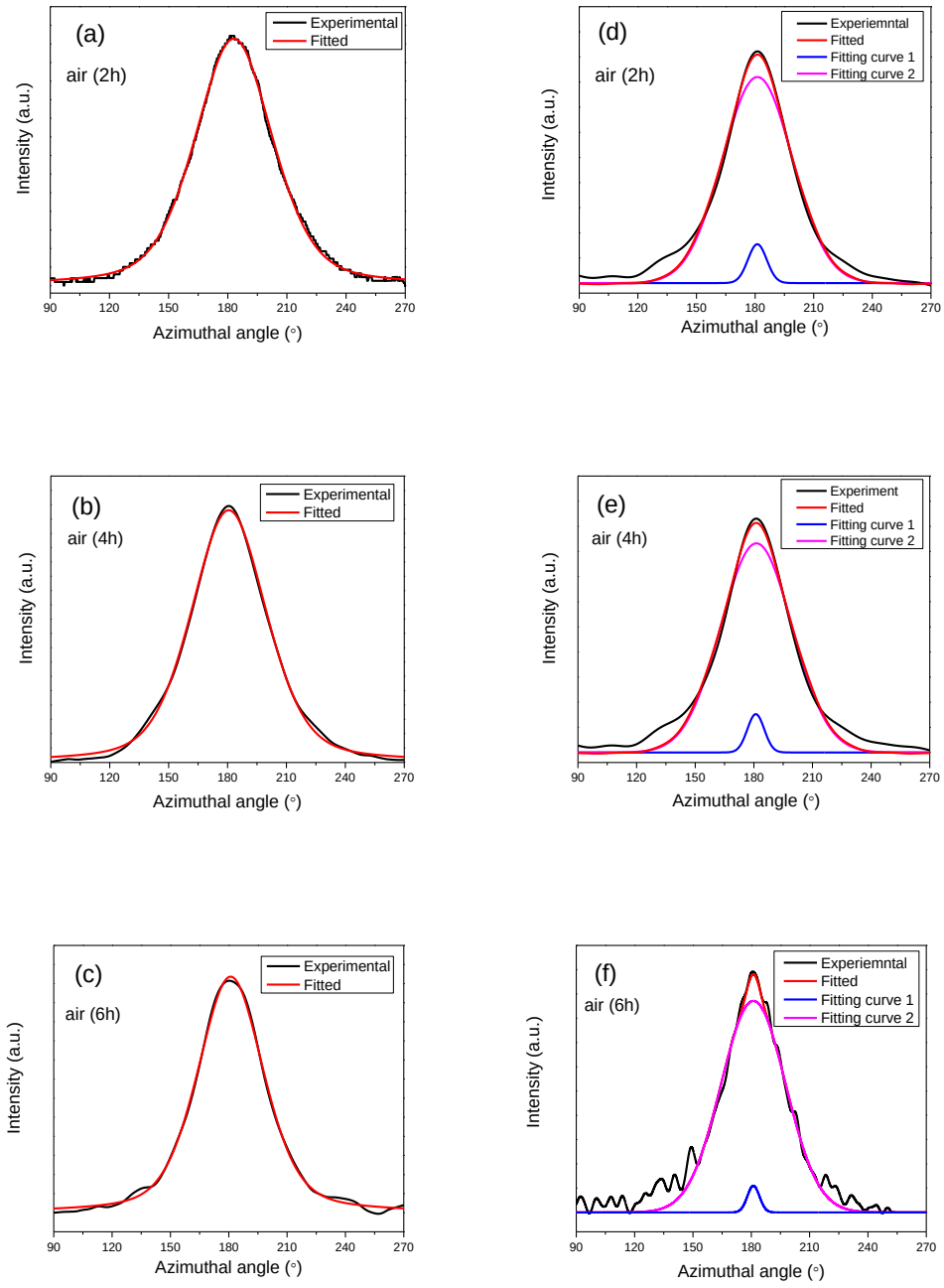

Figure 6.2. Azimuthal scans of ladder polymer at 2θ = 25.7 ° for fibers stabilized in air for 2, 4, and 6 hours at 265°C under a tension of 20 MPa. (a-c) PAN fibers, (d-f) PAN/CNC-40 fibers.

Table 6.3. Herman's orientation factor of the ladder structure in stabilized fibers (in air at 265°C under a tension of 20 MPa for 2, 4 and 6 hours).

Stabilization time (h)	Herman's orientation factor			
	PAN	PAN/CNC-40		
		Overall	Curve 1	Curve 2
2	0.64	0.76	0.98	0.75
4	0.66	0.77	0.98	0.76
6	0.69	0.79	0.99	0.78

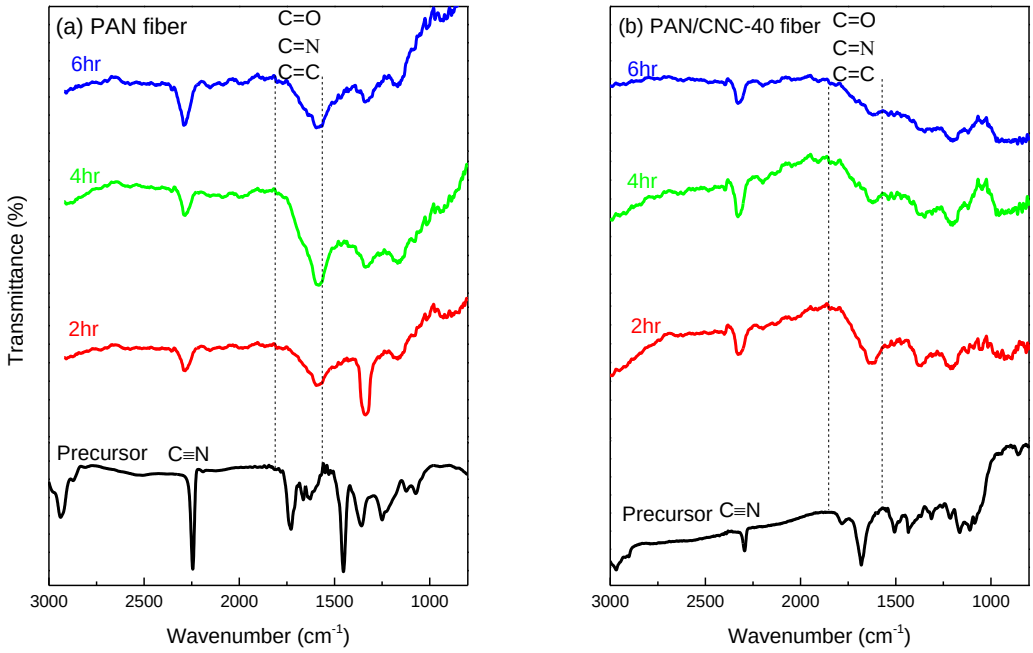

Figure 6.3. FTIR spectra of precursor fiber and stabilized fiber in air for different time. (a) PAN fiber and (b) PAN/CNC-40 fiber.

Thermal stabilization process of PAN in air is complex where cyclization, oxidation, and crosslinking occur concurrently and transform PAN chain into a thermally stable ladder polymer structure[75]. Since cyclization reaction can be initiated in air or inert environment while oxidative environment is required for oxidation and

crosslinking[141], stabilization reactions have been individually studied by: (i) heat treatment of PAN fiber in nitrogen environment, where cyclization occurs, and (ii) by re-running the samples from (i) under oxidative heat treatment to initiate oxidation and crosslinking reactions [8, 138]. To study the effect of CNCs on the stabilization process of PAN fiber, individual stabilization reaction in PAN and PAN/CNC-40 fibers were analyzed by running the fibers in different gas environments (Figure 6.4). During heat treatment under nitrogen, PAN fibers show a single exothermic peak, mainly corresponding to the cyclization reaction. For PAN/CNC-40 fibers, two exothermic peaks are observed from the heat treatment under nitrogen: one is related to PAN cyclization reaction and the subsequent one is related to CNCs reaction including the dehydration and depolymerization of cellulose [83, 84]. After re-running the fibers in air after in N_2, two broad peaks are observed, which are assigned to oxidation reaction and crosslinking reaction [8, 138].

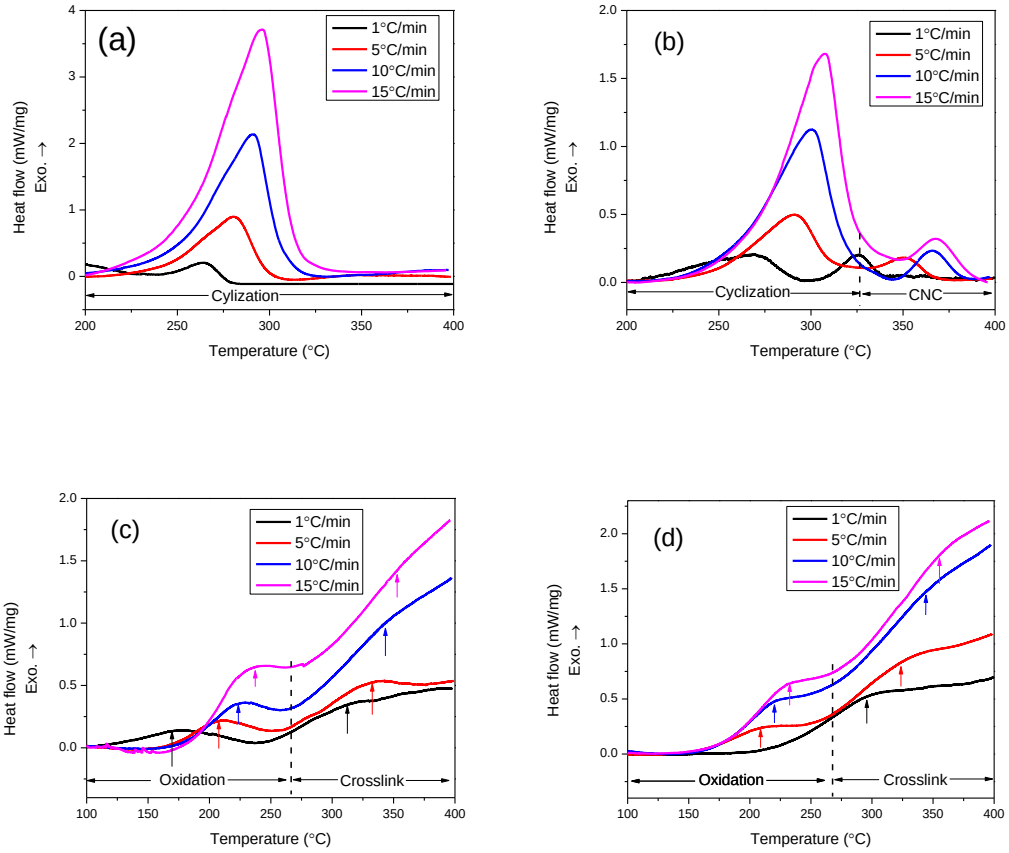

Figure 6.4. DSC curves of PAN and PAN/CNC fibers at various heating rates. (a) PAN fiber in nitrogen, (b) PAN/CNC-40 fiber in nitrogen, (c) re-running PAN fiber in air after run in nitrogen, and (d) re-running PAN/CNC-40 fiber in air after run in nitrogen.

The peak temperatures of cyclization ($T_{cyclization}$), oxidation ($T_{oxidation}$) and crosslinking ($T_{crosslink}$) obtained by DSC at different heating rates are listed in Table 6.4. The activation energy is calculated by Kissinger method given by the following equation [142]:

$$-\frac{Ea}{R} = \frac{d(Ln\frac{\varphi}{T_m^2})}{d(\frac{1}{T_m})} \qquad (6.1)$$

where E_a is the activation energy, R is the universal gas constant, φ is the applied heating rate, and T_m is peak temperature (in Kelvin). After the activation energy is obtained, the pre-exponential factor A can be obtained using the equation: $A = \frac{\varphi E_a}{RT_m^2} e^{E_a/RT_m}$. Then the reaction constant k can be calculated through the Arrhenius equation $k = Ae^{-E_a/RT_m}$ [143]. At a specific temperature, a higher value of k indicates a faster reaction rate. The Kissinger plots of fibers are shown in Figure 6.5 and the calculated results are summarized in Table 6.5. It is reported that adding carbon nanotubes(CNT) into PAN fibers can lower activation energies of oxidation and the cross-linking reactions but has little effect on the activation energy of cyclization in stabilized PAN/CNT fiber[7, 8]. Compared to the PAN fiber, adding CNC into PAN fiber decreases activation energies of cyclization and crosslinking reactions by 17.5 and 19 %, respectively. Both fibers show similar values of oxidation activation energy. The calculated pre-exponential factor (A) in Arrhenius equation for all the reactions is lower by more than one order of magnitude in PAN/CNC fiber than in PAN fiber. The reaction rate constants of cyclization and oxdiation reactions of PAN calculated at 265°C are slightly lower in PAN/CNC-40 composite fiber than in PAN fibers. But composite fibers show slightly higher reaction rate constant of crosslinking reaction than that of PAN fibers.

Table 6.4. Peak temperatures from DSC for PAN and PAN/CNC-40 fibers.

Heating rate (°C /min)	PAN peak temperature (°C)			PAN/CNC-40 peak temperature (°C)			
	N_2	Rerun in air		N_2		Rerun in air	
	$T_{cyclization}$	$T_{oxidation}$	$T_{crosslink}$	$T_{cyclization}$	T_{CNC}	$T_{oxidation}$	$T_{crosslink}$
1	265	178	311	268	326	-	300
5	281	208	331	291	351	209	329
10	291	221	343	300	366	219	345
15	296	228	359	308	369	231	356

Table 6.5. Activation energies and kinetic parameters of PAN and PAN/CNC-40 fibers determined from Kissinger method.

	PAN fiber			PAN/CNC-40 fiber		
	Ea (KJ/mol)[a]	$A(s^{-1})$[b]	$K_{265°C}$ (s^{-1})[c]	Ea (KJ/mol)[a]	$A(s^{-1})$[b]	$K_{265°C}$ (s^{-1})[c]
CNCs in N_2	-	-	-	174.4	9.6×10^{13}	0.001
Cyclization	198.5	1.6×10^{18}	0.085	163.8	4.2×10^{14}	0.053
oxidation	83.5	2.2×10^{8}	1.76	83.1	6.7×10^{7}	0.573
crosslinking	157.7	7.1×10^{12}	0.003	127.8	2.0×10^{10}	0.008

a Reaction activation energy
b Pre-exponential factor
c Reaction rate constant calculated at 265°C

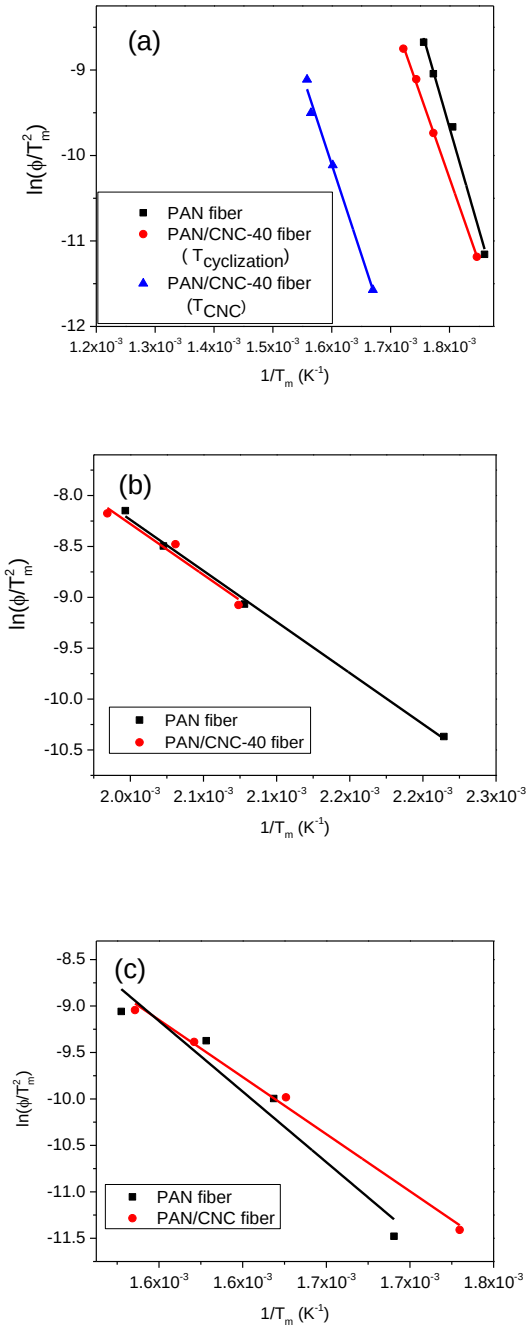

Figure 6.5. Plots of $Ln(\varphi/T_m^2)$ versus $1/T_m$ according to Kissinger method for PAN and PAN/CNC-40 fibers. (a) Cyclization and CNC reaction peaks of fibers in nitrogen, (b) oxidation peak of fibers rerun in air after running in nitrogen, and (c) crosslinking peak of fibers rerun in air after running in nitrogen.

To further study the effect of CNCs on the structural evolution of PAN, PAN and PAN/CNC-40 fibers were firstly stabilized in nitrogen for 6 hours and then further stabilized in air for various times in furnace. WAXD patterns and integrated scans of fibers stabilized in N_2 for 6 hours then in air for various times at 265 °C under a tension of 20 MPa are shown in Figure 6.6. The peak at $2\theta = 25.7$ ° is characteristic of ladder structure. In N_2 environment, sharp peak at $2\theta = 16.7$ ° in PAN fiber becomes broad and no peak appears around $2\theta = 25.7$ °. It was reported that PAN under nitrogen is initiated via cyclization and mainly forms isolated aromatic ring, instead of ladder polymer under air [144]. This suggests that isolated aromatic ring structure was formed when PAN fibers were stabilized in pure N_2. After PAN fibers were subsequently stabilized in air, the peak shift from $2\theta = 16.7$ ° towards $2\theta = 25.7$ °. For PAN/CNC-40 fiber, peak at $2\theta = 16.7$ ° of PAN become weak and characteristic peaks of CNCs at $2\theta = 20.5$ ° and 22.6 ° still exist even after fibers were stabilized in N_2 at 265 °C for 6 hours. With increasing stabilization time in air, these CNC peak intensity begins weakening and the peak position shifts to $2\theta = 25.7$ °. The orientation of the ladder structure was determined from the azimuthal WAXD scans (Figure 6.7 and Table 6.6). Compared to stabilized fiber in air, the azimuthal scans of all stabilized fiber (stabilized in N_2, then in air) are fitted by one curve. The orientation of ladder structure in PAN/CNC-40 composite fibers is about 0.69 - 0.7, which is lower as compared to 0.76 - 0.79 for stabilized composite fibers in air. But it is still slightly higher than that of the stabilized PAN fibers. When PAN fibers are stabilized in N_2 for 6 hours and then in air for 1 hour, the orientation of ladder structure is 0.65 and it approaches to 0.7 with increasing stabilization time in air.

The chemical structure of stabilized fibers in N_2 and stabilized fibers in N_2 then in air was characterized by FTIR (Figure 6.8). As compared to the precursor fibers, the peak intensity of C≡N group at ~ 2242 cm^{-1} in stabilized fibers in N_2 weakens and new peaks occur in the range of 1575 – 1725 cm^{-1} due to the formation of C=O, C═C or C═N bonds [140]. This is attributed to the formation of isolated aromatic ring structure from PAN in N_2 [144]. After fibers were stabilized in air after in N_2, all the stabilized fiber exhibit similar FTIR spectra when fiber were stabilized only in air. Combination of FTIR data and integrated scans of WAXD patterns, it suggests that isolated aromatic ring structure forms when fibers stabilized in N_2, and crosslinking and ladder structures could form when fibers are then stabilized in air after stabilized in N_2.

Mechanical properties of fiber stabilized in N_2 at 265°C under a tension of 20 MPa for 6 hours is listed in Table 6.7. Interestingly, the tensile modulus of stabilized PAN/CNC-40 fiber in N_2 for 6h is still comparable to that of the PAN/CNC-40 precursor fiber though the tensile strength significantly decreases. When both fibers were stabilized in N_2 for 6h and then in air for 1h, the tensile strength of both fibers increases as compare to that of the fibers stabilized in N_2 for 6h. This is possibly attributed to the different structures when fibers are stabilized in different gas environments. It has been shown that isolated aromatic ring are formed in pure N_2 [144], and crosslinking and ladder structures would form when fibers are subsequently stabilized in air after N_2. After these fibers are subsequently stabilized in air for more than 2 hours, all fibers show comparable mechanical properties. Representative SEM images of cross-section of stabilized fibers are shown in Figure B.2 (Appendix B).

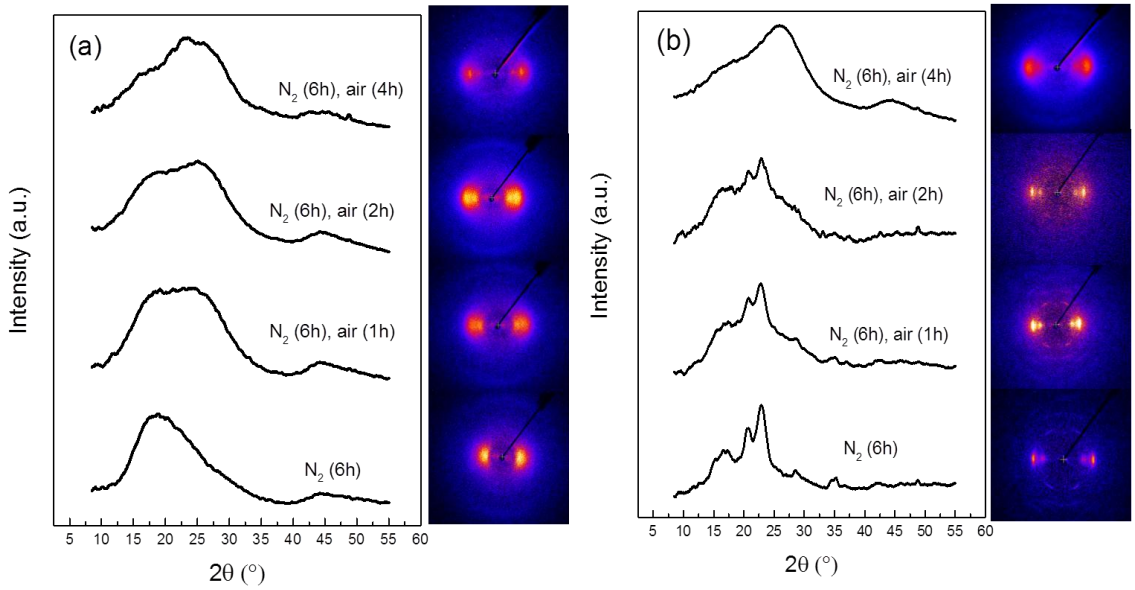

Figure 6.6. WAXD patterns and integrated scans of fibers stabilized in N_2 for 6 hours, then in air for 1, 2 and 4 hours at 265 °C under a tension of 20 MPa. (a) PAN and (b) PAN/CNC-40 fibers.

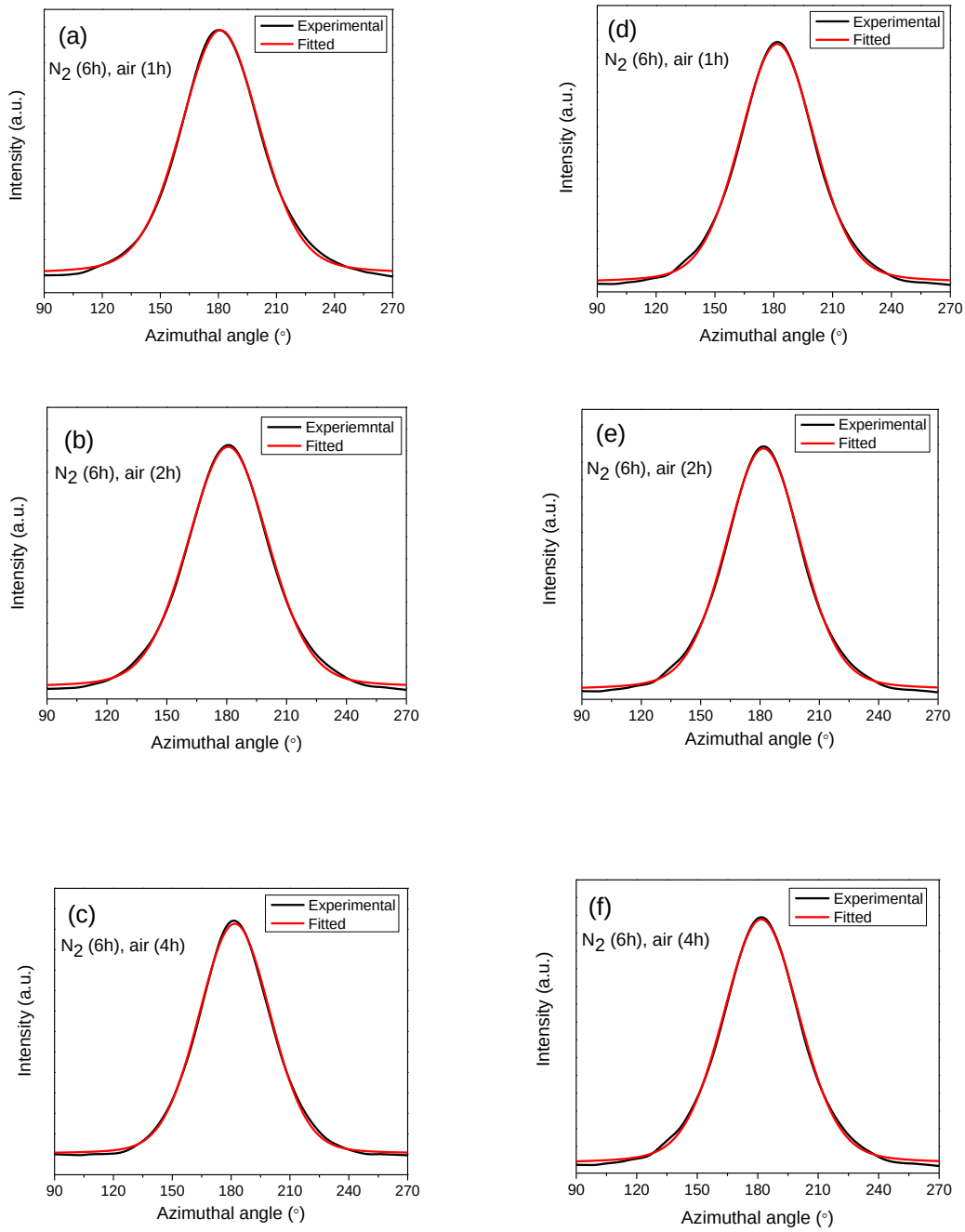

Figure 6.7. Azimuthal scans at 2θ = 25.7 ° for fibers stabilized at 265°C under a tension of 20 MPa in N_2 for 6 hours, then in air for 1, 2 and 4 hours. (a-c) PAN fibers, (e-f) PAN/CNC-40 fibers.

Table 6.6. Herman's orientation factor of ladder structure in stabilized fiber (at 265°C under a tension of 20 MPa in N_2 for 6 hours then in air for 1, 2 and 4 hours).

Stabilization time (h)	Herman's orientation factor	
	PAN	PAN/CNC-40
1	0.65	0.69
2	0.66	0.69
4	0.70	0.70

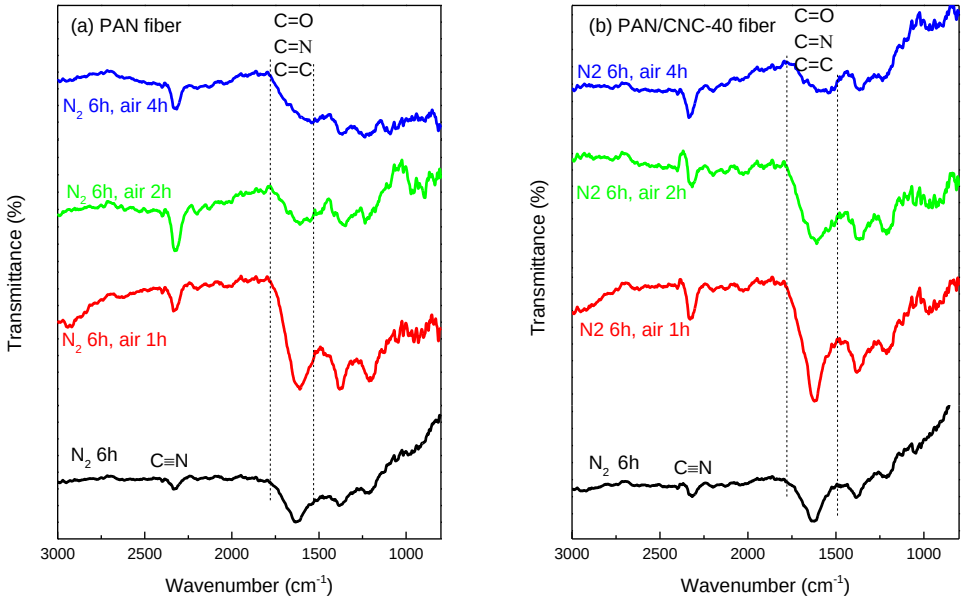

Figure 6.8. FTIR spectra of stabilized fibers in N_2 for 6 hours and stabilized fiber in N_2 for 6 hours, then in air for 2, 4, and 6 hours. (a) PAN fiber and (b) PAN/CNC-40 fiber.

Table 6.7. Mechanical properties of fiber stabilized in N_2 at 265°C under a tension of 20 MPa for 6 hours.

	PAN fiber	PAN/CNC-40 fiber
Tensile modulus (GPa)	11.4 ± 0.3	20.8 ± 0.3
Tensile strength (MPa)	155 ± 45	294 ± 33

Table 6.8. Mechanical properties of fiber stabilized in N_2 at 265°C under a tension of 20 MPa for 6 hours then in air for 1, 2 and 4 hours.

	PAN fiber			PAN/CNC-40 fiber		
Holding time in air (h)	1	2	4	1	2	4
Tensile modulus (GPa)	11.8 ±0.3	11.8 ± 0.3	11.7 ± 0.3	17.9 ± 0.2	16.3 ± 0.2	11.0 ± 0.4
Tensile strength (MPa)	258 ± 22	251 ±12	213 ± 5	324 ± 9	306 ± 7	194 ± 29

6.4 Conclusions

As compared to PAN fibers, the addition of CNCs improves the orientation of the ladder polymer when stabilized PAN/CNC-40 fibers either in air or in N_2 followed by in air. Using DSC, it shows that adding CNCs into PAN fibers has little effect on the activation energy of oxidation reaction. While the activation energies of cyclization and crosslinking reactions is reduced by 17.5 and 19 %, respectively.

CHAPTER 7. STABILIZATION AND CARBONIZATION OF POLYACRYLONITRILE/CELLULOSE NANOCRYSTALS COMPOSITE FIBERS

7.1 Introduction

In previous chapters, it has been shown that even with 40 wt% CNC concentration, good dispersion and high orientation of CNCs in PAN fiber can be achieved. These PAN/CNC fibers show good mechanical properties. Because quality of precursor fibers is critical to make high performance carbon fibers, these PAN/CNC fibers can potentially be converted to a new grade of carbon fibers. In this chapter, the effect of CNCs on the stabilized and carbonized PAN will be studied.

7.2 Experimental

7.2.1 Materials and fiber processing

Materials and the preparation of solutions and fiber spinning conditions are described in chapter 4. For carbon fiber processing, a tube furnace manufactured by Micropyretics Heaters International (Cincinnati, OH) was used. For stabilization, all fibers were heated from room temperature to 265 °C and held at 265 °C for 170 minutes, then heated to 305 °C and held for 10 minutes. During carbonization process in nitrogen, all fibers were heated up to 1400 °C at a heating of 5 °C/min and then held for 10 minutes. A total of 30 MPa stress was applied on all fiber bundles during stabilization

and carbonization processes. All precursor fibers at a draw ratio of 23 are used for stabilization and carbonization studies reported in this chapter.

7.2.2 Characterization

Single filament tensile testing was done at a gauge length of 25.4 mm on FAVIMAT tensile testing instrument (Textechno. Herbert Stein GmbH & Co. KG). The strain rates for precursors and carbon fibers during mechanical testing were 1%/s and 0.1%/s, respectively. Tensile modulus values have not been corrected for compliance. Thermogravimetric analysis (TGA, TA Instrument Q500) was used to study the fiber at a heating rate of 5 °C/min from 35 to 400 °C in air. Differential scanning calorimetry (TA Instrument Q200) was performed on fibers at different heating rate from 35 to 400 °C. Thermo-mechanical analyzer (TMA Q400, TA Instruments) was used to study the thermal shrinkage behavior of fibers under 25 MPa stress and the stress-temperature evolution of fibers under iso-strain mode with 0.3% pre-strain. Scanning electron microscopy (SEM) was performed on cross-section of carbon fibers using a Zeiss Ultra-60 SEM operated at 5 kV.

7.3 Results and discussion

The effect of draw ratio on the thermal stabilization process of PAN fibers was first investigated by TGA and the curves of PAN and PAN/CNC-10 fibers at a draw ratio of 4x and 23x are shown in Figures 7.1 (a) and 7.1 (b). The TGA curves of the PAN and PAN/CNC-10 fibers at various draw ratios are shown in Figure C.1 (Appendix C). PAN fibers with 4x draw ratio exhibit higher weight loss than fibers with 23x draw ratio. This is because the drawing process can significantly increase the PAN crystallinity and PAN

crystal size from 4x to 23x as discussed in chapter 4. For PAN/CNC-10 fibers, when temperature is less than 250 °C, composite fibers with 23x draw ratio show slightly lower weight loss than fibers at a draw ratio of 4. Interestingly, when temperatures is higher than 250 °C, PAN/CNC-10 fibers with 23x draw ratio show higher weight loss than 4x draw ratio fibers. Besides the effect of draw ratios, the effect of CNCs concentration on the thermal stability of fibers at a draw ratio of 23 is investigated (Figure 7.1(c)). When the CNCs concentration is ≦ 5 wt%, the PAN/CNC composite fibers show slightly lower weight loss than the control PAN fibers. But, for the 40 wt% CNC loaded composite fibers, it shows significantly higher weight loss as compared to PAN fibers.

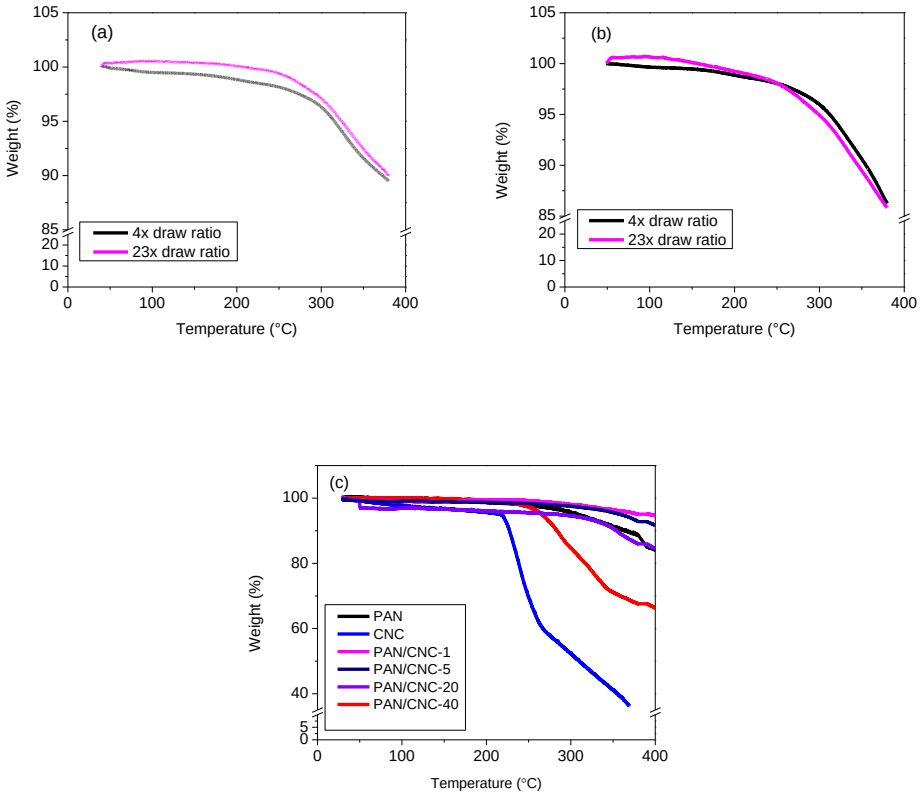

Figure 7.1. TGA curve of fibers in air. (a) PAN fiber at different draw ratios, (b) PAN/CNC-10 fiber at different draw ratios, and (c) fibers with different CNC concentrations at a draw ratio of 23.

In addition to TGA, the thermal stabilization process of fibers in air was investigated by DSC. DSC curves of PAN and PAN/CNC-40 fibers with various heating rates in air are shown in Figure C.2 (Appendix C). DSC curve of PAN fibers at a heating rate of 20 °C/min is shown in Figure 7.2 (a). Two peaks are observed in PAN fibers. For the PAN/CNC-40 composite fibers (Figure 7.2 (b)), one extra peak is observed at higher temperature, which is related to the CNCs reactions. Even though the individual stabilization events such as cyclization, oxidation, and crosslinking can be separated by controlling the gas environment as discussed in chapter 6, these reactions occur nearly simultaneously in air. The effect of adding CNCs into PAN fibers on the reaction activation energy in air was studied by running the fibers in DSC at different heating rates and peak temperatures are listed in Table 7.1. The activation energy is calculated by fitting the data using Kissinger method (equation 6.1). The calculated activation energies are listed in Table 7.2. As compared to PAN fiber, the activation energy of peak 1 is higher while activation energy of peak 2 is lower in PAN/CNC-40 composite fiber. The activation energy of peak 3 shows a higher value than that of peak 1 and peak 2.

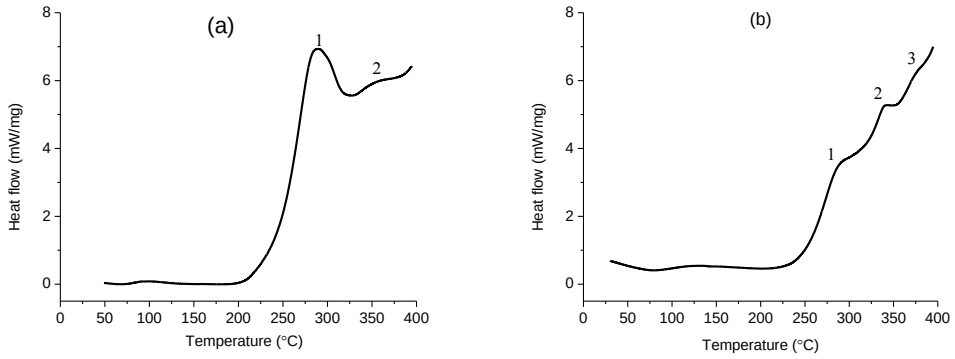

Figure 7.2. DSC curves of (a) PAN and (b) PAN/CNC-40 fibers with 23x draw ratio in air at a heating rate of 20 °C/min.

Table 7.1. Peak temperature from DSC in air for PAN and PAN/CNC-40 fibers at a draw ratio of 23.

Heating rate	PAN peak temperature (°C)		PAN/CNC-40 peak temperature (°C)		
(°C /min)	Peak 1	Peak 2	Peak 1	Peak 2	Peak 3
5	259	324	-	-	-
10	273	337	273	321	361
15	281	347	280	331	369
20	286	355	285	339	375

Table 7.2. Activation energies (E_a, KJ/mol) of fiber at a draw ratio of 23 in air determined from Kissinger method.

	PAN fiber	PAN/CNC-40 fiber
Peak 1	104	128
Peak 2	122	96
Peak 3	-	154

The thermal shrinkage behavior of PAN and PAN/CNC-40 fibers with 23x draw ratio was measured by thermo mechanical analyzer (TMA) under a tension of 25 MPa in air at a heating rate of 5 °C/min from 30 to 200 °C (Figure 7.3 (a)). As compared to the control PAN fiber, in which only crystalline PAN regions constrain the free relaxation of amorphous chains, high crystalline CNCs in composite fibers impose additional constraint on the amorphous PAN molecules. Thus the PAN/CNC composite fibers show less thermal shrinkage than the control PAN fibers. Moreover, the higher the CNCs loading, the less thermal shrinkage is observed. In addition, the stress-temperature evolution of fiber was monitored by a heating-cooling cycle under a constant iso-strain

with TMA. All fibers were heated to 175 °C at a heating rate of 5 °C/min and then cooled down to 50 °C and the heating-cooling cycles were repeated for 3 times (Figure 7.3 (b)). During the first heating cycle, stress development from thermal shrinkage is observed starting above 70 °C due to the entropic relaxation of polymer chains. The maximum entropic stress in PAN fiber during first thermal cycling is higher than in PAN/CNC-40 fiber. During the second and third thermal cycles, stress was mainly attributed to intrinsic thermal expansion/shrinkage below PAN glass transition temperature while stress was resulted from entropic stress above PAN glass transition temperature [7]. In the second and the third cycles, the magnitude of shrinkage stress of PAN and PAN/CNC-40 fibers decreases as compared to that of fibers in the first thermal scan. The decrease in stress is that the polymer chains re-coil during cooling in the first cycle and do not recover during the following heating-cooling cycle [7]. In the second and third cycles, when the temperature is in the range of 50 – 95°C during heating process, the amplitude of intrinsic thermal shrinkage stress of composite fibers is comparable to that of PAN fibers (~ 3 MPa). When the temperature is in the range of 95 – 175°C during heating process, the amplitude of entropic stress in composite fibers (8 MPa) is smaller than that in the PAN fibers (13 MPa). This result implies that CNC incorporation in the PAN/CNC component constrains the entropic force from the stretched polymer chains, which is attributed to the higher crystallinity of rod-like CNCs as compared to PAN.

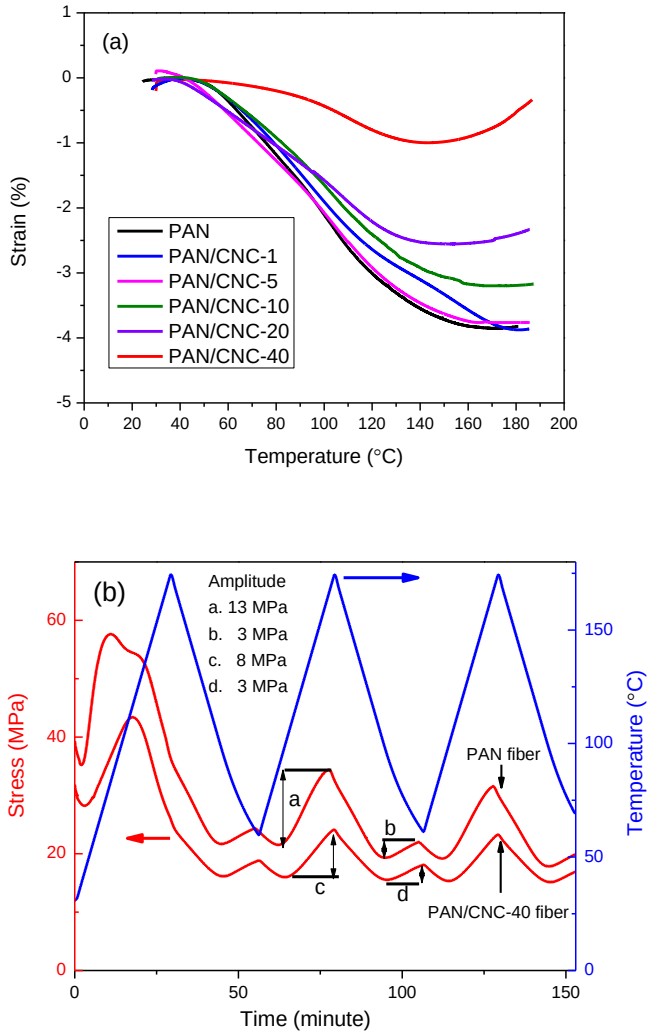

Figure 7.3. TMA curves of PAN and PAN/CNC-40 fibers at a draw ratio of 23 in air. (a) shrinkage behavior under 25 MPa stress and (b) stress changes in fibers under 0.3 % iso-strain.

Mechanical properties of carbonized fibers (PAN and PAN/CNC-40) at 1000, 1100 and 1200°C are listed in Table 7.3. As expected, all carbon fibers show improvements in tensile modulus with increasing carbonization temperatures. When carbonized at 1000 °C, tensile strength and tensile modulus of PAN based carbon fiber are 1.9 GPa and 203 GPa, respectively. When carbonized at 1200 °C, tensile strength and

tensile modulus of the PAN fiber are increased to 2.2 and 220 GPa, respectively. For PAN/CNC-40 based carbon fibers, tensile strength is about 1.7 GPa while tensile modulus increased from 189 to 205 GPa as carbonization temperature increased from 1000 to 1200°C. The elongation at break of all carbon fibers ranges from 0.6 to 1 %.

Table 7.3. Tensile properties of PAN and PAN/CNC-40 based carbon fibers.

	PAN			PAN/CNC-40		
Carbonization Temperature	1000 °C	1100 °C	1200 °C	1000 °C	1100 °C	1200 °C
Diameter (μm)	8.2 ± 0.7	7.6 ± 0.5	8.1 ± 0.4	7.0 ± 0.3	6.9 ± 0.2	7.0 ± 0.3
Modulus (GPa)	203 ± 16	220 ± 5	226 ± 8	189 ± 12	190 ± 5	205 ± 4
Strength (GPa)	1.9 ± 0.5	2.0 ± 0.4	2.2 ± 0.3	1.7 ± 0.2	1.8 ± 0.2	1.7 ± 0.2
elongation at break (%)	0.7 ± 0.2	0.6 ± 0.1	1.0 ± 0.1	0.9 ± 0.1	1.0 ± 0.1	0.7 ± 0.1

Because higher carbonization temperature can result in higher mechanical properties, fibers were carbonization at 1300 and 1400^{o}C. The mechanical properties of carbonized fibers at 1300 and 1400^{o}C are listed in Table 7.4. As carbonization temperature increases to 1400°C, as compared to fibers carbonized at lower temperature, PAN based carbon fibers show slightly decreased tensile strength while PAN/CNC-40 based carbon fibers show similar tensile strength. For tensile modulus, both fibers show higher values at higher carbonization temperature than at lower carbonization temperature. To study the effect of CNCs concentration on the carbon fiber properties, PAN/CNC-10 and PAN/CNC-20 fibers are carbonized at 1300 and 1400°C. As shown in

Table 7.4, at 1400°C carbonization temperature, both PAN/CNC-10 and PAN/CNC-20 based carbon fibers show higher tensile strength (2.3 GPa) than PAN based carbon fiber (1.6 GPa), and they show comparable tensile modulus (265 GPa for PAN/CNC-10 based carbon fiber, and 252 GPa for PAN/CNC-20 based carbon fiber) as compared to PAN based carbon fiber (257 GPa).

Table 7.4. Tensile properties of various carbon fibers.

	PAN[a]		PAN/CNC-10[a]		PAN/CNC-20[a]		PAN/CNC-40[a]	
Carbonization Temperature	1300°C	1400°C	1300 °C	1400°C	1300 °C	1400 °C	1300 °C	1400 °C
Diameter (μm)	7.7±0.4	8.1 ± 0.3	7.4 ± 0.4	7.5 ± 0.3	6.2 ± 0.1	6.0 ± 0.4	7.3 ± 0.3	7.1 ± 0.3
Modulus (GPa)	251 ± 27	257 ± 8	251 ± 10	265 ± 11	246 ± 12	252 ± 9	226 ± 18	220 ± 7
Strength (GPa)	1.9 ± 0.4	1.6 ± 0.4	1.8 ± 0.3	2.3 ± 0.4	2.3 ± 0.5	2.3 ± 0.5	1.8 ± 0.4	1.9 ± 0.4
elongation at break (%)	0.7 ± 0.1	0.6 ± 0.1	0.7 ± 0.1	0.8 ± 0.1	0.9 ± 0.2	0.9 ± 0.2	0.7 ± 0.1	0.9 ± 0.2

[a] Precursor fiber at a draw ratio of 23.

To study the effect of CNCs on the structure of PAN based carbon fibers, all the carbonized fibers are characterized by Raman spectroscopy. The Raman spectra of carbon materials usually exhibit a disorder band (D-band at ~ 1350 cm^{-1}) and graphitic band (G-band at ~ 1580 cm^{-1}). For precursor fibers, the PAN fibers do not exhibit any peak while the PAN/CNC-40 fibers show a peak at around 1095 cm^{-1} due to the C-O stretch in cellulose. After stabilization, only D and G-bands are observed in the Raman spectra (Figure 7.4) in both fibers. In the carbonized fibers, the G-band becomes more

obvious as compared to the stabilized fibers, suggesting more formation of the ordered graphitic structure. The Raman spectra of fibers carbonized at 1300°C are shown in Figure 7.5. The I_D/I_G peak intensity ratio of various carbon fibers is listed in Table 7.5. I_D/I_G ratio of the PAN based carbon fibers decreases from 2.75 to 2.52, as carbonization temperature increases from 1000 to 1300°C. At 1300°C, I_D/I_G values of all composite based carbon fibers are about 2.28 - 2.3.

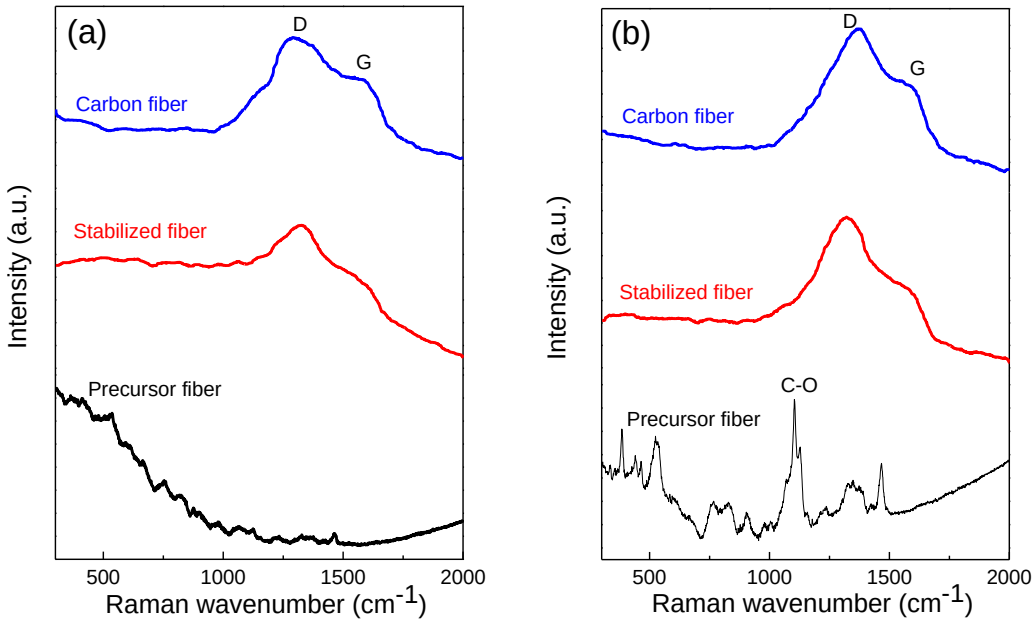

Figure 7.4. Raman spectra of (a) PAN and (b) PAN/CNC-40 precursor, stabilized and carbonized fibers at 1000°C.

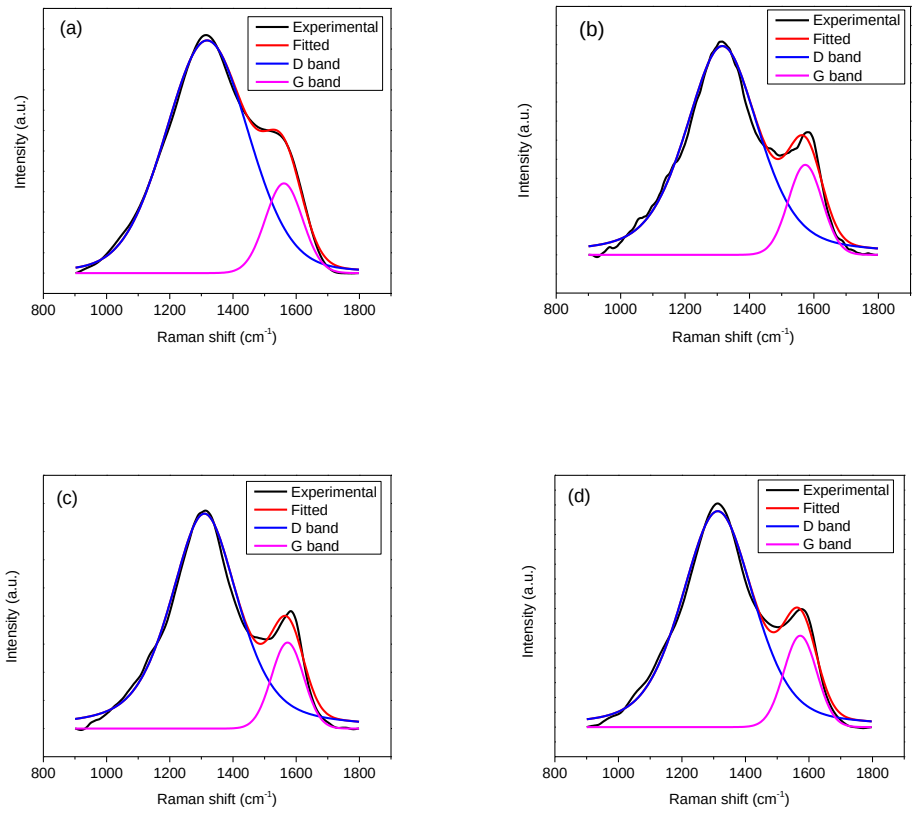

Figure 7.5. Raman spectra and fitting curves of PAN and PAN/CNC fibers at a draw ratio of 23 carbonized at 1300 °C. (a) PAN, (b) PAN/CNC-10, (c) PAN/CNC-20, (D) PAN/CNC-40.

Table 7.5. I_D/I_G ratio of carbonized fibers.

	PAN	PAN/CNC-10	PAN/CNC-20	PAN/CNC-40
1000 °C	2.75	-	-	2.55
1300 °C	2.52	2.30	2.28	2.31

Integrated WAXD scans of precursor, stabilized, and carbon fibers are shown in Figure 7.6. As compared to precursor and stabilized fibers, carbonized fibers show two distinct peaks at $2\theta \approx 26°$ and $2\theta \approx 43°$, which are (002) and (100) (101) planes of carbon structure, respectively. Structural parameters of various carbon fibers are listed in Table

7.6. For PAN and PAN/CNC-40 based carbon fibers, when carbonization temperature increased from 1000 to 1300°C, larger crystal sizes ($L_{2\theta \approx 26^\circ}$ and $L_{2\theta \approx 43^\circ}$) and higher plane orientation (f_{002}) are observed. At 1300°C carbonization temperature, carbonized PAN/CNC fibers show a relatively larger crystallize size of (10) plane (2.63 – 3.24 nm) as compared to the carbonized PAN fiber (1.98 nm).

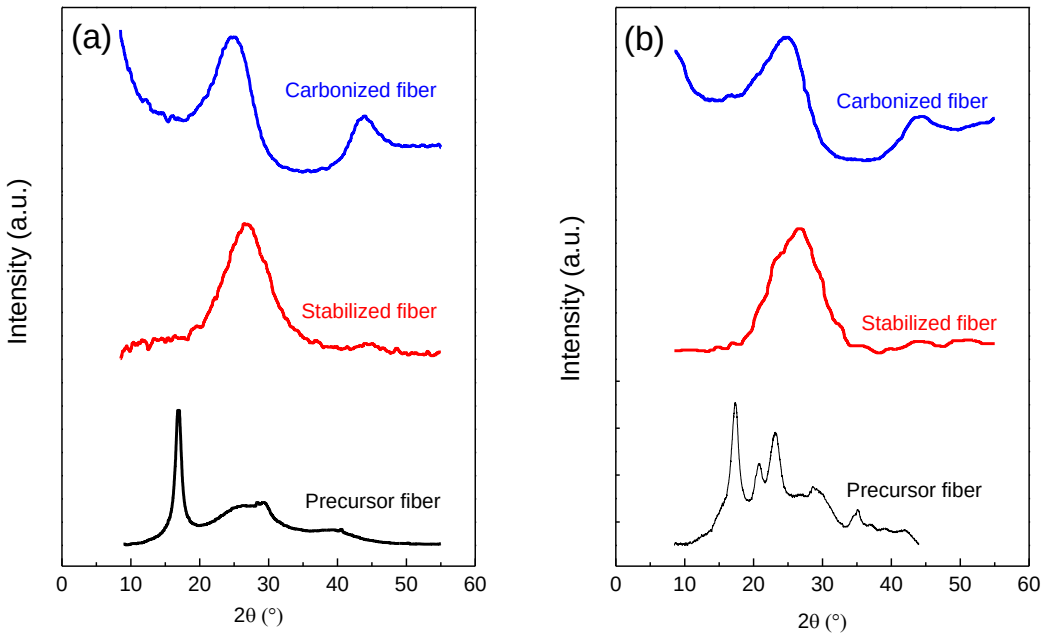

Figure 7.6. Integrated WAXD scans of precursors, stabilized, and carbonized fibers (at 1000°C) for (a) PAN and (b) PAN/CNC-40.

Table 7.6. Structural parameters of carbonized PAN and PAN/CNC fibers

	PAN		PAN/CNC-10	PAN/CNC-20	PAN/CNC-40	
Carbonization Temperature	1000°C	1300°C	1300 °C	1300 °C	1000 °C	1300 °C
$d_{(002)}$ [a] (nm)	0.346	0.356	0.340	0.342	0.355	0.347
$L_{(002)}$ [b] (nm)	1.14	1.36	1.54	1.37	1.15	1.44
$L_{(10)}$ [c] (nm)	1.32	1.98	2.98	3.24	1.94	2.63
f_{002} [d]	0.73	0.75	0.77	0.77	0.74	0.79
Z_{002} [e] (deg)	35.4	33.4	30.8	29.5	33.8	27.2

[a] $d_{(002)}$: *d*-spacing of (002) plane at $2\theta \sim 26°$.
[b] Crystal size of (002) plane at $2\theta \sim 26°$, according to Scherrer's equation with $K = 0.9$
[c] Crystal size of (10) plane at $2\theta \sim 43°$, according to Scherrer's equation with $K = 0.9$
[d] orientation factor of (002) plane
[e] Full-width at half-maximum (FWHM) from azimuthal scans of (002) plane at $2\theta \sim 26°$.

SEM images of carbon fibers' cross sections are shown in Figure 7.7. Carbon fibers made from PAN, PANCNC-10 and PAN/CNC-20 fibers show solid cross sections while the PAN/CNC-40 based carbon fibers exhibit certain amount of observable voids, whose diameters are about 50 - 100 nm. Micron sized voids that were elongated along the fiber axis were reported in PAN/lignin carbon fibers, especially when lignin concentration is greater than 15 wt% [145, 146]. These voids were attributed to low solution viscosities and different stabilization process for PAN/lignin fibers as compared to PAN fibers [95, 145]. The formation of voids in PAN/CNC based carbon fibers may be from two possible factors. One is the low carbon yield of cellulose (~30 wt%) as compared to PAN ~ 50 wt%) [56]. During stabilization and carbonization, CNCs are converted to carbon in situ. Due to its low carbon yield, voids may form. The other factor is that different stabilization reactions process take place in PAN and CNCs. Some PAN

or CNCs may not be fully stabilized under the same stabilization conditions. These not fully stabilized polymers may burn off during carbonization and thus form voids. In the future, stabilization parameters of PAN/CNC composite fibers containing different CNCs concentration should be optimized to find a balance to fully stabilized PAN as well as CNC.

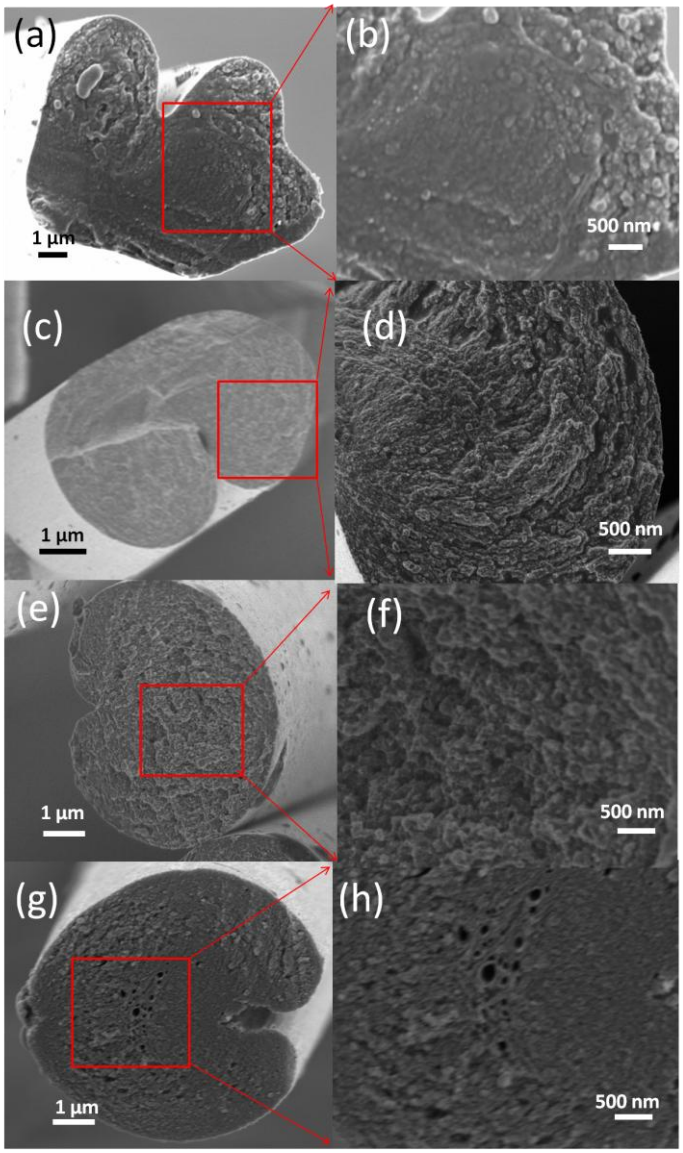

Figure 7.7. SEM images of cross sections of carbonized fibers at 1300 °C. (a-b) PAN, (c-d) PAN/CNC-10, (e-f) PAN/CNC-20, and (g-h) PAN/CNC-40 based carbon fibers.

7.4 Conclusions

Carbon fibers were made from polyacrylonitrile (PAN) fibers containing 10, 20 and 40 wt% CNC. Based on Raman spectroscopy, PAN/CNC based carbon fibers show lower I_D/I_G ratio than PAN based carbon fibers. Azimuthal scans of WAXD show that higher carbonization temperature results in larger crystal size and higher orientation of carbon structure. Carbonized PAN/CNC-10 and PAN/CNC-20 fibers show comparable tensile strength and tensile modulus to the PAN based carbon fiber. However, PAN/CNC-40 based carbon fibers show relatively lower tensile modulus where voids were observed in the cross section.

CHAPTER 8. CONCLUSIONS AND RECOMMENDATIONS

8.1 Conclusions

Individually dispersed CNCs in solvents including pure DMF, pure water, and mixture of H_2O/DMF have been successfully prepared. The critical moisture (≧3.8 wt %) in CNC is required to disperse individual CNCs. Compared with pure solvents such as DMF and H_2O, H_2O/DMF co-solvent mixture can more effectively disperse individual CNC.

The PAN solution rheological properties are affected with the incorporation of CNCs. With the presence of CNC, solution behavior changes from newtonian fluid to shear-thinning fluid at lower angular frequency. PAN/CNC composite fibers were successfully spun by gel spinning method. The CNC reinforcement efficiency is more pronounced in fibers at low draw ratios. At a draw ratio of 4x, the tensile modulus increased from 8.7 GPa for the control PAN to 18.8 GPa for PAN/CNC-40 composite fiber. The drawing process increases PAN crystal size, PAN crystallinity and PAN crystallite orientation in all fibers, resulting in improved tensile strength and tensile modulus. Like other nanocomposite fibers, the drawing process decreases the elongation at break of PAN/CNC fibers when CNC loading is up to 20 wt%. However, for PAN/CNC-40 composite fiber, the drawing process improves the PAN/CNC-40 composite fiber strain to failure from 1.5% for 4x draw ratio to 8.0 % for 29x draw ratio. Elongation at break of PAN/CNC-40 composite fibers at the highest draw ratio is comparable to that of the control PAN fiber also at its highest draw ratio.

Raman spectroscopy has been used to characterize CNC orientation and to study the interfacial shear stress in the PAN/CNC fibers. Polar plots of the nanocomposite fibers show four-fold symmetry under VH mode, and two-fold symmetry under VV mode, and both second and fourth order CNC orientation parameters can be obtained. Calculated interfacial shear strength in PAN/CNC-20 and PAN/CNC-40 fibers are 16.1 and 18.4 MPa, respectively.

As compared to PAN fibers, the addition of CNCs improves the orientation of the laddered polymer when stabilized PAN/CNC fibers either in air or in N_2 followed by air. Using DSC, it shows that adding CNCs into PAN fibers has little effect on the activation energy of the oxidation reaction. While the activation energies of cyclization and crosslinking reactions are reduced by 17.5 and 19 %, respectively.

Carbon fibers were made from PAN fibers containing 10, 20 and 40 wt% CNC. Under the same processing conditions, carbonized PAN/CNC-10 and PAN/CNC-20 fibers show comparable tensile strength and tensile modulus to the PAN based carbon fiber. However, PAN/CNC-40 based carbon fibers show relatively lower mechanical properties where voids were observed in the cross section.

8.2 Recommendations for future studies

1. In chapter 2, it has been shown that DMF/water co-solvent can more effectively disperse individual cellulose nanocrystals than pure DMF or pure water. In the future, different co-solvent systems such as dimethyl sulfoxide (DMSO)/H_2O and dimethyl acetamide (DMAc)/H_2O should be explored to study the dispersibility of CNCs in these co-solvents. In addition, the simulation study is recommended to understand the interaction between CNC and different solvents, especially the hydrogen bonding interaction. Combination of experimental and simulation study can potentially find a co-solvent system that can more effectively disperse individual CNCs than reported to-date. This `co-solvent system may help to disperse other nanomaterials, if they are functionalized with –OH groups on their surface.
2. In chapter 4, PAN/CNC composite fibers containing 40 wt% CNCs exhibit good ductility. The mechanism of this phenomenon needs more investigation. For example, in gel-spun CNC reinforced poly(vinyl alcohol) fibers, the strain to failure of these fibers with 40 wt% CNC concentration significantly decreases as compared to the poly(vinyl alcohol) fiber. Is the dispersion of CNCs the only factor that accounts for the ductility of PAN/CNC fibers? DMF/H_2O co-solvent can be tried in poly(vinyl alcohol) fibers to compare the results.
3. In chapters 6 and 7, azimuthal scans of WAXD show that the orientation of ladder structure is higher in the PAN/CNC composite fibers than in PAN fibers. PAN/CNC based carbon fibers show mechanical properties comparable to the PAN based carbon fibers. The microstructure of PAN, PAN in the vicinity of

CNCs and CNCs in stabilized fibers and the corresponding carbon fibers also need further investigation. This will help in understanding the effect of CNCs on the PAN structure evolution during carbonization

4. The optimized stabilization and carbonization process should be explored to make high performance PAN/CNC based carbon fibers. For example, the heating rate has the effect on the carbon yield of CNC. The stress applied on the fibers can be adjusted due to different shrinkage behavior in PAN and PAN/CNC fibers. Different stabilization holding times should be explored based on the CNC concentration.

APPENDIX A. SUPPORTING INFORMATION FOR CHAPTER 4

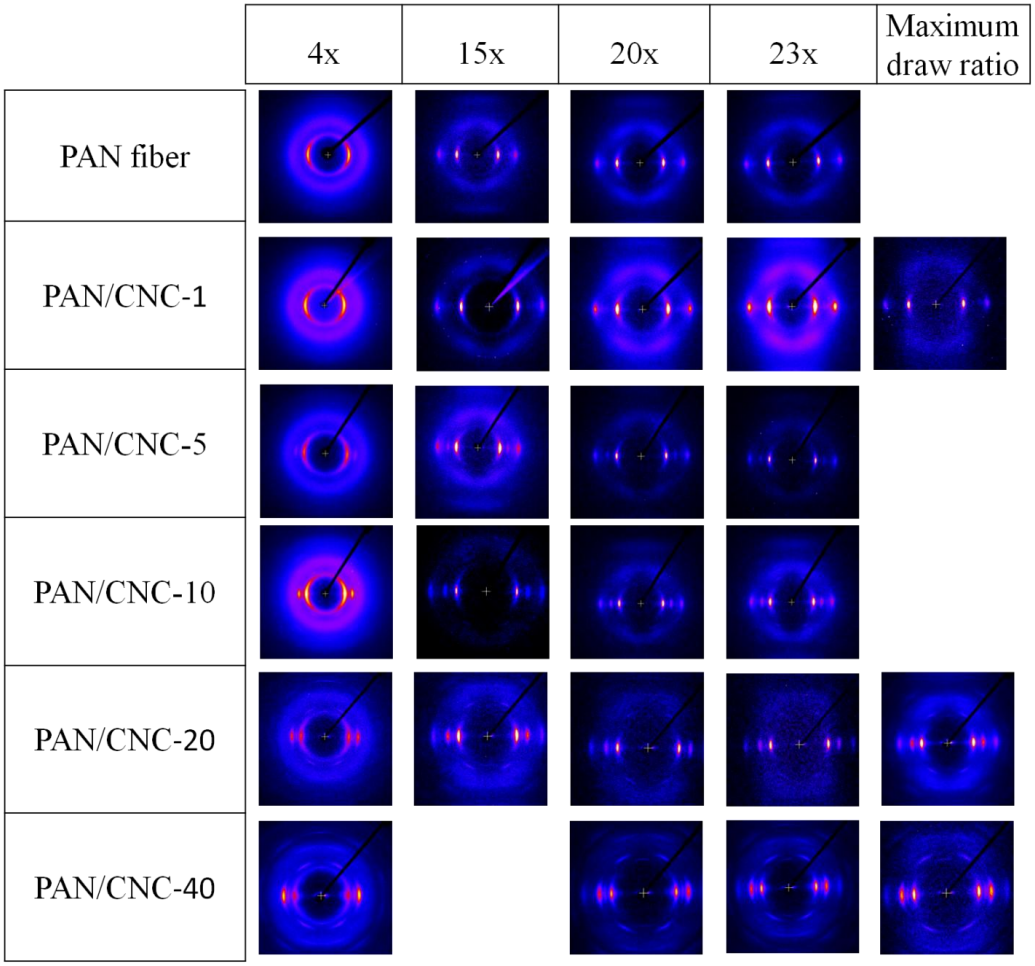

Figure A.1. WAXD patterns of PAN and PAN/CNC fibers with various draw ratios

Table A.1. Structural parameters of PAN fibers at various draw ratios.

draw ratio	4x	15x	20x	23x
a ($d_{2\theta\sim17°, Å}$)	5.28	5.22	5.23	5.24
b ($d_{2\theta\sim30°, Å}$)	3.08	3.03	3.03	3.03
a/b ratio	1.716	1.727	1.729	1.730
PAN crystallinity (%)	45	54	60	62
PAN crystallite size (nm)	3.7	9.2	9.0	8.9
f_{PAN}#	0.57	0.82	0.83	0.87
meridional peak position (2θ, degree)	39.8	39.1	39.1	39.0

f=Herman's orientation factor

Table A.2. Structural parameters of PAN/CNC-1 fibers at various draw ratios.

draw ratio	4x	15x	20x	23x	26x
a ($d_{2\theta\sim17°, Å}$)	5.27	5.23	5.26	5.27	5.10
b ($d_{2\theta\sim30°, Å}$)	3.14	3.04	3.03	3.04	2.97
a/b ratio	1.683	1.719	1.733	1.734	1.715
PAN crystallinity (%)	49	54	59	60	62
PAN crystallite size (nm)	3.5	9.6	9.5	9.5	9.5
f_{PAN}#	0.57	0.85	0.88	0.90	0.91
f_{CNC}#	※	※	※	※	※
meridional peak position (2θ, degree)	39.5	39.3	39.3	39.0	39.0

※ CNC peak is weak; # f=Herman's orientation factor

Table A.3. Structural parameters of PAN/CNC-5 fibers at various draw ratios.

draw ratio	4x	15x	20x	23x
a ($d_{2\theta\sim17°, Å}$)	5.29	5.24	5.23	5.24
b ($d_{2\theta\sim30°, Å}$)	3.17	3.03	3.03	3.03
a/b ratio	1.669	1.730	1.730	1.726
PAN crystallinity (%)	50	53	59	60
PAN crystallite size (nm)	3.4	8.8	9.2	10.1
f_{PAN} #	0.59	0.81	0.86	0.87
f_{CNC} #	0.88	0.91	0.91	0.91
Meridional peak position (2θ, degree)	39.7	39.0	38.9	38.9

f=Herman's orientation factor

Table A.4. Structural parameters of PAN/CNC-10 fibers at various draw ratios.

draw ratio	4x	15x	20x	23x
a ($d_{2\theta\sim17°, Å}$)	5.35	5.22	5.23	5.23
b ($d_{2\theta\sim30°, Å}$)	3.17	3.02	3.02	3.02
a/b ratio	1.684	1.730	1.730	1.730
PAN crystallinity (%)	48	52	70	70
PAN crystallite size (nm)	3.3	11.2	9.6	9.9
f_{PAN} #	0.57	0.83	0.85	0.89
f_{CNC} #	0.91	0.91	0.92	0.94
meridional peak position (2θ, degree)	※	38.3	38.3	※

※ PAN peak is overlapped with CNC peak

Table A.5. Structural parameters of PAN/CNC-20 fibers at various draw ratios.

draw ratio	4x	15x	20x	23x	29x
a ($d_{2\theta\sim17°, Å}$)	5.20	5.09	5.10	5.10	5.11
b ($d_{2\theta\sim30°, Å}$)	3.14	2.99	2.99	2.99	3.00
a/b ratio	1.650	1.705	1.703	1.706	1.704
PAN crystallinity (%)	52	54	54	56	63
PAN crystallite size (nm)	2.4	8.7	8.9	8.9	8.9
f_{PAN} #	0.60	0.77	0.80	0.80	0.85
f_{CNC} #	0.87	0.89	0.90	0.90	0.92
meridional peak position (2θ, degree)	※	※	※	※	※

※ PAN peak is overlapped with CNC peak

Table A.6. Structural parameters of PAN/CNC-40 fibers at various draw ratios.

draw ratio	4x	20x	23x	29x
a ($d_{2\theta\sim17°, Å}$)	5.17	5.12	5.10	5.13
b ($d_{2\theta\sim30°, Å}$)	#	3.01	2.99	3.00
a/b ratio	#	1.703	1.706	1.709
PAN crystallinity (%)	#	#	#	#
PAN crystallite size (nm)	4.3	7.1	7.1	7.1
f_{PAN} #	0.68	0.86	0.86	0.86
f_{CNC} #	0.91	0.92	0.91	0.91
Meridional peak position (2θ, degree)	※	※	※	※

Data is not available; ※ PAN peak is overlapped with CNC peak.

Table A.7. Tensile strength (MPa) of PAN and PAN/CNC fibers at various draw ratios.

draw ratio	4x	15 x	20 x	23x	Maximum Draw ratio[#]
PAN fiber	292 ± 16	748 ± 40	766 ± 49	765 ± 38	765 ± 38 (23x)
PAN/CNC-1	280 ± 20	568 ± 43	701 ± 59	710 ± 79	859 ± 97 (26x)
PAN/CNC-5	250 ± 18	619 ± 84	683 ± 96	758 ± 66	758 ± 66 (23x)
PAN/CNC-10	189 ± 15	628 ± 90	755 ± 58	868 ± 85	868 ± 85 (23x)
PAN/CNC-20	196 ± 11	620 ± 43	750 ± 26	803 ± 39	893 ± 80 (29x)
PAN/CNC-40	171 ± 15	※	636 ± 51	705 ± 54	813 ± 61 (29x)

Maximum draw ratio is listed in the bracket ; ※ data is not available

Table A.8. Tensile modulus (GPa) of PAN and PAN/CNC fibers at various draw ratios.

draw ratio	4x	15x	20x	23x	Maximum Draw ratio[#]
PAN fiber	8.7 ± 0.4	17.4 ± 0.6	18.0 ± 1.0	17.8 ± 0.8	17.8 ± 0.8 (23x)
PAN/CNC-1	9.0 ± 0.4	14.8 ± 0.5	16.3 ± 0.5	16.5 ± 0.9	19.2 ± 0.8 (26x)
PAN/CNC-5	9.8 ± 0.6	15.8 ± 1.9	17.9 ± 1.3	18.8 ± 1.4	18.8 ± 1.4 (23x)
PAN/CNC-10	10.6 ± 0.5	17.9 ± 1.5	19.5 ± 0.8	19.9 ± 1.0	19.9 ± 1.0 (23x)
PAN/CNC-20	12.5 ± 0.6	17.1 ± 0.9	20.6 ± 0.4	20.8 ± 0.8	22.1 ± 0.9 (29x)
PAN/CNC-40	18.8 ± 0.7	※	20.8 ± 0.7	17.7 ± 1.0	20.6 ± 0.9 (29x)

Maximum draw ratio is listed in the bracket ; ※ data is not available

Table A.9. Elongation at break (% strain) of PAN and PAN/CNC fibers at various draw ratios.

draw ratio	4x	15x	20x	23x	Maximum Draw ratio[#]
PAN fiber	18.9 ± 2.5	7.6 ± 0.3	7.2 ± 0.3	7.1 ± 0.5	7.1 ± 0.5 (23x)
PAN/CNC-1	40.1 ± 8.4	9.6 ± 0.7	8.0 ± 0.4	6.9 ± 0.7	7.0 ± 0.7 (26x)
PAN/CNC-5	30.4 ± 5.4	7.8 ± 0.7	7.5 ± 0.7	7.3 ± 0.9	7.3 ± 0.9 (23x)
PAN/CNC-10	38.0 ± 15.4	10.0 ± 1.6	9.1 ± 1.0	8.4 ± 0.9	8.4 ± 0.9 (23x)
PAN/CNC-20	45.1 ± 7.8	10.2 ± 0.7	7.5 ± 0.3	7.2 ± 0.4	6.6 ± 0.4 (29x)
PAN/CNC-40	1.5 ± 0.4	※	7.5 ± 1.5	8.2 ± 0.7	8.0 ± 1.2 (29x)

Maximum draw ratio is listed in the bracket ; ※ data is not available

Table A.10. Work of rupture (MPa) of PAN and PAN/CNC fibers at various draw ratios.

draw ratio	4x	15x	20x	23x	Maximum Draw ratio[#]
PAN fiber	43.6 ± 7.3	30.4 ± 2.4	29.0 ± 2.4	29.2 ± 2.0	29.2 ± 2.0 (23x)
PAN/CNC-1	93.2 ± 22.0	33.3 ± 3.3	31.6 ± 3.2	26.8 ± 4.7	34.4 ± 6.0 (26x)
PAN/CNC-5	60.6 ± 12.0	26.7 ± 3.2	26.3 ± 5.4	28.7 ± 4.6	28.7 ± 4.6 (23x)
PAN/CNC-10	46.8 ± 34.1	36.7 ± 7.4	36.8 ± 4.5	37.7 ± 5.2	37.7 ± 5.2 (23x)
PAN/CNC-20	48.8 ± 15.1	33.6 ± 3.8	29.3 ± 1.9	30.3 ± 2.9	28.2 ± 3.9 (29x)
PAN/CNC-40	1.4 ± 0.6	※	25.4 ± 5.8	28.4 ± 4.7	31.2 ± 5.8 (29x)

Maximum draw ratio is listed in the bracket ; ※ data is not available

APPENDIX B. MORPHOLOGY OF STABILIZED PAN AND PAN/CNC FIBERS AT A DRAW RATIO OF 10

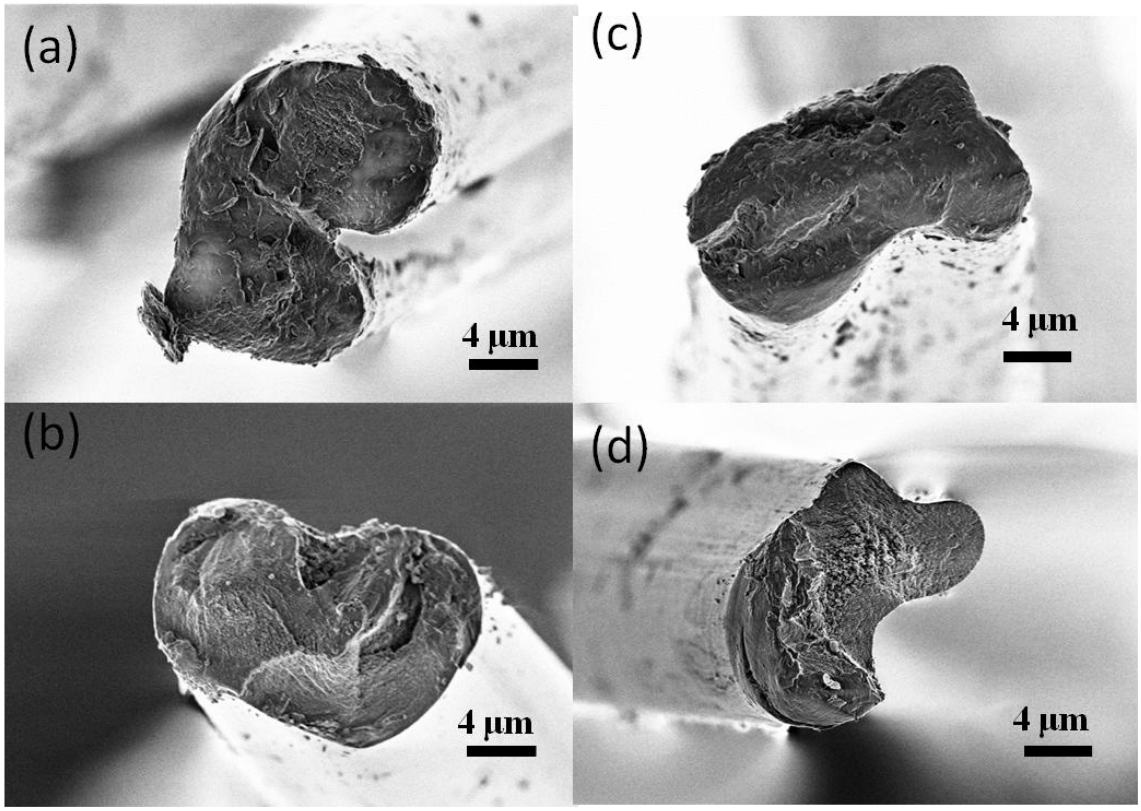

Figure B.1. SEM images of fibers with 10x draw ratio stabilized in air at 265°C under a tension of 20 MPa for various times. (a and b) PAN fibers stabilized in air for 2 and 4h, and (c and d) PAN/CNC-40 fibers stabilized in air for 2 and 4h.

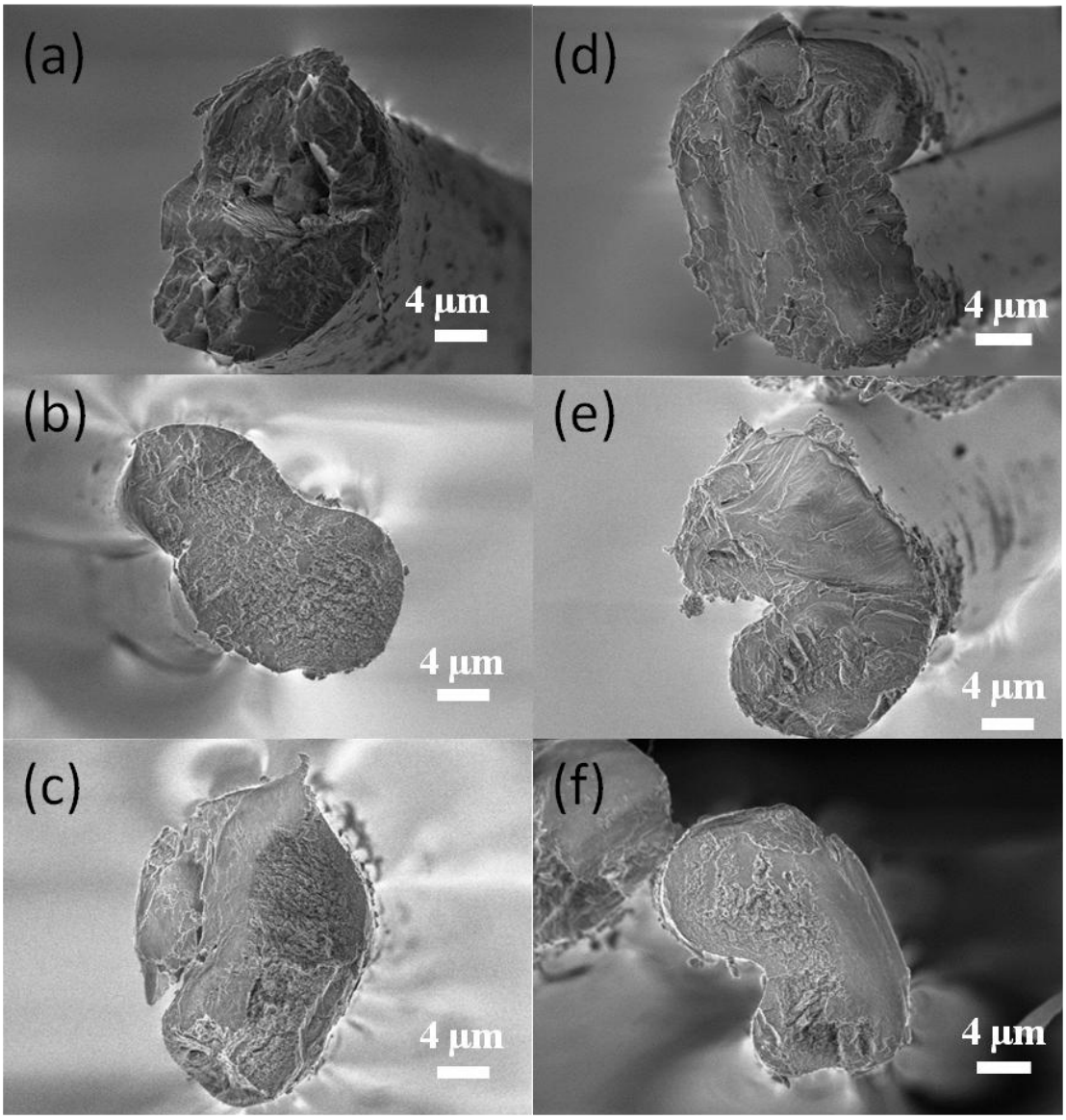

Figure B.2. SEM images of fibers with 10x draw ratio stabilized at 265°C under a tension of 20 MPa in N_2 (6h) then in air for various times. (a) PAN fibers stabilized in N_2 for 6h, (b-c) PAN fibers stabilized in N_2 for 6h then in air for 1 and 2 h, (d) PAN/CNC-40 fibers stabilized in N_2 for 6h, and (e - f) PAN/CNC-40 fibers stabilized in N_2 for 6h then in air for 1 and 2 h.

APPENDIX C. SUPPORTING INFORMATION FOR CHAPTER 7

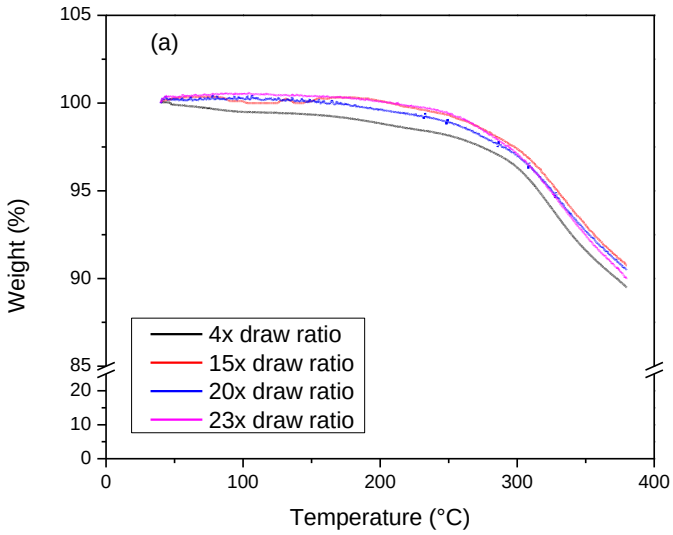

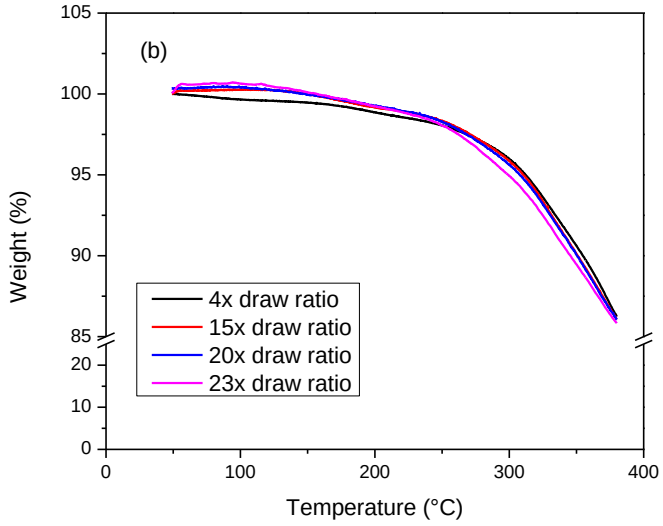

Figure C.1. TGA curves of fibers in air at a heating rate of 5 °C/min. (a) PAN fiber at various draw ratios and (b) PAN/CNC-10 fiber at various draw ratios

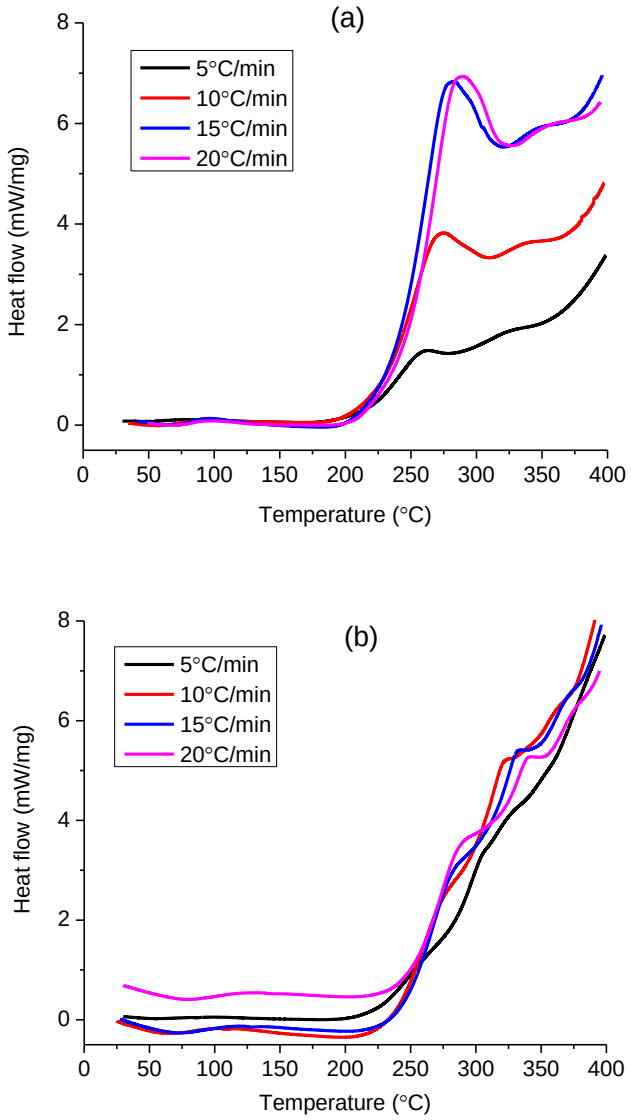

Figure C.2. DSC curves of (a) PAN and (b) PAN/CNC-40 fibers at a draw ratio of 23 with various heating rate in air.

REFERENCES

[1] V. Gupta, V. Kothari, Manufactured fibre technology, Springer Science & Business Media1997.

[2] E. Fitzer, D. Müller, The influence of oxygen on the chemical reactions during stabilization of pan as carbon fiber precursor, Carbon 13(1) (1975) 63-69.

[3] S. Nataraj, K. Yang, T. Aminabhavi, Polyacrylonitrile-based nanofibers—a state-of-the-art review, Progress in polymer science 37(3) (2012) 487-513.

[4] S.-H. Lee, S.-M. Park, Y. Kim, Effect of the concentration of sodium acetate (SA) on crosslinking of chitosan fiber by epichlorohydrin (ECH) in a wet spinning system, Carbohydrate polymers 70(1) (2007) 53-60.

[5] P. Smith, P.J. Lemstra, B. Kalb, A.J. Pennings, Ultrahigh-strength polyethylene filaments by solution spinning and hot drawing, Polymer Bulletin 1(11) (1979) 733-736.

[6] B. Qian, W. Lin, J. He, P. Hu, C. Wu, The role of macromolecular entanglements in the gel spinning process and properties of high performance polyacrylonitrile fibers, Journal of polymer engineering 15(3-4) (1995) 327-345.

[7] Y. Liu, H.G. Chae, S. Kumar, Gel-spun carbon nanotubes/polyacrylonitrile composite fibers. Part I: Effect of carbon nanotubes on stabilization, Carbon 49(13) (2011) 4466-4476.

[8] Y. Liu, H.G. Chae, S. Kumar, Gel-spun carbon nanotubes/polyacrylonitrile composite fibers. Part II: Stabilization reaction kinetics and effect of gas environment, Carbon 49(13) (2011) 4477-4486.

[9] H.G. Chae, M.L. Minus, S. Kumar, Oriented and exfoliated single wall carbon nanotubes in polyacrylonitrile, Polymer 47(10) (2006) 3494-3504.

[10] l.P. Barham, A. Keller, High-strength polyethylene fibres from solution and gel spinning, Journal of Materials Science 20(7) (1985) 2281-2302.

[11] J. Masson, Acrylic fiber technology and applications, CRC Press1995.

[12] S.R. Hutchinson, A.E. Tonelli, B.S. Gupta, D.R. Buchanan, An investigation of the structure–property relationships in melt-processable high-acrylonitrile copolymer filaments, Journal of Materials Science 43(15) (2008) 5143-5156.

[13] T. Wang, S. Kumar, Electrospinning of polyacrylonitrile nanofibers, Journal of Applied Polymer Science 102(2) (2006) 1023-1029.

[14] H. Chang, J. Luo, P.V. Gulgunje, S. Kumar, Structural and Functional Fibers, Annual Review of Materials Research 47 (2017) 331-359.

[15] M.S.A. Rahaman, A.F. Ismail, A. Mustafa, A review of heat treatment on polyacrylonitrile fiber, Polymer Degradation and Stability 92(8) (2007) 1421-1432.

[16] P. Lindenmeyer, R. Hosemann, Application of the theory of paracrystals to the crystal structure analysis of polyacrylonitrile, Journal of Applied Physics 34(1) (1963) 42-45.

[17] O.J. Sanchez, C.A. Cardona, Trends in biotechnological production of fuel ethanol from different feedstocks, Bioresource Technology 99(13) (2008) 5270-5295.

[18] M.A.S. Azizi Samir, F. Alloin, A. Dufresne, Review of Recent Research into Cellulosic Whiskers, Their Properties and Their Application in Nanocomposite Field, Biomacromolecules 6(2) (2005) 612-626.

[19] F.L. Dri, L.G. Hector Jr, R.J. Moon, P.D. Zavattieri, Anisotropy of the Elastic Properties of Crystalline Cellulose Iβ from First Principles Density Functional Theory with Van der Waals Interactions, Cellulose 20(6) (2013) 2703-2718.

[20] I. Diddens, B. Murphy, M. Krisch, M. Müller, Anisotropic Elastic Properties of Cellulose Measured Using Inelastic X-ray Scattering, Macromolecules 41(24) (2008) 9755-9759.

[21] Y. Habibi, L.A. Lucia, O.J. Rojas, Cellulose nanocrystals: chemistry, self-assembly, and applications, Chemical Reviews 110(6) (2010) 3479-3500.

[22] M.T. Postek, A. Vladár, J. Dagata, N. Farkas, B. Ming, R. Wagner, A. Raman, R.J. Moon, R. Sabo, T.H. Wegner, Development of the Metrology and Imaging of Cellulose Nanocrystals, Measurement Science and Technology 22(2) (2011) 024005.

[23] R.H. Atalla, D.L. Vanderhart, Native cellulose: a composite of two distinct crystalline forms, Science 223(4633) (1984) 283-285.

[24] P.C. Faria-Tischer, C.A. Tischer, L. Heux, S. Le Denmat, C. Picart, M.-R. Sierakowski, J.-L. Putaux, Preparation of cellulose II and III I films by allomorphic conversion of bacterial cellulose I pellicles, Materials Science and Engineering: C 51 (2015) 167-173.

[25] S. Park, J.O. Baker, M.E. Himmel, P.A. Parilla, D.K. Johnson, Research Cellulose crystallinity index: measurement techniques and their impact on interpreting cellulase performance, Biotechnology for Biofuels 3(10) (2010).

[26] R.J. Moon, A. Martini, J. Nairn, J. Simonsen, J. Youngblood, Cellulose Nanomaterials Review: Structure, Properties and Nanocomposites, Chemical Society Reviews 40(7) (2011) 3941-3994.

[27] A. Chakraborty, M. Sain, M. Kortschot, Reinforcing potential of wood pulp-derived microfibres in a PVA matrix, Holzforschung 60(1) (2006) 53-58.

[28] A. Chakraborty, M. Sain, M. Kortschot, Cellulose microfibrils: a novel method of preparation using high shear refining and cryocrushing, Holzforschung 59(1) (2005) 102-107.

[29] K. Abe, S. Iwamoto, H. Yano, Obtaining cellulose nanofibers with a uniform width of 15 nm from wood, Biomacromolecules 8(10) (2007) 3276-3278.

[30] K. Abe, F. Nakatsubo, H. Yano, High-strength nanocomposite based on fibrillated chemi-thermomechanical pulp, Composites Science and Technology 69(14) (2009) 2434-2437.

[31] A.N. Nakagaito, H. Yano, The effect of fiber content on the mechanical and thermal expansion properties of biocomposites based on microfibrillated cellulose, Cellulose 15(4) (2008) 555-559.

[32] J. Araki, M. Wada, S. Kuga, T. Okano, Birefringent glassy phase of a cellulose microcrystal suspension, Langmuir 16(6) (2000) 2413-2415.

[33] S. Elazzouzi-Hafraoui, Y. Nishiyama, J.-L. Putaux, L. Heux, F. Dubreuil, C. Rochas, The shape and size distribution of crystalline nanoparticles prepared by acid hydrolysis of native cellulose, Biomacromolecules 9(1) (2007) 57-65.

[34] Y. Chen, C. Liu, P.R. Chang, X. Cao, D.P. Anderson, Bionanocomposites based on pea starch and cellulose nanowhiskers hydrolyzed from pea hull fibre: effect of hydrolysis time, Carbohydrate Polymers 76(4) (2009) 607-615.

[35] N. Hayashi, T. Kondo, M. Ishihara, Enzymatically produced nano-ordered short elements containing cellulose Iβ crystalline domains, Carbohydrate polymers 61(2) (2005) 191-197.

[36] M. Henriksson, G. Henriksson, L. Berglund, T. Lindström, An environmentally friendly method for enzyme-assisted preparation of microfibrillated cellulose (MFC) nanofibers, European Polymer Journal 43(8) (2007) 3434-3441.

[37] S. Iwamoto, W. Kai, T. Isogai, T. Saito, A. Isogai, T. Iwata, Comparison study of TEMPO-analogous compounds on oxidation efficiency of wood cellulose for preparation of cellulose nanofibrils, Polymer Degradation and Stability 95(8) (2010) 1394-1398.

[38] Q. Cheng, S. Wang, Q. Han, Novel process for isolating fibrils from cellulose fibers by high‐intensity ultrasonication. II. Fibril characterization, Journal of applied polymer science 115(5) (2010) 2756-2762.

[39] G. Siqueira, J. Bras, A. Dufresne, Cellulosic bionanocomposites: a review of preparation, properties and applications, Polymers 2(4) (2010) 728-765.

[40] T. Abitbol, E. Kloser, D.G. Gray, Estimation of the surface sulfur content of cellulose nanocrystals prepared by sulfuric acid hydrolysis, Cellulose 20(2) (2013) 785-794.

[41] X. Cao, H. Dong, C.M. Li, New nanocomposite materials reinforced with flax cellulose nanocrystals in waterborne polyurethane, Biomacromolecules 8(3) (2007) 899-904.

[42] H. Yu, Z. Qin, B. Liang, N. Liu, Z. Zhou, L. Chen, Facile extraction of thermally stable cellulose nanocrystals with a high yield of 93% through hydrochloric acid hydrolysis under hydrothermal conditions, Journal of Materials Chemistry A 1(12) (2013) 3938-3944.

[43] S. Camarero Espinosa, T. Kuhnt, E.J. Foster, C. Weder, Isolation of thermally stable cellulose nanocrystals by phosphoric acid hydrolysis, Biomacromolecules 14(4) (2013) 1223-1230.

[44] M.M. Ruiz, J.Y. Cavaille, A. Dufresne, C. Graillat, J.F. Gérard, New waterborne epoxy coatings based on cellulose nanofillers, Macromolecular Symposia, Wiley Online Library, 2001, pp. 211-222.

[45] D. Viet, S. Beck-Candanedo, D.G. Gray, Dispersion of Cellulose Nanocrystals in Polar Organic Solvents, Cellulose 14(2) (2007) 109-113.

[46] L. Heux, G. Chauve, C. Bonini, Nonflocculating and Chiral-Nematic Self-Ordering of Cellulose Microcrystals Suspensions in Nonpolar Solvents, Langmuir 16(21) (2000) 8210-8212.

[47] S.X. Peng, H. Chang, S. Kumar, R.J. Moon, J.P. Youngblood, A comparative guide to controlled hydrophobization of cellulose nanocrystals via surface esterification, Cellulose 23(3) (2016) 1825-1846.

[48] C. Goussé, H. Chanzy, G. Excoffier, L. Soubeyrand, E. Fleury, Stable Suspensions of Partially Silylated Cellulose Whiskers Dispersed in Organic Solvents, Polymer 43(9) (2002) 2645-2651.

[49] J. Araki, M. Wada, S. Kuga, Steric Stabilization of A Cellulose Microcrystal Suspension by Poly (Ethylene Glycol) Grafting, Langmuir 17(1) (2001) 21-27.

[50] N. Ljungberg, C. Bonini, F. Bortolussi, C. Boisson, L. Heux, J.-Y. Cavaillé, New Nanocomposite Materials Reinforced with Cellulose Whiskers in Atactic Polypropylene: Effect of Surface and Dispersion Characteristics, Biomacromolecules 6(5) (2005) 2732-2739.

[51] H. Yuan, Y. Nishiyama, M. Wada, S. Kuga, Surface Acylation of Cellulose Whiskers by Drying Aqueous Emulsion, Biomacromolecules 7(3) (2006) 696-700.

[52] M. Grunert, W.T. Winter, Nanocomposites of Cellulose Acetate Butyrate Reinforced with Cellulose Nanocrystals, Journal of Polymers and the Environment 10(1) (2002) 27-30.

[53] M.A.S.A. Samir, F. Alloin, J.-Y. Sanchez, A. Dufresne, Cellulose nanocrystals reinforced poly (oxyethylene), Polymer 45(12) (2004) 4149-4157.

[54] G. Wu, D. Liu, G. Liu, J. Chen, S. Huo, Z. Kong, Thermoset nanocomposites from waterborne bio-based epoxy resin and cellulose nanowhiskers, Carbohydrate Polymers 127 (2015) 229-235.

[55] G. Gong, A.P. Mathew, K. Oksman, Toughening effect of cellulose nanowhiskers on polyvinyl acetate: fracture toughness and viscoelastic analysis, Polymer Composites 32(10) (2011) 1492-1498.

[56] J. Luo, H. Chang, A.A.B. Davijani, H.C. Liu, P.-H. Wang, R.J. Moon, S. Kumar, Influence of high loading of cellulose nanocrystals in polyacrylonitrile composite films, Cellulose (2017) 1-14.

[57] P. Lu, Y.-L. Hsieh, Cellulose nanocrystal-filled poly (acrylic acid) nanocomposite fibrous membranes, Nanotechnology 20(41) (2009) 415604.

[58] I. Cacciotti, E. Fortunati, D. Puglia, J.M. Kenny, F. Nanni, Effect of silver nanoparticles and cellulose nanocrystals on electrospun poly (lactic) acid mats: Morphology, thermal properties and mechanical behavior, Carbohydrate Polymers 103 (2014) 22-31.

[59] C. Xiang, A.G. Taylor, J.P. Hinestroza, M.W. Frey, Controlled release of nonionic compounds from poly (lactic acid)/cellulose nanocrystal nanocomposite fibers, Journal of Applied Polymer Science 127(1) (2013) 79-86.

[60] J.O. Zoppe, M.S. Peresin, Y. Habibi, R.A. Venditti, O.J. Rojas, Reinforcing poly (ε-caprolactone) nanofibers with cellulose nanocrystals, ACS Applied Materials & Interfaces 1(9) (2009) 1996-2004.

[61] C. Zhou, R. Chu, R. Wu, Q. Wu, Electrospun polyethylene oxide/cellulose nanocrystal composite nanofibrous mats with homogeneous and heterogeneous microstructures, Biomacromolecules 12(7) (2011) 2617-2625.

[62] M.S. Peresin, Y. Habibi, A.-H. Vesterinen, O.J. Rojas, J.J. Pawlak, J.V. Seppälä, Effect of moisture on electrospun nanofiber composites of poly (vinyl alcohol) and cellulose nanocrystals, Biomacromolecules 11(9) (2010) 2471-2477.

[63] H. Dong, K.E. Strawhecker, J.F. Snyder, J.A. Orlicki, R.S. Reiner, A.W. Rudie, Cellulose nanocrystals as a reinforcing material for electrospun poly (methyl methacrylate) fibers: Formation, properties and nanomechanical characterization, Carbohydrate Polymers 87(4) (2012) 2488-2495.

[64] E.E. Urena-Benavides, P.J. Brown, C.L. Kitchens, Effect of jet stretch and particle load on cellulose nanocrystal− alginate nanocomposite fibers, Langmuir 26(17) (2010) 14263-14270.

[65] S. Chen, G. Schueneman, R.B. Pipes, J. Youngblood, R.J. Moon, Effects of Crystal Orientation on Cellulose Nanocrystals–Cellulose Acetate Nanocomposite Fibers Prepared by Dry Spinning, Biomacromolecules 15(10) (2014) 3827-3835.

[66] L. Liu, X. Yang, H. Yu, C. Ma, J. Yao, Biomimicking the structure of silk fibers via cellulose nanocrystal as β-sheet crystallite, RSC Advances 4(27) (2014) 14304-14313.

[67] S. Eichhorn, J. Sirichaisit, R. Young, Deformation mechanisms in cellulose fibres, paper and wood, Journal of Materials Science 36(13) (2001) 3129-3135.

[68] W. Hamad, S. Eichhorn, Deformation micromechanics of regenerated cellulose fibers using Raman spectroscopy, Journal of Engineering Materials and Technology 119(3) (1997) 309-313.

[69] R. Rusli, K. Shanmuganathan, S.J. Rowan, C. Weder, S.J. Eichhorn, Stress-transfer in anisotropic and environmentally adaptive cellulose whisker nanocomposites, Biomacromolecules 11(3) (2010) 762-768.

[70] S. Tanpichai, F. Quero, M. Nogi, H. Yano, R.J. Young, T. Lindström, W.W. Sampson, S.J. Eichhorn, Effective Young's modulus of bacterial and microfibrillated cellulose fibrils in fibrous networks, Biomacromolecules 13(5) (2012) 1340-1349.

[71] A. Šturcová, G.R. Davies, S.J. Eichhorn, Elastic modulus and stress-transfer properties of tunicate cellulose whiskers, Biomacromolecules 6(2) (2005) 1055-1061.

[72] S. Chand, Review carbon fibers for composites, Journal of Materials Science 35(6) (2000) 1303-1313.

[73] H.G. Chae, B.A. Newcomb, P.V. Gulgunje, Y. Liu, K.K. Gupta, M.G. Kamath, K.M. Lyons, S. Ghoshal, C. Pramanik, L. Giannuzzi, High strength and high modulus carbon fibers, Carbon 93 (2015) 81-87.

[74] T.H. Ko, Influence of continuous stabilization on the physical properties and microstructure of PAN-based carbon fibers, Journal of Applied Polymer Science 42(7) (1991) 1949-1957.

[75] S. Dalton, F. Heatley, P.M. Budd, Thermal stabilization of polyacrylonitrile fibres, Polymer 40(20) (1999) 5531-5543.

[76] T.H. Ko, T.C. Day, M.F. Lin, The effect of precarbonization on mechanical properties of final polyacrylonitrile-based carbon fibres, Journal of materials science letters 12(5) (1993) 343-345.

[77] D. Qian, E.C. Dickey, R. Andrews, T. Rantell, Load transfer and deformation mechanisms in carbon nanotube-polystyrene composites, Applied Physics Letters 76(20) (2000) 2868-2870.

[78] M. Minus, S. Kumar, The processing, properties, and structure of carbon fibers, JOM 57(2) (2005) 52-58.

[79] S. Kumar, D.P. Anderson, A.S. Crasto, Carbon fibre compressive strength and its dependence on structure and morphology, Journal of Materials Science 28(2) (1993) 423-439.

[80] H.G. Chae, M.L. Minus, A. Rasheed, S. Kumar, Stabilization and carbonization of gel spun polyacrylonitrile/single wall carbon nanotube composite fibers, Polymer 48(13) (2007) 3781-3789.

[81] Y. Liu, H.G. Chae, S. Kumar, Gel-spun carbon nanotubes/polyacrylonitrile composite fibers. Part III: Effect of stabilization conditions on carbon fiber properties, Carbon 49(13) (2011) 4487-4496.

[82] B.A. Newcomb, L.A. Giannuzzi, K.M. Lyons, P.V. Gulgunje, K. Gupta, Y. Liu, M. Kamath, K. McDonald, J. Moon, B. Feng, High resolution transmission electron microscopy study on polyacrylonitrile/carbon nanotube based carbon fibers and the effect of structure development on the thermal and electrical conductivities, Carbon 93 (2015) 502-514.

[83] M. Tang, R. Bacon, Carbonization of cellulose fibers—I. Low temperature pyrolysis, Carbon 2(3) (1964) 211-220.

[84] E. Frank, L.M. Steudle, D. Ingildeev, J.M. Spörl, M.R. Buchmeiser, Carbon fibers: precursor systems, processing, structure, and properties, Angewandte Chemie International Edition 53(21) (2014) 5262-5298.

[85] X. Zhang, Y. Lu, H. Xiao, H. Peterlik, Effect of hot stretching graphitization on the structure and mechanical properties of rayon-based carbon fibers, Journal of Materials Science 49(2) (2014) 673-684.

[86] A.E. Lewandowska, C. Soutis, L. Savage, S.J. Eichhorn, Carbon fibres with ordered graphitic-like aggregate structures from a regenerated cellulose fibre precursor, Composites Science and Technology 116 (2015) 50-57.

[87] H. Xiao, Y. Lu, W. Zhao, X. Qin, A comparison of the effect of hot stretching on microstructures and properties of polyacrylonitrile and rayon-based carbon fibers, Journal of Materials Science 49(14) (2014) 5017-5029.

[88] K. Sudo, K. Shimizu, A new carbon fiber from lignin, Journal of Applied Polymer Science 44(1) (1992) 127-134.

[89] S. Kubo, J. Kadla, Lignin-based carbon fibers: Effect of synthetic polymer blending on fiber properties, Journal of Polymers and the Environment 13(2) (2005) 97-105.

[90] J. Kadla, S. Kubo, R. Venditti, R. Gilbert, A. Compere, W. Griffith, Lignin-based carbon fibers for composite fiber applications, Carbon 40(15) (2002) 2913-2920.

[91] S.H. Park, S.G. Lee, S.H. Kim, The use of a nanocellulose-reinforced polyacrylonitrile precursor for the production of carbon fibers, Journal of Materials Science 48(20) (2013) 6952-6959.

[92] P.J. Bissett, C.W. Herriott, Lignin/polyacrylonitrile-containing dopes, fibers, and methods of making same, US Patent 8771832, 2014.

[93] H.C. Liu, A.-T. Chien, B.A. Newcomb, Y. Liu, S. Kumar, Processing, Structure, and Properties of Lignin-and CNT-Incorporated Polyacrylonitrile-Based Carbon Fibers, ACS Sustainable Chemistry & Engineering 3(9) (2015) 1943-1954.

[94] S. Kumar, H. Chang, Polyacrylonitrile/cellulose nano-structure fibers, US Patent 9409337, 2016.

[95] X. Dong, C. Lu, P. Zhou, S. Zhang, L. Wang, D. Li, Polyacrylonitrile/lignin sulfonate blend fiber for low-cost carbon fiber, RSC Advances 5(53) (2015) 42259-42265.

[96] J. Lu, P. Askeland, L.T. Drzal, Surface Modification of Microfibrillated Cellulose for Epoxy Composite Applications, Polymer 49(5) (2008) 1285-1296.

[97] M.A.S. Azizi Samir, F. Alloin, J.-Y. Sanchez, N. El Kissi, A. Dufresne, Preparation of Cellulose Whiskers Reinforced Nanocomposites From An Organic Medium Suspension, Macromolecules 37(4) (2004) 1386-1393.

[98] R.R. Lahiji, X. Xu, R. Reifenberger, A. Raman, A. Rudie, R.J. Moon, Atomic Force Microscopy Characterization of Cellulose Nanocrystals, Langmuir 26(6) (2010) 4480-4488.

[99] J.M. Bernal-García, A. Guzmán-López, A. Cabrales-Torres, A. Estrada-Baltazar, G.A. Iglesias-Silva, Densities and Viscosities of (N, N-Dimethylformamide+ Water) at Atmospheric Pressure from (283.15 to 353.15) K, Journal of Chemical & Engineering Data 53(4) (2008) 1024-1027.

[100] C. Wohlfarth, Refractive Index of the Mixture (1) Water;(2) N, N-Dimethylformamide, Refractive indices of pure liquids and binary liquid mixtures (supplement to III/38), Springer2008, pp. 580-581.

[101] J. Riseman, J.G. Kirkwood, The Intrinsic Viscosity, Translational and Rotatory Diffusion Constants of Rodlike Macromolecules in Solution, The Journal of Chemical Physics 18(4) (1950) 512-516.

[102] S. Beck, J. Bouchard, R. Berry, Dispersibility in Water of Dried Nanocrystalline Cellulose, Biomacromolecules 13(5) (2012) 1486-1494.

[103] A.C. Khazraji, S. Robert, Interaction Effects Between Cellulose and Water in Nanocrystalline and Amorphous Regions: A Novel Approach Using Molecular Modeling, Journal of Nanomaterials 2013 (2013) 44.

[104] D.W. Fengel, G., Wood: Chemistry, Ultrastructure, Reactions, Walter de Gruyter: New York, (1989) pp 77-81.

[105] M.S. Peresin, Y. Habibi, J.O. Zoppe, J.J. Pawlak, O.J. Rojas, Nanofiber composites of polyvinyl alcohol and cellulose nanocrystals: manufacture and characterization, Biomacromolecules 11(3) (2010) 674-681.

[106] A. Jalal Uddin, J. Araki, Y. Gotoh, Toward "Strong" Green Nanocomposites: Polyvinyl Alcohol Reinforced with Extremely Oriented Cellulose Whiskers, Biomacromolecules 12(3) (2011) 617-624.

[107] W.J. Lee, A.J. Clancy, E. Kontturi, A. Bismarck, M.S. Shaffer, Strong and Stiff: High-Performance Cellulose Nanocrystal/Poly (vinyl alcohol) Composite Fibers, ACS Applied Materials & Interfaces 8(46) (2016) 31500-31504.

[108] Y. Liu, Y.H. Choi, H.G. Chae, P. Gulgunje, S. Kumar, Temperature dependent tensile behavior of gel-spun polyacrylonitrile and polyacrylonitrile/carbon nanotube composite fibers, Polymer 54(15) (2013) 4003-4009.

[109] H.G. Chae, T. Sreekumar, T. Uchida, S. Kumar, A comparison of reinforcement efficiency of various types of carbon nanotubes in polyacrylonitrile fiber, Polymer 46(24) (2005) 10925-10935.

[110] L.E. Alexander, In X-Ray Diffraction Methods in Polymer Science, Robert, E., Ed.; Krieger Publishing Co.: Huntington, NY (1979) pp 198-277.

[111] E.E. Urena-Benavides, C.L. Kitchens, Wide-Angle X-ray Diffraction of Cellulose Nanocrystal− Alginate Nanocomposite Fibers, Macromolecules 44(9) (2011) 3478-3484.

[112] N. Marcovich, M. Auad, N. Bellesi, S. Nutt, M. Aranguren, Cellulose micro/nanocrystals reinforced polyurethane, Journal of Materials Research 21(4) (2006) 870-881.

[113] D. Liu, X. Chen, Y. Yue, M. Chen, Q. Wu, Structure and rheology of nanocrystalline cellulose, Carbohydrate Polymers 84(1) (2011) 316-322.

[114] S.H. Lee, E. Cho, S.H. Jeon, J.R. Youn, Rheological and electrical properties of polypropylene composites containing functionalized multi-walled carbon nanotubes and compatibilizers, Carbon 45(14) (2007) 2810-2822.

[115] M.-K. Seo, S.-J. Park, Electrical resistivity and rheological behaviors of carbon nanotubes-filled polypropylene composites, Chemical Physics Letters 395(1) (2004) 44-48.

[116] Y.H. Choi, Polyacrylonitrile/carbon nanotube composite fibers: effect of various processing parameters on fiber structure and properties, Georgia Institute of Technology, Ph.D Thesis, 2010.

[117] K. Littunen, U. Hippi, T. Saarinen, J. Seppälä, Network formation of nanofibrillated cellulose in solution blended poly (methyl methacrylate) composites, Carbohydrate Polymers 91(1) (2013) 183-190.

[118] Z. Wangxi, L. Jie, W. Gang, Evolution of structure and properties of PAN precursors during their conversion to carbon fibers, Carbon 41(14) (2003) 2805-2812.

[119] P. Lu, Y.-L. Hsieh, Preparation and characterization of cellulose nanocrystals from rice straw, Carbohydrate Polymers 87(1) (2012) 564-573.

[120] J.O. Zoppe, Y. Habibi, O.J. Rojas, R.A. Venditti, L.-S. Johansson, K. Efimenko, M. Osterberg, J. Laine, Poly (N-isopropylacrylamide) brushes grafted from cellulose nanocrystals via surface-initiated single-electron transfer living radical polymerization, Biomacromolecules 11(10) (2010) 2683-2691.

[121] D. Sawai, A. Yamane, T. Kameda, T. Kanamoto, M. Ito, H. Yamazaki, K. Hisatani, Uniaxial drawing of isotactic poly (acrylonitrile): development of oriented structure and tensile properties, Macromolecules 32(17) (1999) 5622-5630.

[122] A.-T. Chien, B.A. Newcomb, D. Sabo, J. Robbins, Z.J. Zhang, S. Kumar, High-strength superparamagnetic composite fibers, Polymer 55(16) (2014) 4116-4124.

[123] D. Sawai, T. Kanamoto, H. Yamazaki, K. Hisatani, Dynamic mechanical relaxations in poly (acrylonitrile) with different stereoregularities, Macromolecules 37(8) (2004) 2839-2846.

[124] N. Wanasekara, R. Santos, C. Douch, E. Frollini, S.J. Eichhorn, Orientation of cellulose nanocrystals in electrospun polymer fibres, Journal of Materials Science 51(1) (2016) 218-227.

[125] R. Allen, I. Ward, Z. Bashir, An investigation into the possibility of measuring an ‘X-ray modulus’ and new evidence for hexagonal packing in polyacrylonitrile, Polymer 35(10) (1994) 2063-2071.

[126] R. Allen, I. Ward, Z. Bashir, The variation of the D-spacings with stress in the hexagonal polymorph of polyacrylonitrile, Polymer 35(19) (1994) 4035-4040.

[127] R. Ibbett, S. Gaddipati, S. Hill, G. Tucker, Structural reorganisation of cellulose fibrils in hydrothermally deconstructed lignocellulosic biomass and relationships with enzyme digestibility, Biotechnology for Biofuels 6(1) (2013) 1.

[128] G. Duesberg, I. Loa, M. Burghard, K. Syassen, S. Roth, Polarized Raman spectroscopy on isolated single-wall carbon nanotubes, Physical Review Letters 85(25) (2000) 5436.

[129] E. López-Honorato, P. Meadows, R. Shatwell, P. Xiao, Characterization of the anisotropy of pyrolytic carbon by Raman spectroscopy, Carbon 48(3) (2010) 881-890.

[130] Z. Li, R.J. Young, I.A. Kinloch, Interfacial stress transfer in graphene oxide nanocomposites, ACS Applied Materials & Interfaces 5(2) (2013) 456-463.

[131] T. Liu, S. Kumar, Quantitative characterization of SWNT orientation by polarized Raman spectroscopy, Chemical Physics Letters 378(3) (2003) 257-262.

[132] A. Jorio, A. Souza Filho, V. Brar, A. Swan, M. Ünlü, B. Goldberg, A. Righi, J. Hafner, C. Lieber, R. Saito, Polarized resonant Raman study of isolated single-wall carbon nanotubes: Symmetry selection rules, dipolar and multipolar antenna effects, Physical Review B 65(12) (2002) 121402.

[133] W.J. Jones, D.K. Thomas, D.W. Thomas, G. Williams, On the determination of order parameters for homogeneous and twisted nematic liquid crystals from Raman spectroscopy, Journal of Molecular Structure 708(1) (2004) 145-163.

[134] B.A. Newcomb, H.G. Chae, P.V. Gulgunje, K. Gupta, Y. Liu, D.E. Tsentalovich, M. Pasquali, S. Kumar, Stress transfer in polyacrylonitrile/carbon nanotube composite fibers, Polymer 55(11) (2014) 2734-2743.

[135] S. Iwamoto, W. Kai, A. Isogai, T. Iwata, Elastic modulus of single cellulose microfibrils from tunicate measured by atomic force microscopy, Biomacromolecules 10(9) (2009) 2571-2576.

[136] X. Chen, M. Zheng, C. Park, C. Ke, Direct measurements of the mechanical strength of carbon nanotube–poly (methyl methacrylate) interfaces, Small 9(19) (2013) 3345-3351.

[137] A.H. Barber, S.R. Cohen, S. Kenig, H.D. Wagner, Interfacial fracture energy measurements for multi-walled carbon nanotubes pulled from a polymer matrix, Composites Science and Technology 64(15) (2004) 2283-2289.

[138] H.C. Liu, A.-T. Chien, B.A. Newcomb, A.A.B. Davijani, S. Kumar, Stabilization kinetics of gel spun polyacrylonitrile/lignin blend fiber, Carbon 101 (2016) 382-389.

[139] I. Karacan, T. Soy, Structure and properties of oxidatively stabilized viscose rayon fibers impregnated with boric acid and phosphoric acid prior to carbonization and activation steps, Journal of Materials Science 48(5) (2013) 2009-2021.

[140] I. Shimada, T. Takahagi, M. Fukuhara, K. Morita, A. Ishitani, FT‐IR study of the stabilization reaction of polyacrylonitrile in the production of carbon fibers, Journal of Polymer Science Part A: Polymer Chemistry 24(8) (1986) 1989-1995.

[141] A. Gupta, I. Harrison, New aspects in the oxidative stabilization of PAN-based carbon fibers, Carbon 34(11) (1996) 1427-1445.

[142] H.E. Kissinger, Reaction kinetics in differential thermal analysis, Analytical chemistry 29(11) (1957) 1702-1706.

[143] C.R. Nair, K. Krishnan, K. Ninan, Differential scanning calorimetric study on the Claisen rearrangement and thermal polymerisation of diallyl ether of bisphenols, Thermochimica acta 359(1) (2000) 61-67.

[144] X. Liu, W. Chen, Y.-l. Hong, S. Yuan, S. Kuroki, T. Miyoshi, Stabilization of Atactic-Polyacrylonitrile under Nitrogen and Air As Studied by Solid-State NMR, Macromolecules 48(15) (2015) 5300-5309.

[145] G. Husman, Development and Commercialization of a Novel Low-Cost Carbon Fiber, Presentation at 2012 DOE Hydrogen and Fuel Cells Program and Vehicle Technologies Program Annual Merit Review and Peer Evaluation Meeting (2012).

[146] D.A. Baker, T.G. Rials, Recent advances in low-cost carbon fiber manufacture from lignin, Journal of Applied Polymer Science 130(2) (2013) 713-728.